THESIS

METHODOLOGY FOR CALCULATING SHEAR STRESS IN A MEANDERING CHANNEL

Submitted by

Sin, Kyung-Seop

Department of Civil and Environmental Engineering

In partial fulfillment of the requirements

For the Degree of Master of Science

Colorado State University

Fort Collins, Colorado

Fall 2010

Master's Committee:

Department Head: Luis A. Garcia

Advisor: Christopher I. Thornton

Pierre Y. Julien

Ellen E. Wohl

ABSTRACT

METHODOLOGY FOR CALCULATING SHEAR STRESS IN A MEANDERING CHANNEL

Shear stress in meandering channels is the key parameter to predict bank erosion and bend migration. A representative study reach of the Rio Grande River in central New Mexico has been modeled in the Hydraulics Laboratory at CSU. To determine the shear stress distribution in a meandering channel, the large scale (1:12) physical modeling study was conducted in the following phases: 1) model construction 2) data collection 3) data analysis, and 4) conclusion and technical recommendations. Data of flow depth, flow velocity in three velocity components (V_x, V_y and V_z) and bed shear stress using a Preston tube were collected in the laboratory.

According to the laboratory data analysis, shear stress from a Preston tube is the most appropriate shear stress calculation method. In case of the Preston tube, data collection was performed directly on the surface of the channel. Other shear stress calculation methods were based on ADV (Acoustic Doppler Velocity) data that were not collected directly on the bed surface. Therefore, the shear stress determined from ADV measurements was underestimated. Additionally, K_b (the ratio of maximum shear stress to average shear stress) plots were generated. Finally, the envelope

equation for K_b from the Preston tube measurements was selected as the most appropriate equation to design meandering channels.

Sin, Kyung-Seop
Department of Civil and Environmental Engineering
Colorado State University
Fort Collins, CO 80523
Fall, 2010

ACKNOWLEDGEMENTS

First of all, I especially wish to express my huge gratitude to Dr. Christopher Thornton who supported my graduate work and continuously provided me with many details and suggestions for this research. Also, I want to record my thanks to my committee members, Dr. Pierre Julien and Dr. Ellen Wohl for providing me with valuable observations to complete this study. I am also indebted to Amanda Cox and Michael Robinson who offered constructive criticism of my work as it progressed. In addition, I wish to show my appreciation to civil engineering graduate students at CSU who gave me useful suggestions and encouragements to improve my graduate study. Additionally, I should like to thank CSU civil engineering faculty members who established my academic background in classes to finish this graduate study successfully. This thesis would never have become what it now without patience, support and encouragement of my family members; my father (Shin, Young-ho), my mother (Kim, Young-Hee), my wife (Lee, Yong-Bin) and my younger sister (Shin, Jung-Hye). I here express my more than grateful recognition. They always have been there, providing all sorts of visible and invisible support for me. I am sending most sincere thanks to them.

Table of Contents

1 Introduction 1
1.1 Background 1
1.2 Project Background 1
1.3 Research Objectives 3
2 Literature Review 4
2.1 Introduction 4
2.2 Open Channel Flow in Meandering Bends 5
2.2.1 Meandering Channel Geometry 5
2.2.2 Flow Patterns in Meandering Channels 7
2.2.2.1 Stream Morphology 7
2.2.2.2 Transverse Velocity Distribution in Bends 11
2.2.2.3 Superelevation against the Outside of the Bank 12
2.2.3 Erosion Patterns in Meandering Rivers 13
2.2.4 Channel Stability 16
2.3 Shear Stress Calculation Methods 18
2.3.1 Preston Tube 18
2.3.1.1 Preston (1954) 18
2.3.1.2 Ippen and Drinker (1962) 23
2.3.1.3 Heintz (2002) 26
2.3.1.4 Sclafani (2008) 27
2.3.2 Linear Regression of Flow Velocity Profile 28
2.3.2.1 Clauser (1956) 28
2.3.2.2 Schlicting (1987) 30
2.3.2.3 Smart (1999) 31
2.3.3 Rozovskii's Method (1961) 33
2.3.3.1 Laboratory Study for Validation of Theory 35
2.3.3.2 Field Observation for Validation of Theory 36
2.3.4 Reynolds Shear Stress 39
2.3.4.1 Wahl (2000) 39
2.3.4.2 Baird (2004) 42
2.4 Summary 44
3 Data Analysis 45
3.1 Introduction 45
3.2 Shear Stress Calculation Results 45
3.2.1 Preston Tube 46
3.2.2 Linear Regression of Flow Velocity Profile 51
3.2.3 Rozovskii Method 54
3.2.4 Reynolds Shear Stress 59
3.3 Summary 66
4 Comparisons of Shear Stress Calculation Methods 67
4.1 Comparison of Shear Stress from Preston Tube and Linear Regression of Velocity Profile for Longitudinal Direction 68
4.2 Comparison of Shear Stress from Linear Regression of Velocity Profile for Lateral Direction (τ_y) and Rozovskii Method 72

4.3 Comparison of Shear Stress from Preston Tube and Reynolds Shear Stress Extrapolation 73
4.4 Comparison of Shear Stress from Linear Regression of Velocity Profile for Longitudinal Direction (τ_x) and Reynolds Shear Stress Extrapolation 77
4.5 Comprehensive Comparisons 81
4.6 Averaged Shear Stress from HEC-RAS and K_b Value 84
5 Conclusions and Recommendations 88
5.1 Overview 88
5.2 Conclusions 88
5.3 Recommendations for Future Research 91
5.4 Limitations of this Study 91
6 References 93
Appendix A. Model Description 96
A.1 Introduction 97
A.2 Model Description 97
A.2.1 Model Geometry 98
A.2.2 Model Construction 101
A.3 Instrumentation 106
A.3.1 Flow Rate Measurement 106
A.3.2 Flow Depth Measurement 107
A.3.3 Velocity Measurement 109
A.3.4 Shear Stress Measurement 111
A.4 Model Calibration 112
A.5 Test Program (Test Matrix) 114
Appendix B. Preston Tube Calibration 115
Appendix C. Linear Regression of Flow Velocity Profile 120
Appendix D. Shear Stress from Rozovskii (1961) Method 131
Appendix E. Reynolds Shear Stress Extrapolation 142
E.1 Reynolds Shear Extrapolation 143
Appendix F. Comparison of Shear Stress from Linear Regression of Velocity Profile for Lateral Direction (τ_y) and Rozovskii Method 153
Appendix G. Comparison of Shear Stress Maximum Values 156
G.1 Comparison of Shear Stress Maximum Values 157

List of Figures

Figure 2.1 Typical Meandering Channel (from Watson et al. (2005)) 4
Figure 2.2 Geometry of Meandering Channel (from Watson et al. (2005)) 6
Figure 2.3 Description of Sine-Generated Curve Function (from Knighton (1998)) ... 7
Figure 2.4 Schematic Description of Straight Channel and Meandering Channel (from Federal Interagency Stream Restoration Working Group (FISHRWG) (1998)).8
Figure 2.5 A typical meandering stream with point bars (from Watson et al. (2005)). 8
Figure 2.6 Typical Middle Bar (from Watson et al. (2005)) 9
Figure 2.7 Typical Alternate Bars (from Watson et al. (2005)).................................. 10
Figure 2.8 Typical Braid Bars (from Watson et al. (2005))....................................... 10
Figure 2.9 Schematic Descriptions of Flow in Meandering Channel (from FHWA (2001))... 11
Figure 2.10 Sketch of the flow around bend (from FHWA (2001)).......................... 12
Figure 2.11 Geomorphic Change of Straight Channel into Meandering Channel (from Knighton, (1998)) 14
Figure 2.12 The relationship of relative migration rate to bend curvature for 18 rivers (from Knighton (1998)) 15
Figure 2.13 Seven Modes of Meander Loop Development (from FHWA (2001)).... 15
Figure 2.14 Lane's Balance (from Rosgen (1996)) 16
Figure 2.15 Sketch of Data Collection Facility of Preston (from Preston (1954))..... 20
Figure 2.16 Actual Observations of round pitot on wall of circular pipe (from Preston (1954))... 21
Figure 2.17 The Plot of Non-Dimensional Results of Experimentations of Preston (1954)... 22
Figure 2.18 Sketches of Laboratory Flume (from Ippen and Drinker (1962)).......... 23
Figure 2.19 Preston Tube for Shear Stress Measurement (at left) and Pressure Transducer (at right) (from Heintz 2002) 26
Figure 2.21 Relationship between Log Profile Parameters and Shear Velocity Head (from Smart 1999)) 31
Figure 2.22 Velocity Distribution from the Test result by the Experiment of Polygonal Section (from Rozovskii, 1961)... 35
Figure 2.23 Description of Study Reach, Desna River (from Rozovskii, 1961)........ 36
Figure 2.24 Plan View of Snov River (from Rozovskii, 1961) 37
Figure 2.25 Distribution of Flow Velocity of Snov River (from Rozovskii, 1961) ... 38
Figure 2.26 Schematic Sketch of Surface Stresses (from Julien 1998)..................... 39
Figure 2.27 The Description of Turbulence in Flow (from Julien 1998) 40
Figure 2.28 Reynolds Shear stress Profile (from Baird (2004)) 43
Figure 3.1 Shear Stress Distribution, τ_x, from Preston Tube for 8 cfs (psf) 47
Figure 3.2 Shear Stress Distribution, τ_x, from Preston Tube for 12 cfs (psf) 48
Figure 3.3 Shear Stress Distribution, τ_x, from Preston Tube for 16 cfs (psf) 49
Figure 3.4 Shear Stress Distribution, τ_x, from Preston Tube for 20 cfs (psf) 50
Figure 3.5 Shear Stress Distribution, τ_x, by Linear Regression for 20 cfs (psf)......... 52
Figure 3.6 Shear Stress Distribution, τ_y, by Linear Regression for 20 cfs (psf)......... 53
Figure 3.7 Schematic Sketch of Distance between Piezo a and Piezo g.................... 55

Figure 3.9 Radial Shear Stress Distribution, τ_r, from Rozovskii (1961) for 20 cfs ... 57
Figure 3.10 Water Surface Slope Distribution for 20 cfs 58
Figure 3.11 Profile of Reynolds Shear Stress of τ_{xz} for 20 cfs Cross Section 8 Piezo e 60
Figure 3.12 Profile of Reynolds Shear Stress of τ_{zy} for 20 cfs Cross Section 8 Piezo e 60
Figure 3.13 Contour Map of τ_{bed} from Reynolds Shear Stress for 8 cfs (psf) 62
Figure 3.14 Contour Map of τ_{bed} from Reynolds Shear Stress for 12 cfs (psf) 63
Figure 3.15 Contour Map of τ_{bed} from Reynolds Shear Stress for 16 cfs (psf) 64
Figure 3.16 Contour Map of τ_{bed} from Reynolds Shear Stress for 20 cfs (psf) 65
Figure 4.1 Chart of Shear Stress Calculation Methods Comparison 67
Figure 4.2 Comparison of Shear Stress from Preston Tube and Linear Regression of Flow Velocity Profile for 8 cfs 69
Figure 4.3 Comparison of Shear Stress from Preston Tube and Linear Regression of Flow Velocity Profile for 12 cfs 69
Figure 4.4 Comparison of Shear Stress from Preston Tube and Linear Regression of Flow Velocity Profile for 16 cfs 70
Figure 4.5 Comparison of Shear Stress from Preston Tube and Linear Regression of Flow Velocity Profile for 20 cfs 70
Figure 4.6 Averaged Percentage Difference between Preston Tube and Linear Regression with Change of Discharge 71
Figure 4.7 Comparison of Shear Stress from Preston Tube and Reynolds Shear Stress Extrapolation for 8 cfs 74
Figure 4.8 Comparison of Shear Stress from Preston Tube and Reynolds Shear Stress Extrapolation for 12 cfs 74
Figure 4.9 Comparison of Shear Stress from Preston Tube and Reynolds Shear Stress Extrapolation for 16 cfs 75
Figure 4.10 Comparison of Shear Stress from Preston Tube and Reynolds Shear Stress Extrapolation for 20 cfs 75
Figure 4.11 Averaged Percentage Difference between Preston Tube and Reynolds Shear Extrapolation with Change of Discharge 76
Figure 4.12 Comparison of Shear Stress from Linear Regression and Reynolds Shear Stress Extrapolation for 8 cfs 78
Figure 4.13 Comparison of Shear Stress from Linear Regression and Reynolds Shear Stress Extrapolation for 12 cfs 78
Figure 4.14 Comparison of Shear Stress from Linear Regression and Reynolds Shear Stress Extrapolation for 16 cfs 79
Figure 4.15 Comparison of Shear Stress from Linear Regression and Reynolds Shear Stress Extrapolation for 20 cfs 79
Figure 4.16 Averaged Percentage Difference between Reynolds Shear Extrapolation and Linear Regression with Change of Discharge 80
Figure 4.17 Percentage Difference of Maximum Shear Stress with Preston Tube for 8 cfs 82
Figure 4.18 Percentage Difference of Maximum Shear Stress with Preston Tube for 12 cfs 82

Figure 4.19 Percentage Difference of Maximum Shear Stress with Preston Tube for 16 cfs 83
Figure 4.20 Percentage Difference of Maximum Shear Stress with Preston Tube for 20 cfs 83
Figure 4.21 K_b Plots from the Ratio of Maximum Shear Stress from Preston Tube to Cross Section Averaged Shear Stress from HEC-RAS 86
Figure 4.22 K_b Plots from the Ratio of Maximum Shear Stress from Reynolds Shear Stress to Cross Section Averaged Shear Stress from HEC-RAS 87
Figure A.1 Schematic View of the Physical Model 98
Figure A.2 The Type of the Bend of the Study Reach (from Heintz 2002) 99
Figure A.3 Sketch of the Main Channel 100
Figure A.4 Schematic Sketch of Hydromachinery Laboratory 101
Figure A.5 4 ft High Walls of the Model 102
Figure A.6 Skeleton of the Main Channel and Filling Material of Main Channel 103
Figure A.7 Leveling of Fill Sand of the Main Channel 103
Figure A.8 Installation of Steel Flashing 104
Figure A.9 Concrete Placement for Model Construction 105
Figure A.10 Concrete Broom Finish for Desired Channel Roughness 105
Figure A.11 SIGNET Meters and Electronic Display Boxes (from Kinzli, 2005) 106
Figure A.12 Point Gauge Installation for Flow Depth Measurement 107
Figure A.13 The Location of Piezometer Type 1 and Type 3 Bend (from Heintz, 2002) 108
Figure A.14 Installation of Piezometer for Flow Depth Measurement 108
Figure A.15 Stilling wells for water surface elevation measurement 109
Figure A.16 Photograph of ADV (from Heintz 2002) 110
Figure A.17 Installation of ADV in Data Collection Cart 111
Figure A.18 Preston Tube for Shear Stress Measurement (from Sclafani (2008)) 112
Figure A.19 Stop Log Installation of the Model 113
Figure A.20 Stop Log for Calibration of the Model 113
Figure A.21 Test Program of Baseline Condition 114
Figure C.1 Shear Stress Distribution τ_x, by Linear Regression for 8 cfs (psf) 125
Figure C.2 Shear Stress Distribution τ_x, by Linear Regression for 12 cfs (psf) 126
Figure C.3 Shear Stress Distribution, τ_x, by Linear Regression for 16 cfs (psf) 127
Figure C.4 Shear Stress Distribution, τ_y, by Linear Regression for 8 cfs (psf) 128
Figure C.5 Shear Stress Distribution, τ_y, by Linear Regression for 12 cfs (psf) 129
Figure C.6 Shear Stress Distribution, τ_y, by Linear Regression for 16 cfs (psf) 130
Figure D.1 Radial Shear Stress Distribution, τ_r, from Rozovskii (1961) for 8 cfs (psf) 136
Figure D.2 Radial Shear Stress Distribution, τ_r, from Rozovskii (1961) for 12 cfs (psf) 137
Figure D.3 Radial Shear Stress Distribution, τ_r, from Rozovskii (1961) for 16 cfs (psf) 138
Figure D.4 Water Surface Slope Distribution for 8 cfs 139
Figure D.5 Water Surface Slope Distribution for 12 cfs 140
Figure D.6 Water Surface Slope Distribution for 16 cfs 141

Figure F.1 Comparison of Shear Stress from Preston Tube and Rozovskii Method for 8 cfs 154
Figure F.2 Comparison of Shear Stress from Preston Tube and Rozovskii Method for 12 cfs 154
Figure F.3 Comparison of Shear Stress from Preston Tube and Rozovskii Method for 16 cfs 155
Figure F.4 Comparison of Shear Stress from Preston Tube and Rozovskii Method for 20 cfs 155
Figure G.1 Comparison of Shear Stress Maximum Values (8 cfs Upstream) 157
Figure G.2 Comparison of Shear Stress Maximum Values (8 cfs Downstream) 158
Figure G.3 Comparison of Shear Stress Maximum Values (12 cfs Upstream) 158
Figure G.4 Comparison of Shear Stress Maximum Values (12 cfs Downstream) .. 159
Figure G.5 Comparison of Shear Stress Maximum Values (16 cfs Upstream) 159
Figure G.6 Comparison of Shear Stress Maximum Values (16 cfs Downstream) .. 160
Figure G.7 Comparison of Shear Stress Maximum Values (20 cfs Upstream) 160
Figure G.8 Comparison of Shear Stress Maximum Values (20 cfs Downstream) .. 161

List of Tables

Table 2.1 Dimension of the Pitot Tubes (from Preston (1954)) 20
Table 2.2 Geometric Information of Flume (from Ippen and Drinker (1962)) 24
Table 2.3 Summary of Experiment Results of Flow in Bend (from Rozovskii, 1961) 34
Table 4.1 Calculation Results of Percentage Difference between Preston Tube and Linear Regression of Linear Flow Velocity Profile.. 72
Table 4.2 Calculation Results of Percentage Difference between Linear Regression and Rozovskii Method 73
Table 4.3 Calculation Results of Percentage Difference between Preston Tube and Reynolds Shear Extrapolation.. 77
Table 4.4 Calculation Results of Percentage Difference between Linear Regression of longitudinal velocity and Reynolds Shear Extrapolation... 81
Table 4.5 HEC-RAS Output for Shear Stress for Upstream Bend (psf)..................... 85
Table 4.6 HEC-RAS Output for Shear Stress for Downstream Bend (psf)................ 85
Table 4.7 K_b Value from Maximum Shear Stress of Reynolds Shear Stress 85
Table 4.8 K_b Value from Maximum Shear Stress of Preston Tube 85
Table A.1 The Geometry of the Prototype of Study Reach (from Heintz 2002)........ 99
Table A.2 The Geometry Information of the Physical Model (from Heintz 2002).... 99
Table B.1 Shear Stress from Preston Tube Calibration for 8 cfs.............................. 116
Table B.2 Shear Stress from Preston Tube Calibration for 12 cfs........................... 117
Table B.3 Shear Stress from Preston Tube Calibration for 16 cfs........................... 118
Table B.4 Shear Stress from Preston Tube Calibration for 20 cfs........................... 119
Table C.1 Shear Stress (τ_x) from Linear Regression of Flow Velocity Profile for 8 cfs 121
Table C.2 Shear Stress (τ_x) from Linear Regression of Flow Velocity Profile for 12 cfs 122
Table C.3 Shear Stress (τ_x) from Linear Regression of Flow Velocity Profile for 16 cfs 123
Table C.4 Shear Stress (τ_x) from Linear Regression of Flow Velocity Profile for 20 cfs 124
Table D.1 Shear stress (τ_y) from Rozovskii (1961) Method for 8 cfs 132
Table D.2 Shear stress (τ_y) from Rozovskii (1961) Method for 12 cfs 133
Table D.3 Shear stress (τ_y) from Rozovskii (1961) Method for 16 cfs 134
Table D.4 Shear stress (τ_y) from Rozovskii (1961) Method for 20 cfs 135
Table E.1 Reynolds Shear Stress Calculation Summary for 8 cfs (psf) 144
Table E.2 Reynolds Shear Stress Calculation Summary of Upstream Bend for 12 cfs (psf) 145
Table E.3 Reynolds Shear Stress Calculation Summary of Downstream Bend for 12 cfs (psf) 146
Table E.4 Reynolds Shear Stress Calculation Summary of Upstream Bend for 16 cfs (psf) 147
Table E.5 Reynolds Shear Stress Calculation Summary of XS 10 ~ XS 15 for 16 cfs (psf) 148

Table E.6 Reynolds Shear Stress Calculation Summary of XS 16 ~ XS 17 for 16 cfs (psf) 149
Table E.7 Reynolds Shear Stress Calculation Summary of Upstream Bend for 20 cfs (psf) 150
Table E.8 Reynolds Shear Stress Calculation Summary of XS 10 ~ XS 15 for 20 cfs (psf) 151
Table E.9 Reynolds Shear Stress Calculation Summary of XS 16 ~ XS 17 for 20 cfs (psf) 152

List of Symbols

A = cross sectional flow area (L^2)
α = shear stress by Preston tube (M/L^2)
b = the intercept of the regression line of Reynolds Shear Stress (Dimensionless)
β = shear stress from linear regression of flow velocity profile (M/L^2)
β_1 = shear stress from the Rozovskii method (M/L^2)
β_2 = shear stress from Reynolds shear stress extrapolation (M/L^2)
COV-XY = the covariance of two variables (V_x and V_y) (Dimensionless)
COV-YX = the covariance of two variables (V_x and V_y) (Dimensionless)
COV-XZ = the covariance of two variables (V_x and V_Z) (Dimensionless)
COV-ZX = the covariance of two variables (V_x and V_Z) (Dimensionless)
COV-ZY = the covariance of two variables (V_z and V_y) (Dimensionless)
COV-YZ = the covariance of two variables (V_z and V_y) (Dimensionless)
D = horizontal distance of piezo between a and Piezo g (L)
D = internal diameter of pipe (L)
d = the outer diameter of pitot tube (L)
d_1 = 3 times of the difference of height of Piezo a and d (L)
d_2 = Channel bottom width (L)
d_3 = 3 times of the difference of height of Piezo g and d (L)
δ = the percentage difference of shear stress between Preston tube and linear regression of flow velocity profile (Dimensionless)
δ_1 = the percentage difference between Preston tube and Rozovskii Method (Dimensionless)
δ_2 = the percentage difference between Preston tube and Reynolds Shear Stress Extrapolation (Dimensionless)
∂p = the differential pressure (M/L^2)
∂r = the differential radius of curvature (L)
g = the acceleration of gravity (L/T^2)
γ = specific gravity of water (M/L^3)
H = the flow depth (L)
h = Difference of water surface elevation between piezo a and g (L)
k_s = the grain roughness. (Dimensionless)
κ = the constant of Von Karman (Dimensionless)
K_b = the ratio of maximum shear stress to averaged shear stress (Dimensionless)
L = the length of test section (L)
Lc = the Channel Length (L)
Lv = Straight Line Valley Length of a channel (L)
n = the number of samples that collected velocity data (Dimensionless)
P = the dynamic pressure (M/L^2)
p_o = the static pressure (M/L^2)

p_t = the impact pressure (M/L^2)
Δp = the dynamic pressure (L)
R = hydraulic Radius (L)
R_c = radius of curvature of meandering channel (L)
r = the radius of curvature of the channel bend (L)
r_{ce} = the center radius of curvature in bend (L)
r_i = the inner radius of curvature in bend (L)
r_o = the outer radius of curvature in bend (L)
ρ = the mass density of water (M/L^3)
S = the lope of the Regression Equation of Velocity Profile
S_o = the bed slope of channel (L/L)
Sr = the water surface elevation (L/L)
T_w = top width of channel (L)
τ_{bed} = the turbulent shear stress in longitudinal direction that applies on the bed of the channel (M/L^1T^2)
τ_o = bed shear stress (ML^{-2})
τ_r = the radial shear stress ($ML^{-1}T^{-2}$)
τ_{xy} = The turbulent shear stress that applies in y axis and caused by V_x (M/L^1T^2)
τ_{yx} = The turbulent shear stress that applies in x axis and caused by V_y (M/L^1T^2)
τ_{zx} = The turbulent shear stress that applies in x axis caused by V_z (M/L^1T^2)
τ_{xz} = The turbulent shear stress that applies in z axis and caused by V_x (M/L^1T^2)
τ_{yz} = The turbulent shear stress that applies in z axis and caused by V_y (M/L^1T^2)
τ_{zy} = The turbulent shear stress that applies in y axis and caused by V_z (M/L^1T^2)
τ_{xx} = The normal force that applies in x axis and caused by V_x (M/L^1T^2)
τ_{yy} = The normal force that applies in y axis and caused by V_y (M/L^1T^2)
τ_{zz} = The normal force that applies in z axis and caused by V_y (M/L^1T^2)
$\bar{U}$ = The vertical averaged streamwise velocity (LT^{-1})
U^* = The velocity scaling parameter for log law, identical with u_* for uniform 2D flow (L/T)
u = Flow velocity (L/T)
u_* = Shear velocity (L/T)
υ = the kinematic viscosity of water (L^2/T)
V_x = The flow velocity along x-axis (L/T)
V_y = The flow velocity along y-axis (L/T)
V_z = The flow velocity along z-axis (L/T)
v_θ = the flow velocity along the bend of the channel (L/T)
v_1 = Flow velocity value that locates in the lowest data collection point (L/T)
v_2 = Flow velocity value that locates just above of the location of v_1 (L/T)

v_n = Flow velocity value that locates in the highest point (L/T)
x = the Preston differential pressure (L)
y = the distance normal to the plane of the channel bottom (L)
z = the vertical distance the bottom of the channel (L)
z_{Bed} = Bed elevation of the Channel (L)
ΔZ = Differential flow depth (L)

1 Introduction

1.1 Background

Natural channels never stop changing their geomorphic characteristics. Natural alluvial streams are similar to living creatures because they generate water flow, develop point bars, alter bed profile, scour the bed, erode the bank, and cause other phenomena in the stream system. The geomorphic changes in a natural system lead to a wide array of research worldwide, because methods of predicting channel change are limited. Bank erosion due to meandering of the channel is a critical issue in modern river engineering. In the United States, the severity of the problem was recognized when Congress enacted the Streambank Erosion Control Evaluation and Demonstration Act of 1974 and authorized research in the field (Odgaard 1986). The increased demand for bank erosion research resulted in many theoretical and experimental studies to predict geomorphic changes in natural channels. Julien (2002) describes the magnitude and orientation of applied shear stress as one of the main factors of bank erosion. Julien (2002) also describes the damping of shear stress by erosion control.

1.2 Project Background

The 29-mile-long study reach of Rio Grande River was located in central New Mexico. The study reach was a straight braided system with a shifting sand bed and shallow banks (Heintz 2002). The high supply of sediment caused channelization of the river. Cochiti dam was constructed by the U.S Army Corps of Engineers for the purposes of flood and sediment transport control for the Albuquerque area in 1973 (Schmidt, 2005). Subsequently, the channel changed from an aggrading to degrading system. As a result, the planform geometry of the reach has changed from a straight braided to active meandering system (Heintz 2002). Channel meandering resulted in bank erosion and lateral migration. Bank erosion and lateral channel migration occurred to satisfy quasi-equilibrium conditions of the stream system. Fish habitat, vegetation, and infrastructure around the stream and farming lands were threatened due to the bank erosion.

Understanding shear stress distribution in the study reach is necessary because shear stress is the key parameter to predict bank erosion and lateral channel migration. Shear stress distribution was investigated through physical modeling conducted by Colorado State University (CSU). For testing purposes, a 1:12 Froude scale model was constructed and tested in the Hydromachinery Laboratory that is located at the Engineering Research Center (ERC) in CSU. The purpose of the physical modeling was to simulate conditions in the reach and to predict the shear stress distribution at four target flow rates: 8, 12, 16 and 20 cubic feet per second (cfs). Laboratory tests were performed in baseline test conditions without installing hydraulic structures in the main channel.

1.3 Research Objectives

The focus of this study was shear stress distribution analysis in meandering channels via the following methods: 1) Preston tube; 2) linear regression of velocity profile; 3) Rozovskii Method; and 4) Reynolds shear stress extrapolation.

The objectives of the study were to:

a) Understand in detail the shear stress distribution mechanism for meandering channels by performing a physical model study;
b) Calculate shear stress by using four different methods;
c) Compare the different shear stress values;
d) Recommend the most appropriate shear stress calculation method for the establishment of a design guide for channels in the field.

The scope of the research was defined to satisfy the objectives:

a) A comprehensive literature review of previous studies about the shear stress calculation methods in meandering channel;
b) Analysis of the collected data to calculate shear stress distribution in meandering channel;
c) Compare and discuss the different shear stress calculation methods;
d) Recommend the most appropriate shear stress analysis method and direction of future research.

2 Literature Review

2.1 Introduction

Flow in a meandering channel results in geomorphic changes. A picture of a typical meandering channel is presented in Figure 2.1. Flow in meandering channels results in geomorphic changes, such as bank erosion. Implementation of bank protection to prevent erosion is a significant economic expense. Therefore, a development of a tool for bank implementation is important. This tool would be used to predict shear stress, which is the most important aspect of back erosion. Since the beginning of the 20th century, many researchers have developed methods for the analysis of flow in bends. The literature review provides an explanation of the basic concepts of fluvial geomorphology, Preston tube method, Rozovskii's shear calculation, linear regression of flow velocity profile, and Reynolds shear stress about flow in a bend.

Figure 2.1 Typical Meandering Channel (from Watson et al. (2005))

2.2 Open Channel Flow in Meandering Bends

To study flow characteristics in a meandering alluvial channel, a basic understanding of a meandering channel is needed. This section covers the background of meandering channel geometry, flow patterns in bends, erosion patterns and channel stability.

2.2.1 Meandering Channel Geometry

Sinuosity is used to describe a meandering channel. When sinuosity is greater than 1.5, the channel is classified as meandering (Knighton 1998). Equation 2.1 describes the method used for calculating channel sinuosity:

$$Sinuosity = \frac{L_c}{L_v} \qquad \textbf{Equation 2.1}$$

Where, L_c = the channel length; and

L_v = the straight line valley length.

There are two methods available to analyze meander geometry (Knighton 1998). The first method focused on the individual bend statistics: meander wavelength (L) and radius of curvature (r_c), which are averaged over a series of bends. The second method is a series approach method that spans sequences of bends and treats the stream trace as a spatial series of flow direction (arc angle θ) or differential change of flow direction ($\Delta\theta$) along the reach (Knighton 1998). For meandering channels, Knighton (1998) states that the second method provides more flexibility for flow characteristics analysis and theoretical model development. Figure 2.2 presents the geometry of meandering channel.

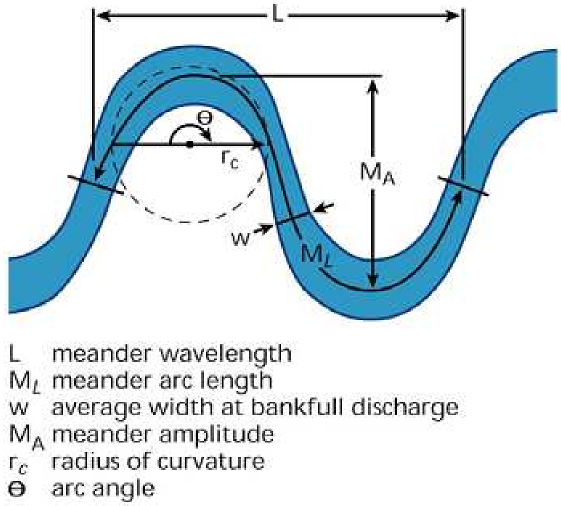

Figure 2.2 Geometry of Meandering Channel (from Watson et al. (2005))

A sine-generated curve is used to develop a simple model of meandering channel, as described by equation 2.2. A pictorial representation of the sine-generated curve is provided in Figure 2.3.

$$\theta = \omega \sin kx \qquad \textbf{Equation 2.2}$$

Where, θ = channel direction;

x = flow distance along the reach;

ω = the maximum angle between a channel segment and the mean downvalley axis; and

k = the ratio of 2π to the meander wavelength.

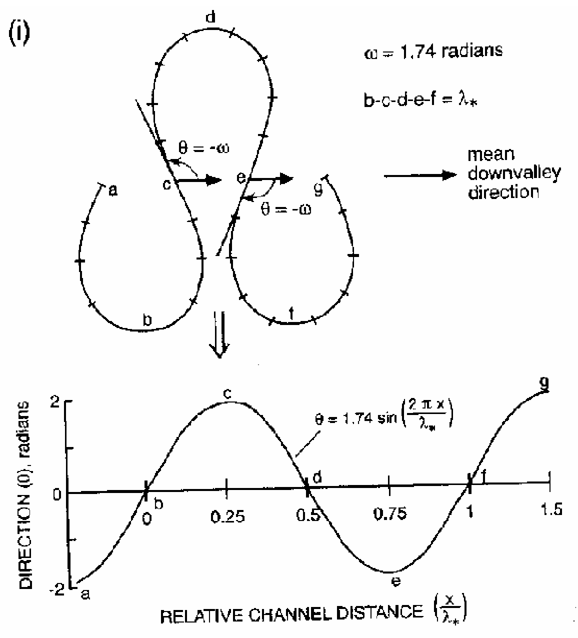

Figure 2.3 Description of Sine-Generated Curve Function (from Knighton (1998))

2.2.2 Flow Patterns in Meandering Channels

The description of flow patterns in a meandering channel has three components; stream morphology, transverse velocity distribution in bends, and superelevation of the water surface against the outside of the bank. This section explains the three main components of flow patterns in meandering channels.

2.2.2.1 Stream Morphology

A geomorphic sketch of a straight and meandering channel is presented in Figure 2.4. Pool-riffle sequences are the characteristics of cobble, gravel and mixed load rivers of moderate gradient (smaller than 5%) (Sear 1996). Topographic high points are defined as riffles and low points are defined as pools (Watson, et al. (2005)). The grain sizes found in riffles are larger than pools. Keller (1971) explained that the reason for the difference in grain size is caused by the sorting process. In addition, Keller (1971) explains that fine sediments are removed from riffles during low flows due to flow velocity and shear stress. These sediments are then deposited in pools. Normally, the outer side of the bank is deeper than the inside bank, forming a point bar at the inside bank. In addition, the following features are also observed in natural streams: point bars, middle bars, alternate bars and braiding. Figure 2.5 shows a typical meandering stream with point bars.

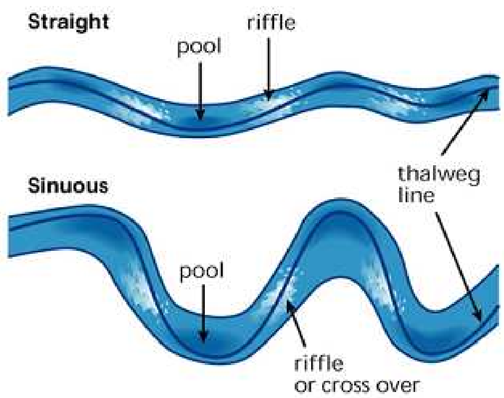

Figure 2.4 Schematic Description of Straight Channel and Meandering Channel (from Federal Interagency Stream Restoration Working Group (FISHRWG) (1998)).

Figure 2.5 A typical meandering stream with point bars (from Watson et al. (2005))

Point bars form at the inside bank of a bend as seen in Figure 2.5. The factors which influence the formation of point bars are flow characteristics, degree of sinuosity, and sediment transportation. Reduction of sediment transport capacity at the inside of the bank, transverse flow velocity distribution and secondary currents in bends result in the formation of point bars (Watson et al. (2005)). A pictorial representation of a middle bar is shown in Figure 2.6. A middle bar is a depositional feature located within the channel, but not connected to the banks.

Figure 2.6 Typical Middle Bar (from Watson et al. (2005))

Alternate bars are regularly-spaced depositional features that are located in the opposite sides of a straight or slightly sinuous stream (Watson et al. (2005)). Figure 2.7 presents the typical shape of alternate bars. Alternate bars are good indicator of the initiation of a meander or braided planform (Watson et al. (2005)). Figure 2.8 shows a braided river, which is composed of a straight channel with multi-threads. In the case of braid bars, the mobility is very high.

Figure 2.7 Typical Alternate Bars (from Watson et al. (2005))

Figure 2.8 Typical Braid Bars (from Watson et al. (2005))

2.2.2.2 Transverse Velocity Distribution in Bends

Imbalance in radial pressure around the bend causes the transverse velocity distribution in a meandering channel (FHWA (Federal Highway Administration) 2001). Figure 2.9 represents a typical cross section within a bend and the velocity distribution. The radial forces that act on the shaded control volume are the centrifugal force that was presented in Equation 2.3 (FHWA 2001):

$$F_c = \frac{mv^2}{r} \qquad \textbf{Equation 2.3}$$

Where, F_c = the centrifugal force (MLT^{-2});

r = the value of radius of curvature (L);

m = the mass of the moving object (M); and

v = the moving velocity of the object (LT^{-1}).

In addition, superelevation of the water surface, dz, results in the differential hydrostatic force γdz. Therefore, the centrifugal force is greater near the surface where the flow velocity is greater and less at the bed where the flow velocity is small (FHWA 2001). The differential hydrostatic force is constant throughout the depth of the control volume. In addition, Figure 2.9 (b) explains that the combination of centrifugal force and hydrostatic force causes a secondary flow in the bend (FHWA 2001).

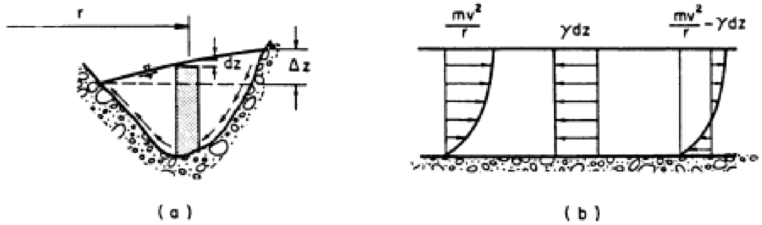

Figure 2.9 Schematic Descriptions of Flow in Meandering Channel (from FHWA (2001))

2.2.2.3 Superelevation against the Outside of the Bank

Due to the centrifugal force of flow in the bend, there is a superelevation of the water surface in the bend (FHWA 2001). The water surface elevation at the outer bank is higher than at the inside of the bank. The differential pressure in the radial direction results from the radial acceleration and can be expressed by Equation 2.4. A sketch of the flow around a bend is provided in Figure 2.10.

$$\frac{1}{\rho}\times\frac{\partial p}{\partial r}=\frac{v_\theta^2}{r}$$ **Equation 2.4**

Where, ρ = the mass density of water (M/L^3);

∂p = the differential pressure (M/L^2);

∂r = the differential radius of curvature (L); and

v_θ = the flow velocity along the bend of a channel (L/T).

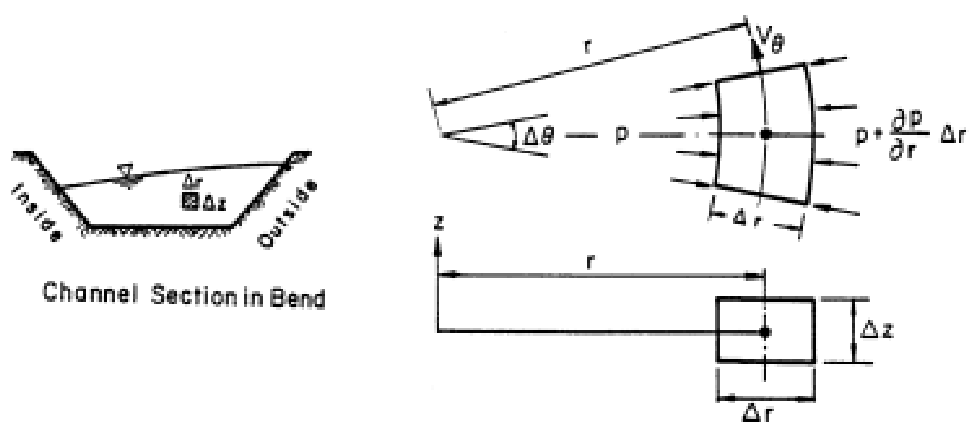

Figure 2.10 Sketch of the flow around bend (from FHWA (2001))

For the calculation of the superelevation, two assumptions should be made;

a) The magnitudes of radial and vertical velocities are smaller than tangential velocities.

b) Distribution of pressure in the bend is hydrostatic.

If the two assumptions are satisfied, it is possible to calculate the superelevation by using Equation 2.5.

$$\Delta Z = \frac{V_{\max}^2}{2g}\left(2 - \left(\frac{r_i}{r_{ce}}\right)^2 - \left(\frac{r_{ce}}{r_o}\right)^2\right)$$ **Equation 2.5**

Where, ΔZ = height of superelevation (L);

$V_{\max}^2$ = maximum flow velocity (L^2/T^2);

g = acceleration of the gravity (L/T^2);

r_i = the inner radius of curvature in bend (L);

r_{ce} = center radius of curvature in bend (L); and

r_o = outer radius of curvature in bend (L).

2.2.3 Erosion Patterns in Meandering Rivers

Figure 2.11 shows the geomorphic change of a straight channel into a meandering channel. There are four stages to change a straight channel into a meandering channel (after Keller, 1972):

a) Alternating bars dominant. (Stage 1)

b) Development of incipient pools and riffles (Stage 2)

c) Development of well-developed pools and riffles with a mean spacing of 5 to 7 channel widths. (Stage 3)

d) Development of meandering channel with riffles at inflection points and pools at bend apices where bank erosion is concentrated. (Stage 4)

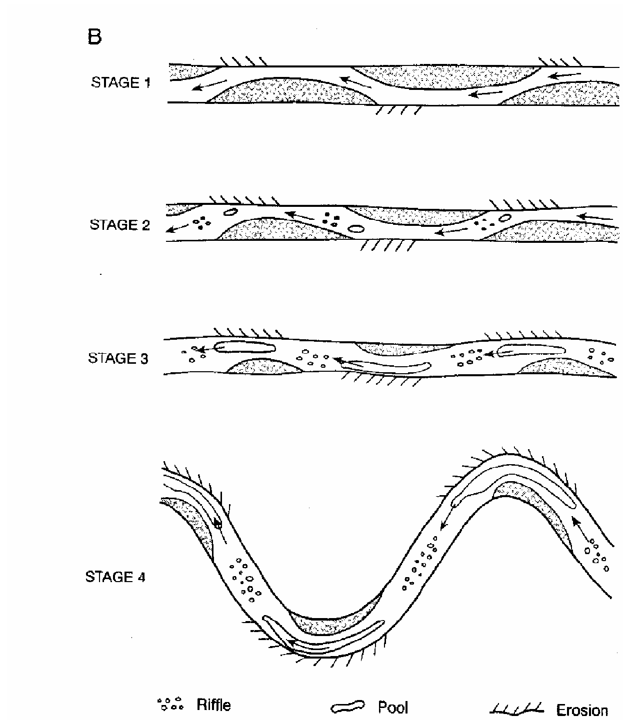

Figure 2.11 Geomorphic Change of Straight Channel into Meandering Channel (from Knighton, (1998))

In addition, Knighton (1998) explained that the relationship between flow and geomorphic form has a link with the radius of the curvature versus width relationship, which can alter flow pattern in meandering channel. Bagnold (1960) claimed that if the ratio of radius of curvature and channel width is smaller than 2, water filaments begin to separate from the inner bank. Hickin and Nanson (1975) suggested that there is a corresponding reduction in the rate of erosion at the concave bank. Hickin and Nanson (1986) plotted the relationship of relative migration rate to bend curvature for 18 rivers (Figure 2.12)

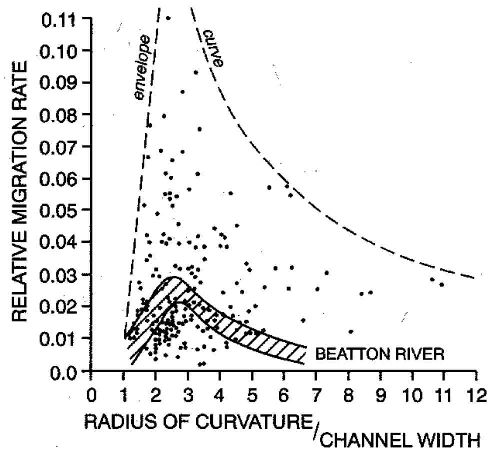

Figure 2.12 The relationship of relative migration rate to bend curvature for 18 rivers (from Knighton (1998))

It is hard to predict the planform of the channel, but the U.S Federal Highway Administration (2001) suggested the modes of meander loop development will aid in planform prediction. Figure 2.13 presents the seven modes of the meander loop development. These modes are: A) Extension B) Translation C) Rotation D) Conversion to a compound loop E) Neck cutoff by closure F) Diagonal cutoff by chute G) Neck cutoff by chute (FHWA (2001)).

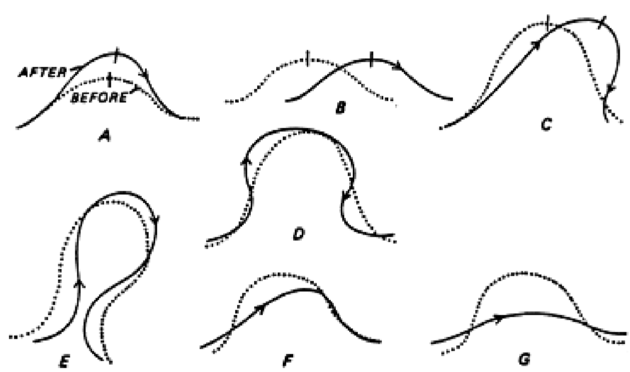

Figure 2.13 Seven Modes of Meander Loop Development (from FHWA (2001))

2.2.4 Channel Stability

It is possible to classify the stream system as stable or unstable. The criterion of the classification depends on whether the stream has adjusted or is still adjusting to the flow and sediment regimes (FHWA 2001). A graded stream is defined as a stream that is not necessarily static or fixed and may exhibit temporary morphological changes in response to the impacts of extreme events. The main attitude of a graded stream is that fluvial processes operating under formative flows tend to restore stream morphology to the graded condition (FHWA 2001). This type of stability is described as dynamic equilibrium. To explain the concept of dynamic equilibrium, the concept of Lane's balance (1955) is commonly used. The schematic sketch of Lane's balance is provided in Figure 2.14. Lane's balance shows the change of the following four variables: Q, S, Q_s and D_{50}. If one or more of these variables change, the river will responded by causing a change in the other variables to restore equilibrium.

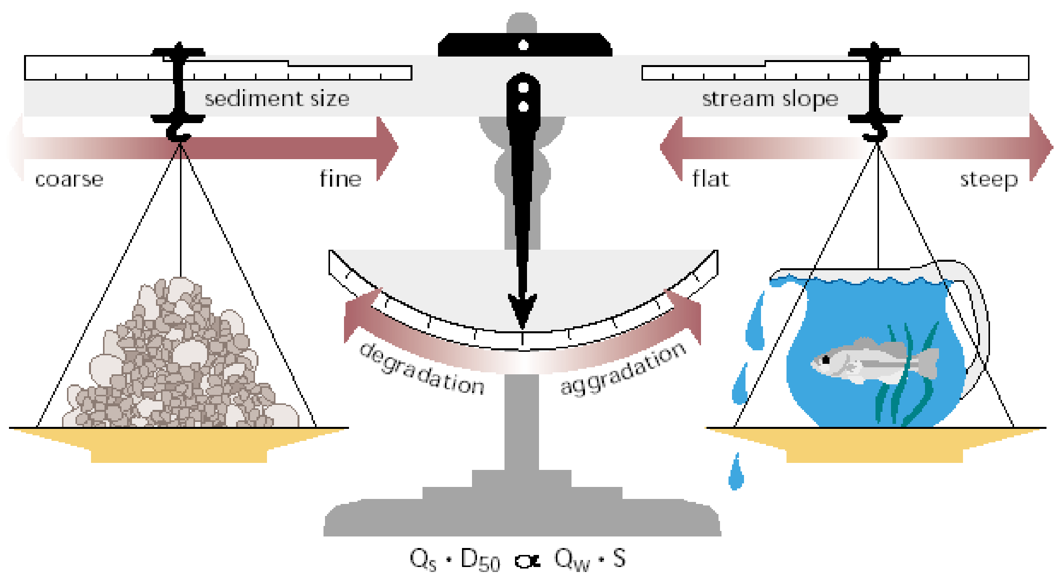

Figure 2.14 Lane's Balance (from Rosgen (1996))

The following equation describes Lane's balance;

$$QS \sim Q_s D_{50} \qquad \textbf{Equation 2.6}$$

Where, Q = water flow rate (L^3/T);

S = slope (L/L);

Q_s = sediment flow rate (M/T); and

D_{50} = median size of bed material (L).

2.3 Shear Stress Calculation Methods

Calculation methods of shear stress in meandering channels have been suggested by many researchers. In this section, the techniques for calculating shear stress using the concept of Reynolds shear stress, Rozovskii method, linear regression of flow velocity profile method and Preston tube method will be introduced.

2.3.1 Preston Tube

Preston tube method computes shear stress by locating a Preston tube directly on the bed of the channel at the point of measurement. After data collection, calibration was performed to convert data from an electronic signal into bed shear stress.

2.3.1.1 Preston (1954)

Preston (1954) performed a laboratory study to determine turbulent skin friction by using pitot tubes. The purpose of the laboratory study was to calculate skin friction that applies on the surface. Before Preston (1954), Stephens and Haslam (1938) suggested the method to determine local skin friction by reading local static pressure. The relationship between local skin friction and local static pressure is presented in Equation 2.7.

$$\frac{(P - p_o) \times d^2}{\rho \nu^2} = F\left(\frac{\tau_O d^2}{\rho \nu^2}\right)$$ **Equation 2.7**

Where, F = representative linear function;

P = dynamic pressure (slug×ft/s^2);

p_o = static pressure (slug×ft/s^2);

d = pitot tube diameter taken as a representative length (ft);

ρ = mass density of water (slug/ft^3);

ν = kinematic viscosity of water (ft^2/s); and

τ_o = boundary shear stress (slug×ft/s^2).

For circular pipe, Preston (1954) explained shear stress, τ_o can be calculated from Equation 2.8.

$$\tau_o = (p_1 - p_2)\frac{D}{4L}$$ **Equation 2.8**

Where, τ_o = boundary shear stress (slug×ft/s^2);

p_1 = pressure at the beginning of length, L (slug×ft/s^2);

p_2 = pressure at the end of length, L (slug×ft/s^2);

D = internal diameter of pipe (ft); and

L = the length of test section (ft).

The instrument for data collection is presented in Figure 2.15. For the data collection, four different pitot tubes were used. The dimensions of the pitot tubes are presented in Table 2.1.

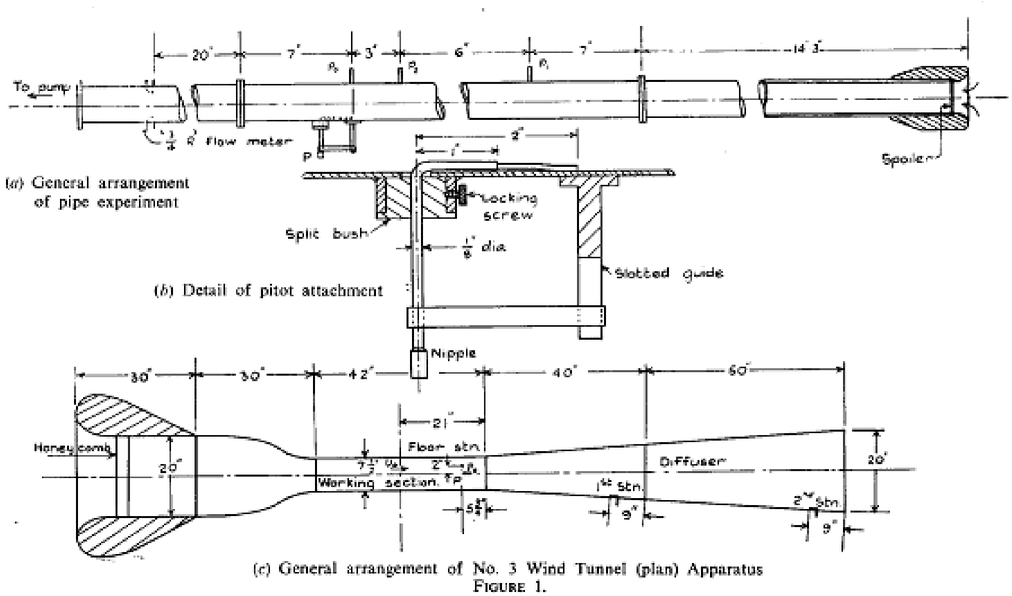

Figure 2.15 Sketch of Data Collection Facility of Preston (from Preston (1954))

Table 2.1 Dimension of the Pitot Tubes (from Preston (1954))

Pitot Tube Number	1	2	3	4
External Diameter (in)	0.02915	0.0544	0.0907	0.1214
Ratio: (Internal/External) Diameter	0.602	0.603	0.599	0.598

The result of experiments in the laboratory was presented in Figure 2.16. Preston (1954) also presents two different equations by expressing the relationship between $\log_{10}\frac{\tau_o d^2}{4\rho \upsilon^2}$ and $\frac{(p-p_o)d^2}{4\rho \upsilon^2}$ in the non-dimensional form. For the condition of $\log\frac{(p_t-p_o)^2}{4\rho \upsilon^2} > 5$, the equation is expressed in Equation 2.9 and the expression of the relationship under the condition of viscous flow was presented in Equation 2.10.

$$\log_{10}\frac{\tau_o d^2}{4\rho v^2} = 2.604 + \frac{7}{8}\times\log_{10}\frac{(p - p_o)d^2}{4\rho v^2} \qquad \textbf{Equation 2.9}$$

$$\log_{10}\frac{\tau_o d^2}{4\rho v^2} = \frac{1}{2}\left(\log_{10} 2 + \log_{10}\frac{(p - p_o)^2}{4\rho v^2}\right) \qquad \textbf{Equation 2.10}$$

Where, P = dynamic pressure (slug×ft/s^2);

p_o = static pressure (slug×ft/s^2);

d = pitot tube diameter taken as a representative length (ft);

ρ = mass density of water (slug/ft^3);

ν = kinematic viscosity of water (ft^2/s); and

τ_o = boundary shear stress (slug×ft/s^2).

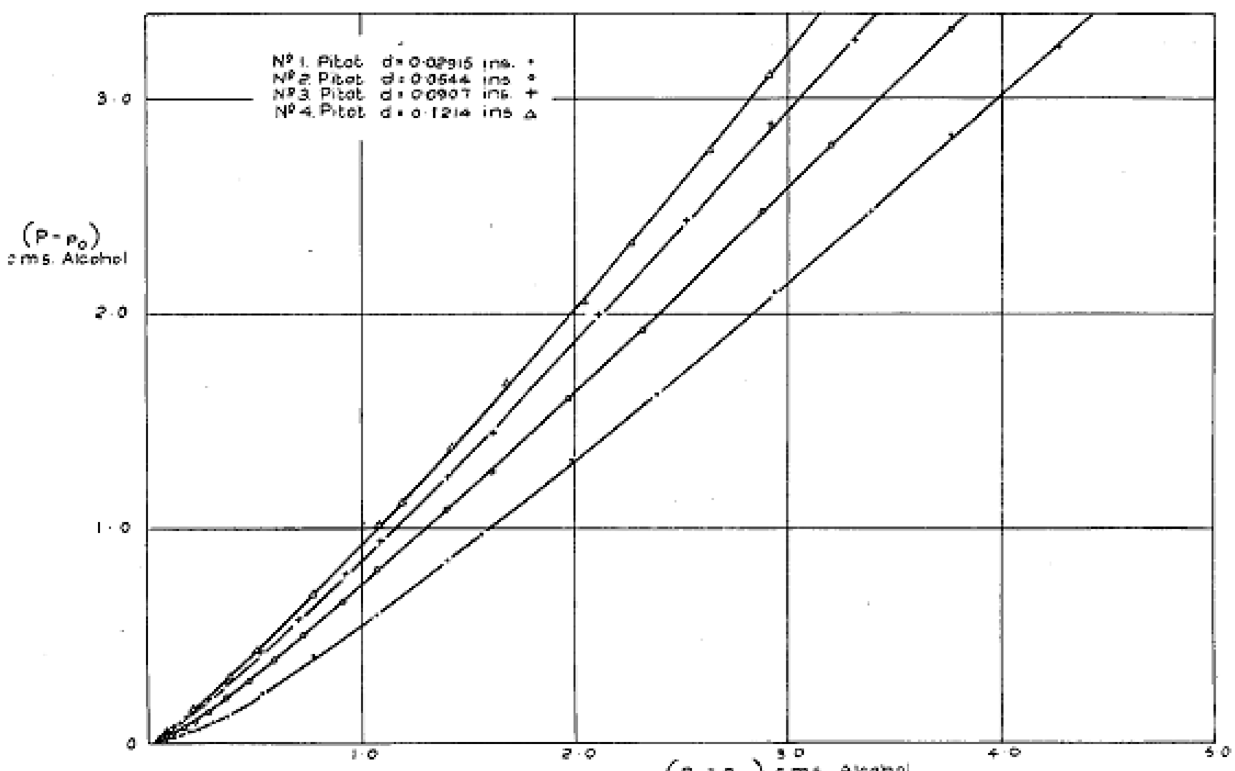

Figure 2.16 Actual Observations of round pitot on wall of circular pipe (from Preston (1954))

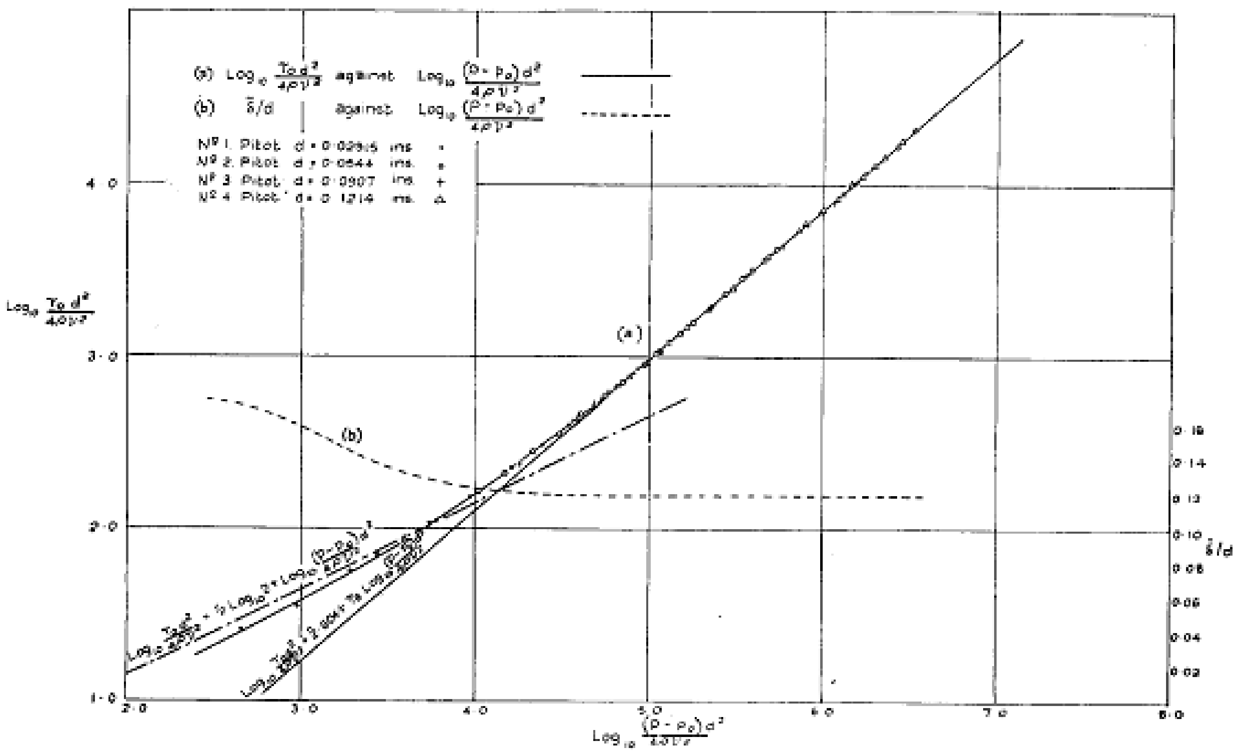

Figure 2.17 The Plot of Non-Dimensional Results of Experimentations of Preston (1954)

2.3.1.2 Ippen and Drinker (1962)

Ippen and Drinker (1962) performed laboratory experiments to correlate the impacts of shear stress on meandering channel bank erosion by using a Preston tube. Two flumes were constructed for data collection. The geometry of each flume was trapezoidal. Table 2.2 presents the geometric information of the two flumes. Figure 2.18 provides a sketch of the flumes in the laboratory.

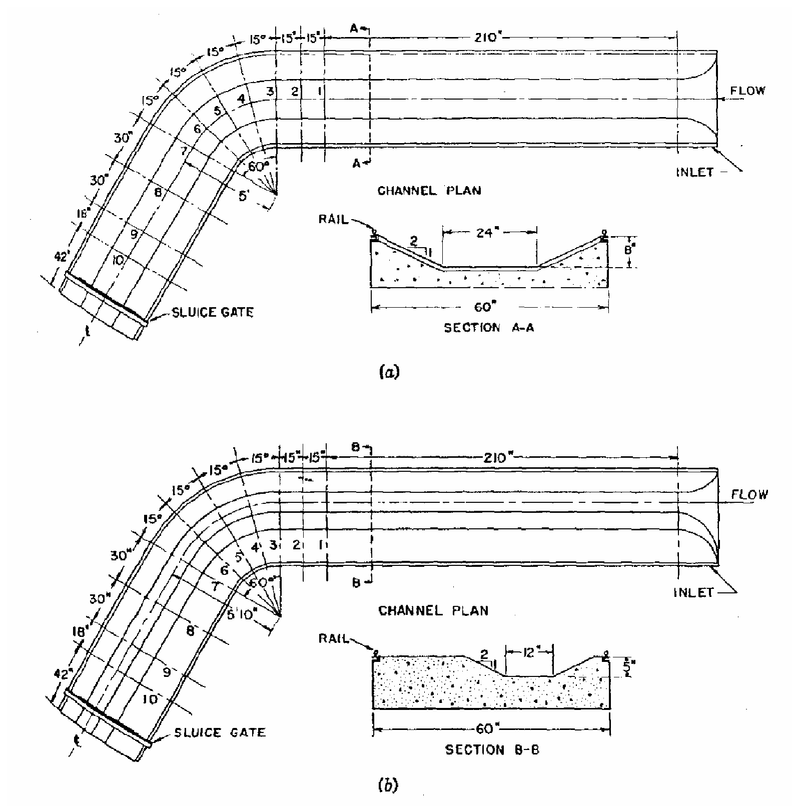

Figure 2.18 Sketches of Laboratory Flume (from Ippen and Drinker (1962))

Table 2.2 Geometric Information of Flume (from Ippen and Drinker (1962))

	Shape of Cross Section	Side Slope (Horizontal :Vertical)	Rotation Angle (Degrees)	Bottom Width (inch)	Radius of curvature (inch)
Larger Flume	Trapezoidal	2:1	60	24	60
Smaller Flume	Trapezoidal	2:1	60	12	70

For flow depth adjustment at the curve entrance, a sluice gate was installed at the exit section to control downstream flow depth. At the beginning of the experiment, the Manning's roughness coefficient was assumed as 0.009. As the experiment progressed, calculation of the roughness coefficient was conducted and the result was 0.010. To measure boundary shear stress, Ippen and Drinker (1962) selected the Preston method (1954) presented in Equation 2.11. This method computes shear stress on a smooth boundary by the pressure differential between static and dynamic pitot tubes resting on the bed surface. Ippen and Drinker (1962) calibrated the pressure head recorded in shear stress measurements in pounds per square feet by using Equation 2.11.

$$\log \frac{\tau_o d^2}{4\rho\upsilon^2} = -1.396 + 0.875 \times \log \frac{(p_t - p_o)^2}{4\rho\upsilon^2}$$ **Equation 2.11**

Where, τ_o = local boundary shear stress (psf);

d = the outer diameter of pitot tube;

ρ = the mass density of water (slug/ft^3);

υ = the kinematic viscosity of water (ft^2/sec);

p_t = the impact pressure (psf); and

p_o = the static pressure (psf).

After experimental investigation of flow in meandering channels by using a Preston tube, Ippen and Drinker (1962) drew the following conclusions;

a) The maximum value of shear stress that resulted from the curved flow is not possible to predict by theoretically or using empirical coefficient of head loss in curved flow at present.

b) During the laboratory experiments, in the case of large curvatures, a high value of shear was observed near the inside bank in the curve and near the outside bank below the curve exit.

c) The laboratory test proved that boundary shear stress distribution is an important parameter to understand erosion and deposition processes in meandering channel.

2.3.1.3 Heintz (2002)

Heintz (2002) carried out Preston tube calibration to measure shear stress in a curved channel constructed at the Engineering Research Center located at Colorado State University. A pressure transducer was used for the collection of pressure data in a trapezoidal meandering channel. Figure 2.27 presents the Preston tube and pressure transducer that were used in the calibration. Equation 2.12 was obtained after Preston tube calibration.

$$\tau = 0.02788 \times \gamma \times \Delta p \qquad \textbf{Equation 2.12}$$

Where, τ = the shear stress (psf);

γ = the specific gravity of water (lb/ft^3); and

Δp = the dynamic pressure ft of H_2O.

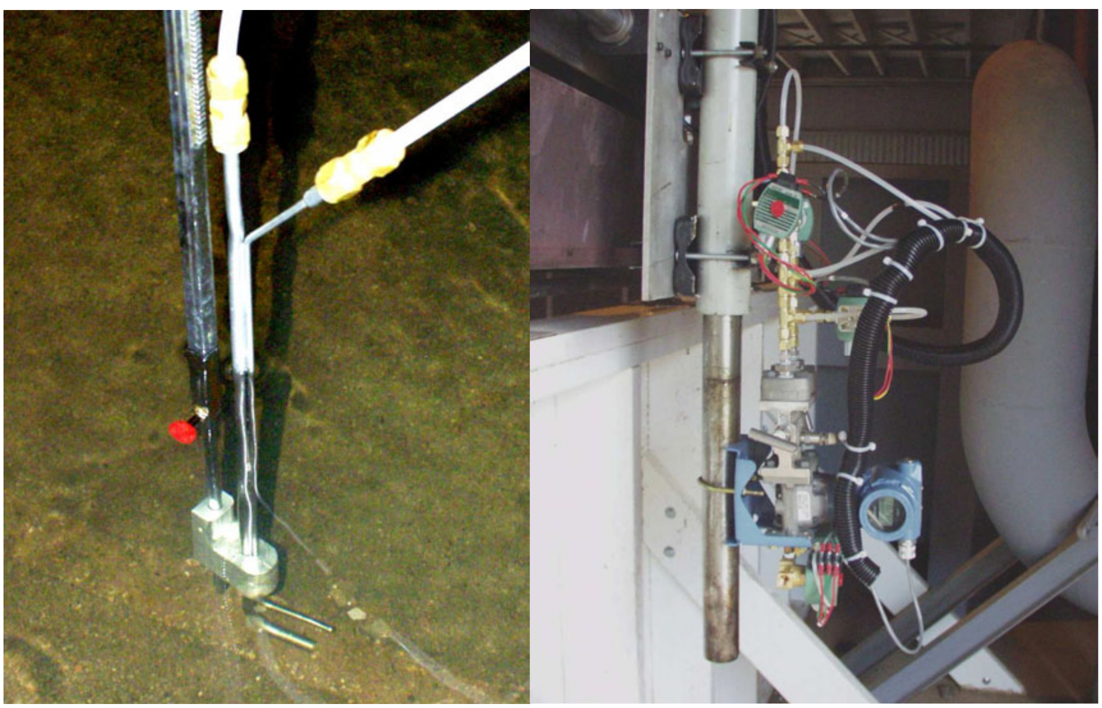

Figure 2.19 Preston Tube for Shear Stress Measurement (at left) and Pressure Transducer (at right) (from Heintz 2002)

2.3.1.4 Sclafani (2008)

Sclafani (2008) carried out another Preston tube calibration in the Engineering Research Center in Colorado State University. Sclafani (2008) explained that the purpose of the second Preston tube calibration was to overcome the limitation of the meandering channel geometry and to develop uniform flow completely in the flume. The Preston tube was installed and calibrated in a 60-foot long, 4-foot wide, 2.5-foot tall flume (Sclafani (2008)).

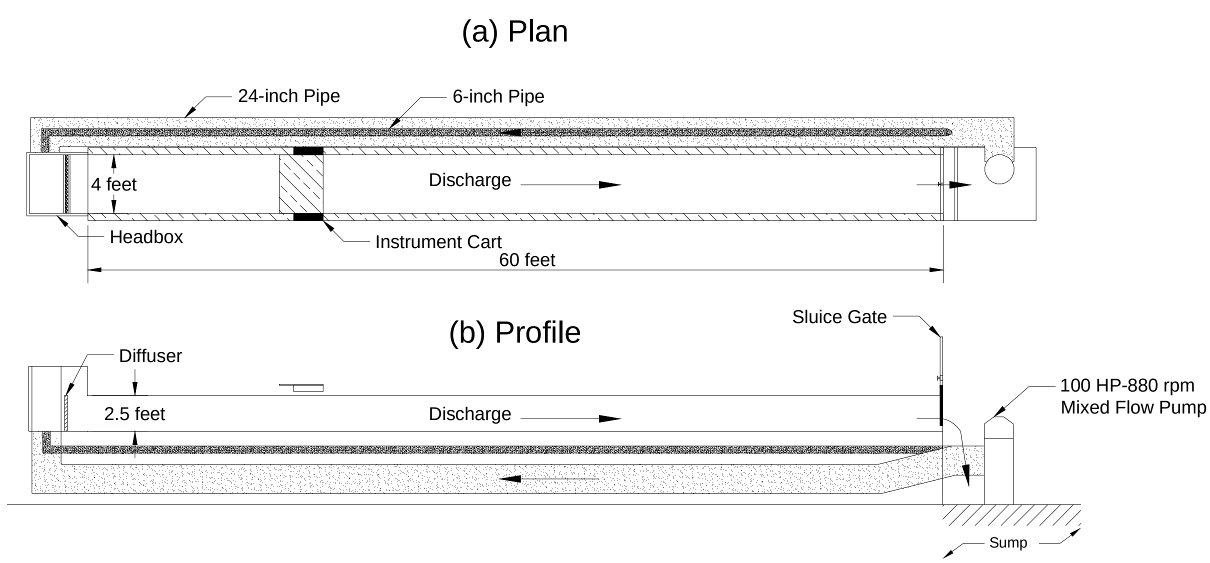

Figure 2.20 Schematic Sketch of the Flume (Sclafani (2008))

After the second Preston tube calibration, Sclafani (2008) obtained a close relationship between differential pressure and bed shear stress presented in Equation 2.13.

$$\tau = 0.1644 \times dp \qquad \textbf{Equation 2.13}$$

Where, τ = the shear stress (psf); and

dp = the differential pressure (in).

2.3.2 Linear Regression of Flow Velocity Profile

Linear regression of flow velocity profile method for shear stress calculation is based on the relationship between the logarithmic profile of flow depth and flow velocity. In this section, relevant studies of the method will be presented.

2.3.2.1 Clauser (1956)

Shear velocity can be calculated using Equation 2.14. If Equation 2.14 is rearranged, it is possible to obtain shear stress.

$$u_* = \sqrt{\frac{\tau_o}{\rho}}$$ **Equation 2.14**

Where, u_* = the shear velocity. (LT^{-1})

τ_o = the bed shear stress. (ML^{-2})

ρ = the mass density of water. (ML^{-3})

According to Clauser (1956), shear velocity can be obtained by taking linear regression between mean point velocity, u and natural log of $\left[\left(y + \frac{y + 0.2d_{50}}{d_{50}}\right)\right] + B$

$$u = \alpha \times \ln\left[\left(y + \frac{y + 0.2d_{50}}{d_{50}}\right)\right] + B$$ **Equation 2.15**

Where, α and B = the slope and intercept of the linear regression respectively (Dimensionless);

y = the distance normal to the plane of the channel bottom (L); and

d_{50} = the grain size for 50 % of the material weight is finer. (L)

Also, Afzalimehr and Anctil (2000) explained combination of law of the wall with Equation 2.15 generates Equation 2.16 to estimate shear velocity. The result of this combination is presented in Equation 2.16.

$$\frac{u}{u_*} = \frac{1}{\kappa} \times \ln\left[\left(\frac{y + 0.2 \times d_{50}}{k_s}\right)\right] + B \qquad \textbf{Equation 2.16}$$

Where, u = the mean point velocity in the longitudinal direction (L/T);

u_* = the shear velocity. (LT^{-1});

κ = von Karman coefficient;

y = the distance normal to the plane of the channel bottom (L);

k_s = the grain roughness. (Dimensionless); and

B = the intercept of the Equation 2.16.

2.3.2.2 Schlicting (1987)

Schlicting (1987) suggested a bed shear stress calculation method by applying a linear regression between the logarithmic profile of flow depth and flow velocity. The shear stress calculation method is explained in Equation 2.17 through Equation 2.19.

$$V = \frac{u_*}{\kappa} \ln\left(\frac{z}{z_o}\right)$$ **Equation 2.17**

$$V = \frac{u_*}{\kappa} \ln z + \mathbf{C}$$ **Equation 2.18**

Where, C is the constant: $-\frac{u_*}{\kappa} \ln(z_o)$ **Equation 2.19**

$\frac{u_*}{\kappa}$ is the slope of linear regression equation.

As a result, the shear stress can be computed by Equation 2.20;

$$\tau = \rho \times (\kappa \times S)^2$$ **Equation 2.20**

Where, S = the slope of the Equation 2.19;

κ = von Karman coefficient. It was assumed that the value of 0.4; and

z = the vertical distance the bottom of the channel (L).

2.3.2.3 Smart (1999)

Smart (1999) published a theory of turbulent velocity profiles and boundary shear by analyzing field data. Smart (1999) collected velocity data at six rivers in New Zealand by using an ADV (Acoustic Doppler Velocity) meter. Three rivers have medium flow condition; Waiho, North Ashburton, and Rangitata rivers. The other three rivers have floods condition; Waitaki, Hurunui, and Rangitata rivers. Smart (1999) obtained the flow resistance equation presented in Equation 2.21

$$\frac{\bar{U}}{U^*} = 2.5 \times \left[\ln\left(M \frac{gH}{U^{*2}} \right) - 1 \right] \qquad \textbf{Equation 2.21}$$

To determine the M value in Equation 2.21, the relationship between shear velocity head and hydraulic roughness was plotted in Figure 2.21.

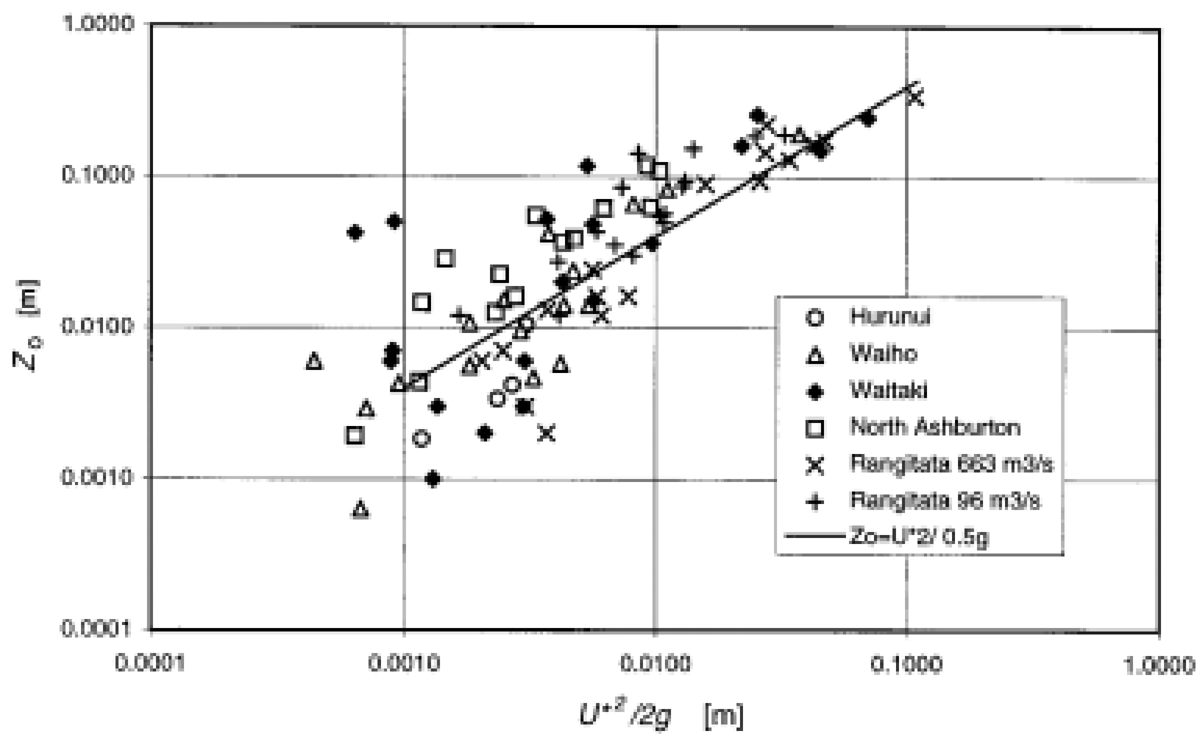

Figure 2.21 Relationship between Log Profile Parameters and Shear Velocity Head (from Smart 1999))

Where, $\bar{U}$ = the vertical averaged streamwise velocity (LT^{-1});

U^* = the velocity scaling parameter for log law, identical with u_* for uniform 2D flow. (LT^{-1}); and

M = the coefficient that relates shear velocity head to hydraulic roughness. (Dimensionless)

Smart (1999) concluded that the collected field data indicate that the grain roughness is proportional to the log profile parameter, U^* under the condition of mobile bed channels. In addition, Smart (1999) claimed that bed shear stress, τ_o is linearly proportional to the grain roughness in case of uniform flow conditions.

2.3.3 Rozovskii's Method (1961)

The method presented by Rozovskii is for the radial shear stress computation by using equations that were derived from Cartesian coordinates. Rozovskii published a paper titled 'Flow of Water in Bends of Open Channels' in 1957 which was translated into English in 1961 at Academy of Science of the Ukrainian SSR Institute of Hydrology and Hydraulic Engineering. Rozovskii introduced the equations for analyzing the flow characteristics in a meandering channel. In addition, Rozovskii (1961) provided a comparison and discussion of other researchers' studies since the introduction of the radial shear stress calculation method in meandering channel. Rozovskii's radial shear stress equation in meandering channel is provided in Equation 2.22;

$$\tau_r = [\rho g S_r h] - \left[\rho \times \int_0^h \frac{v_\theta^2}{R} dz\right] \qquad \textbf{Equation 2.22}$$

Where, τ_r = the radial shear stress ($ML^{-1}T^{-2}$);

ρ = the mass density of the fluid (ML^{-3});

g = the acceleration of gravity (LT^{-2});

Sr = the water surface elevation (L/L);

h = the flow depth (L);

v_θ = the flow velocity along the bend of the channel (LT^{-1}); and

r = the radius of curvature of the channel bend (L).

Before Rozovskii (1961) suggested the method for radial shear stress computation, several researchers conducted laboratory tests to figure out the flow characteristics in meandering channels. Table 2.3 presents the summary of the laboratory tests.

Table 2.3 Summary of Experiment Results of Flow in Bend (from Rozovskii, 1961)

Author	Year of Experiments	Rotation Angle (Degrees)	Channel Width (cm)	Radius of Curvature (cm)	Flow Depth (cm)	Mean Flow Velocity (cm/sec)	h/b	h/r	Channel Form	Subject Of Measurement
Milovich	1914	180	24	28	0.45-13.8	0.66-5	-	-	Rectangular	Trajectories of Bottom Particles with the aid of coloring Material
Daneliya	1936	180	40	60	12	18	0.3	0.2	Rectangular	Distribution of longitudinal and transverse velocity components
Kozhevnikov	1940-1941	180	80	160	2-10	22-50	0.025-0.125	0.0125-0.067	Rectangular Triangular Parabolic	Trajectories of Bottom and surface floats, topography of free surface
Mockmore	1943	2×180	45	52.5	9-12	15-25	0.2-0.27	0.17-0.23	Rectangular	Longitudinal Velocity components topography of free surface
Shuckry	1949-1950	45-180	30	15-90	18-36	90-78	0.6-1.2	0.4-1.2	Rectangular	Distribution of Velocities, topography of free surface
A.I Fidman	1949	3×117	100	225	11.5-16	8.7-3.6	0.12-0.16	0.051-0.071	Rectangular	Topography of free surface
M.I Terasvatsatyan	1950	180	38.4	58	-15	30-40	0.39	0.26	Rectangular	Distribution of Velocities, with aid of ball nozzle
Same	1950	67	38.4	209	-11	-	0.29	0.048	Rectangular	Distribution of Velocities, with aid of ball nozzle
A.K Ananyan	1953	2×180	50	250	15-18	26-33	0.3-0.36	0.06-0.72	Rectangular	Distribution of Velocities, with aid of ball nozzle
N.I Makkareev B.E Romanenko	1940	180	25	50	3-12	20-72	0.1-0.5	-	Rectangular of sinusoidal configuration in plane	Velocity Distributions

2.3.3.1 Laboratory Study for Validation of Theory

For the validation of the theory of Rozovskii, a physical model was constructed by the Hydraulic Laboratory of the Institute of Hydrology at the USSR Academy of Sciences. The rotation angle was 90 degrees, radius of curvature was 16.4 ft, the maximum flow depth was 0.459 ft and bed slope was 0.001 ft/ft. A hydrometric tube was used for the velocity measurement. To obtain the velocity profile, flow velocity measurements were carried out. The depth increment was 0.0656 ft. In the case of the bend section that starts at cross section 14, a nozzle ball was used for the velocity measurement. Figure 2.22 shows the test results for flow velocity distribution.

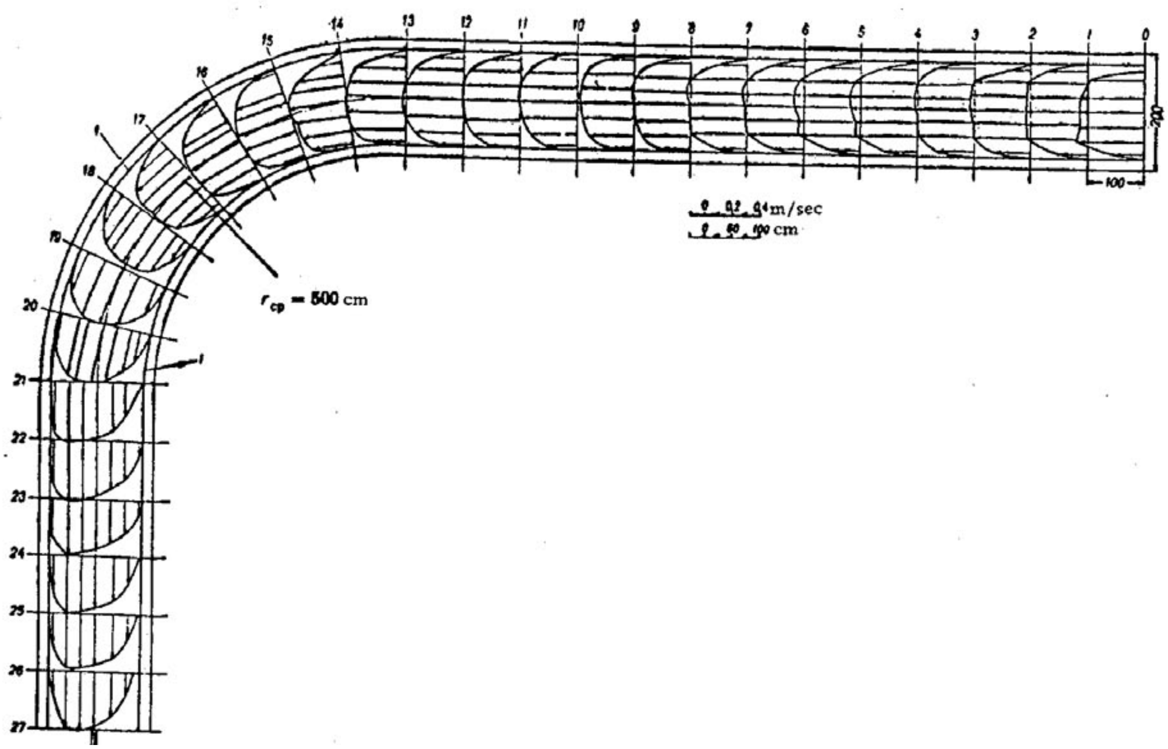

Figure 2.22 Velocity Distribution from the Test result by the Experiment of Polygonal Section (from Rozovskii, 1961)

2.3.3.2 Field Observation for Validation of Theory

Field observations were also performed by the Hydraulic Laboratory of the Institute of Hydrology USSR Academy of Sciences in 1951~1952. The locations of the field observation were the Snov River and Desna River. The rotation angle of the study reach of Desna River is 180 ° and radius of curvature is 400 m. Figure 2.23 shows the study reach of the river. During the field observation, field surveying was performed to determine the water surface elevation and flow depth. According to the surveying results, the general cross section is rectangular. The flow depth was especially deep at cross section 4 the location of contraction of the channel width to 110 m. For measuring the flow velocity, a rotary flow meter with an elongated vane was used.

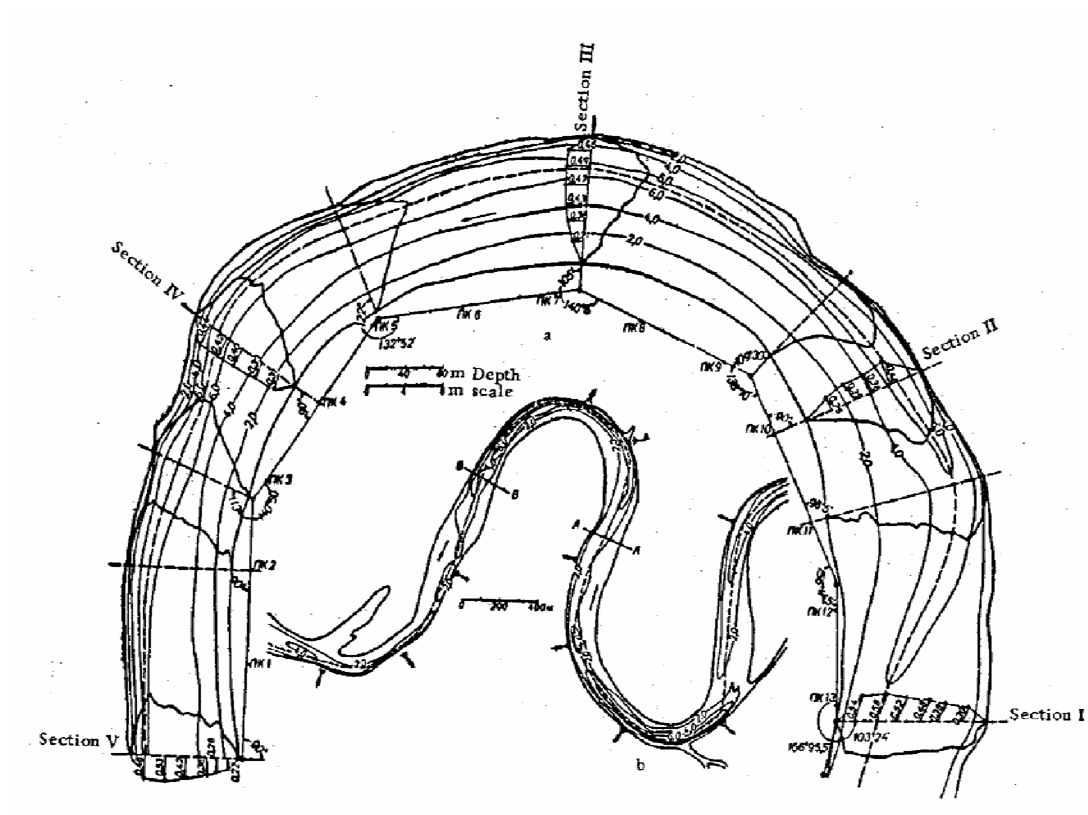

Figure 2.23 Description of Study Reach, Desna River (from Rozovskii, 1961)

Another field observation was performed at the Snov River by Hydraulic Laboratory of the Institute of Hydrology USSR Academy of Sciences. The geometry of the Snov River explained below. Figure 2.18 also shows the plan view and velocity distribution of the Snov River.

1) The averaged channel width was 82.02 ft.
2) The radius of curvature was 279 ft.
3) Maximum flow velocity was 2.624 ft/sec.
4) Discharge of Snov River was about 2119 ft^3/sec.
5) Bed Slope was 0.000382 ft/ft.

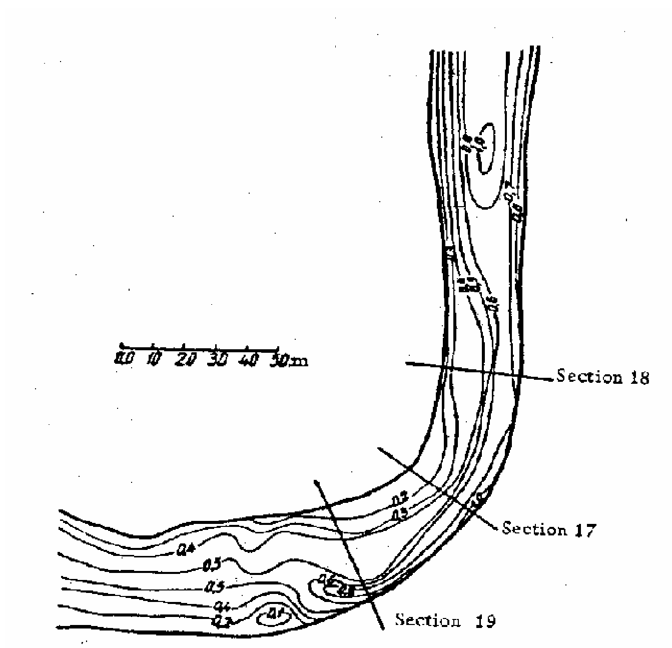

Figure 2.24 Plan View of Snov River (from Rozovskii, 1961)

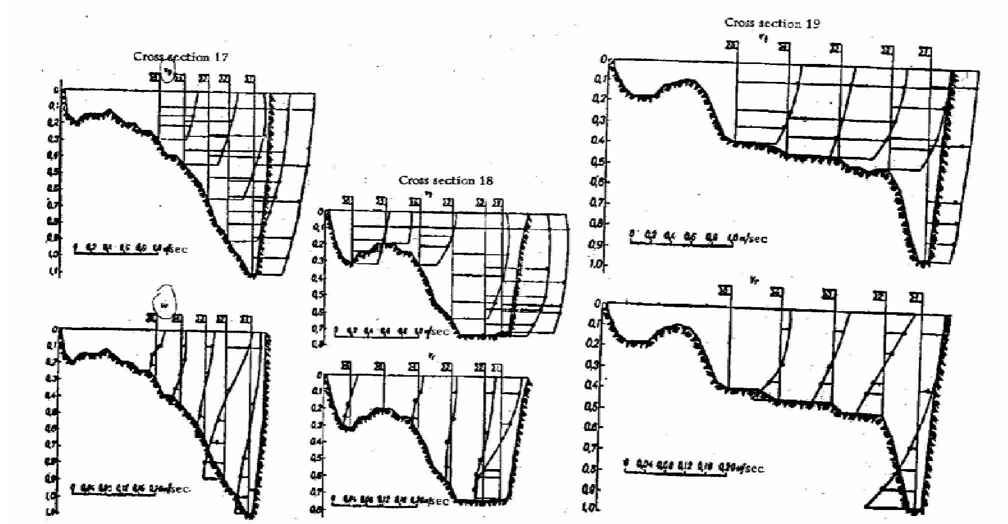

Figure 2.25 Distribution of Flow Velocity of Snov River (from Rozovskii, 1961)

According to the results of the laboratory study and field observations, Rozovskii (1961) concluded that there was good agreement between field observation and the desired theoretical equation. Following Rozovskii's research, several people such as Odgaard (1986) conducted mathematical modeling to determine flow characteristics for a meandering channel.

2.3.4 Reynolds Shear Stress

Julien (1998) explained the Cartesian element of fluid composed with two different forces; internal and external forces. Internal forces apply at the center of the mass (Julien 1998). In case of external forces, stress can be classified as two other components; normal and tangential stress. The study focuses on the calculation of the tangential stress that corresponds with Reynolds shear stress comprised of six different components; $\tau_{xy} = \tau_{yx}$, $\tau_{xz} = \tau_{zx}$ and $\tau_{yz} = \tau_{zy}$. A schematic sketch of surface stresses is presented in Figure 2.26.

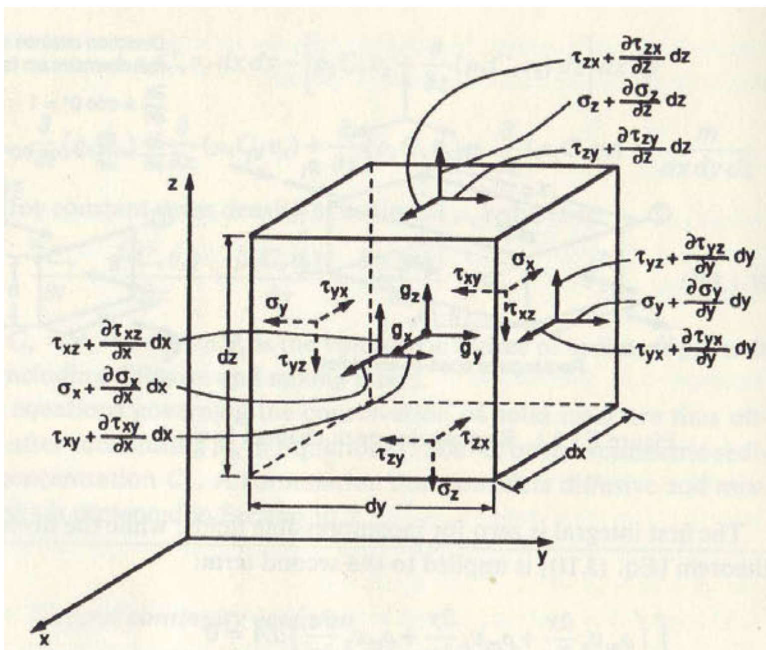

Figure 2.26 Schematic Sketch of Surface Stresses (from Julien 1998)

2.3.4.1 Wahl (2000)

To calculate six components of Reynolds shear stress, an ADV (Acoustic Doppler Velocity) meter was used in this study. The representative flow data from ADV are COV (Covariance) because they are directly used to obtain Reynolds shear stress. As shown in Figure 2.27, flow velocity is not always identical with the averaged flow velocity due to the turbulence in the flow. The basic concept of covariance in this study is the correlation of two components of flow velocity out of three flow velocity components; V_x, V_y and V_z.

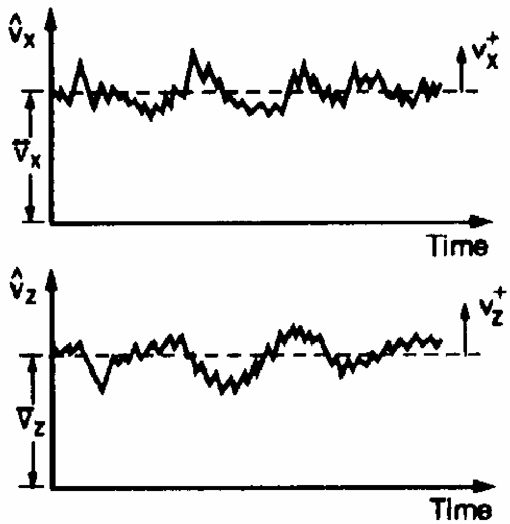

Figure 2.27 The Description of Turbulence in Flow (from Julien 1998)

Equation 2.23 through Equation 2.28 that was cited from Wahl (1996) show the calculation method of Reynolds shear stress using ADV data.

$$\tau_{xy} = \tau_{yx} = -\rho \times (COV - XY) \qquad \textbf{Equation 2.23}$$

Where, τ_{xy} = the turbulent shear stress that applies along the y axis and caused by flow velocity fluctuation in the direction of x-axis (ML-1T-2).

ρ = the mass density of water (ML^{-3}).

COV-XY is the covariance of two variables (V_x and V_y). It can be computed by using Equation 2.24.

COV-XY = $\frac{\sum V_x V_y}{n-1} - \frac{\sum V_x \sum V_y}{n(n-1)}$ **Equation 2.24**

Where, V_x = the flow velocity along x-axis (LT^{-1});

V_y = the flow velocity along y-axis (LT^{-1});

n = the number of samples that collected velocity data (Dimensionless).

τ_{zx} is the turbulent shear stress that applies along the x axis and caused by flow velocity fluctuation in the direction of z-axis ($ML^{-1}T^{-2}$).

$$\tau_{zx} = \tau_{xz} = -\rho \times (COV - XZ)$$ **Equation 2.25**

Where, ρ = the mass density of water (ML^{-3}).

COV-XZ is the covariance of two variables (V_x and V_z). Covariance of two variables (V_x and V_z) is computed by Equation 2.26.

COV-ZX = $\frac{\sum V_z V_x}{n-1} - \frac{\sum V_z \sum V_x}{n(n-1)}$ **Equation 2.26**

Where, V_x = the flow velocity along x-axis (LT^{-1}).

V_z = the flow velocity along z-axis (LT^{-1}).

n= the number of samples that collected velocity data (Dimensionless).

τ_{zy} is the turbulent shear stress that applies along the y axis and caused by flow velocity fluctuation in the direction of z-axis ($ML^{-1}T^{-2}$).

$$\tau_{yz} = \tau_{zy} = -\rho \times (COV - YZ)$$ **Equation 2.27**

Where, ρ = the mass density of water (ML^{-3}).

COV-YZ is the covariance of two variables (V_z and V_y). It can be obtained using Equation 2.28.

$$\textbf{COV-YZ} = \frac{\sum V_y V_z}{n-1} - \frac{\sum V_y \sum V_z}{n(n-1)} \qquad \textbf{Equation 2.28}$$

Where, V_y = the flow velocity along y-axis (LT^{-1}).

V_z = the flow velocity along z-axis (LT^{-1}).

n = the number of samples that collected velocity data (Dimensionless).

2.3.4.2 Baird (2004)

Baird (2004) suggested linear extrapolation of Reynolds shear stress profile to obtain bed shear stress using ADV data. An example of Reynolds shear stress profile is presented in Figure 2.17. Due to the existence of roughness sublayer, Reynolds shear stress decreases to the near bed area just after a maximum value of Reynolds shear stress (Raupach (1991); Nikora and Gohring (2000)). As a result, Montes (1998) suggested linear extrapolation of the linear portion of Reynolds shear stress profile as a method of bed shear stress calculation. Actually, Baird (2004) stated "Reynolds shear stress can be calculated by extrapolating the slope of the linear portion of the shear stress profile to the bed". In addition, Montes (1998) explained that finding the point of interception with x axis is zero in Figure 2.28 is a good method of estimation of bed shear stress.

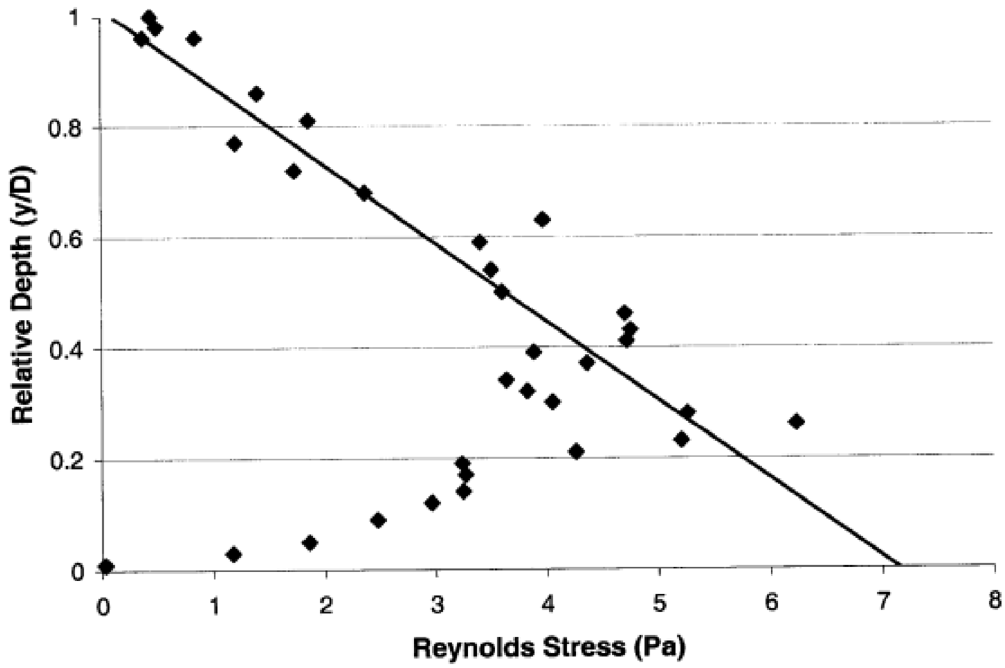

Figure 2.28 Reynolds Shear stress Profile (from Baird (2004))

Baird (2004) rearranged Equation 2.29 (cited from Muste and Patel, 1997; Montes,1998) into Equation 2.30 to obtain the linear regression equation from the linear portion of the Reynolds Shear stress profile that was presented in Figure 2.28.

$$\frac{\tau}{\rho} = -\overline{u^{'}v^{'}} = u_*^2\left(1-\frac{y}{D}\right) \qquad \textbf{Equation 2.29}$$

Where, τ = the shear stress ($ML^{-1}T^{-2}$);

ρ = the mass density of water (ML^{-3});

$u^{'}$ = the instantaneous velocity fluctuations about the mean in the longitudinal direction (LT^{-1}); and

$v^{'}$ = the instantaneous velocity fluctuations about the mean in the vertical direction (LT^{-1}).

$$\frac{y}{D} = m \times (\tau) + b \qquad \textbf{Equation 2.30}$$

Where, $\frac{y}{D}$ = relative depth (Dimensionless);

τ = the shear stress that equals to $-\overline{u'v'}$ at depth $\frac{y}{D}$ ($ML^{-1}T^{-2}$);

m = the regression slope of linear regression equation; and

b = the intercept of the regression line.

2.4 Summary

Numerous researchers have performed studies to quantify shear stress distribution in meandering channels. Mathematical modeling and laboratory experiments have been implemented for the validation of theories. To understand the mechanism of shear stress distribution in meandering channels, the understanding of background of flow in a bend is necessary. At the beginning of this chapter, the basic mechanism of flow in meandering channels was introduced; the parameters to determine meandering channel geometry, stream morphology, concept of secondary flow in bend, the effect of superelevation, and Lane's balance to explain the dynamic equilibrium in a stream system. In Section 2.3.1 through Section 2.3.4, the methods of shear stress calculation were introduced for data analysis of the study. The calculation methods are; Preston tube, linear regression of velocity profile, Rozovskii's method and extrapolation of Reynolds shear stress by using ADV data.

3 Data Analysis

3.1 Introduction

Data analysis was conducted to determine the distribution of shear stress. Measurements of flow velocity, flow depth, and boundary shear stress were performed during the data collection procedure. In accordance with the procedure presented in Section 2.3, four methods were used for the data analysis: a) Preston tube, b) Logarithmic Velocity Profile, c) Rozovskii method, and d) Reynolds shear stress. In this chapter, the shear stress calculation results and the value of differences between each shear stress calculation method are presented.

3.2 Shear Stress Calculation Results

Four calculation methods were used for data analysis. Entering and exiting flow in the model will result in overestimation of shear stress. As result, shear stress data of cross sections 1 through 3 and cross section 18 were excluded from analysis. Preston tube method is the shear stress calculation using a pitot tube. Logarithmic Velocity Profile is the technique of shear stress calculation by obtaining a linear regression after plotting the relationship between flow depth and logarithmic flow velocity profile. Rozovskii's method was derived from the equation of motion in Cartesian coordinates. Reynolds shear stress is calculated from ADV data based on the covariance of two variables of flow velocity. The two variables originated from two of three flow velocity components: V_x, V_y and V_z. In this section, the results and discussion of the data analysis for the four different shear stress calculation methods are presented.

3.2.1 Preston Tube

Preston tube calibration was conducted by Sclafani (2008) in a flume. Boundary shear stress in the x direction, τ_x, was computed by converting Preston differential pressure data (inch of head) into shear stress (psf) using the Preston tube calibration that was exhibited as Equation 2.13. The shear stress distribution calculations from the Preston tube method are presented in Figure 3.1 through Figure 3.4. The range of τ_x values by Preston tube were between 0.0075 psf and 0.072 psf. Clearly, the area with a higher value of τ_x was located at the inner side of the downstream bend of the channel. Also, proportionality of the τ_x value with increasing flow rate was observed except for the case of 16 cfs. With the increases of constant rate, the measured data consistently moved into a higher level of τ_x values.

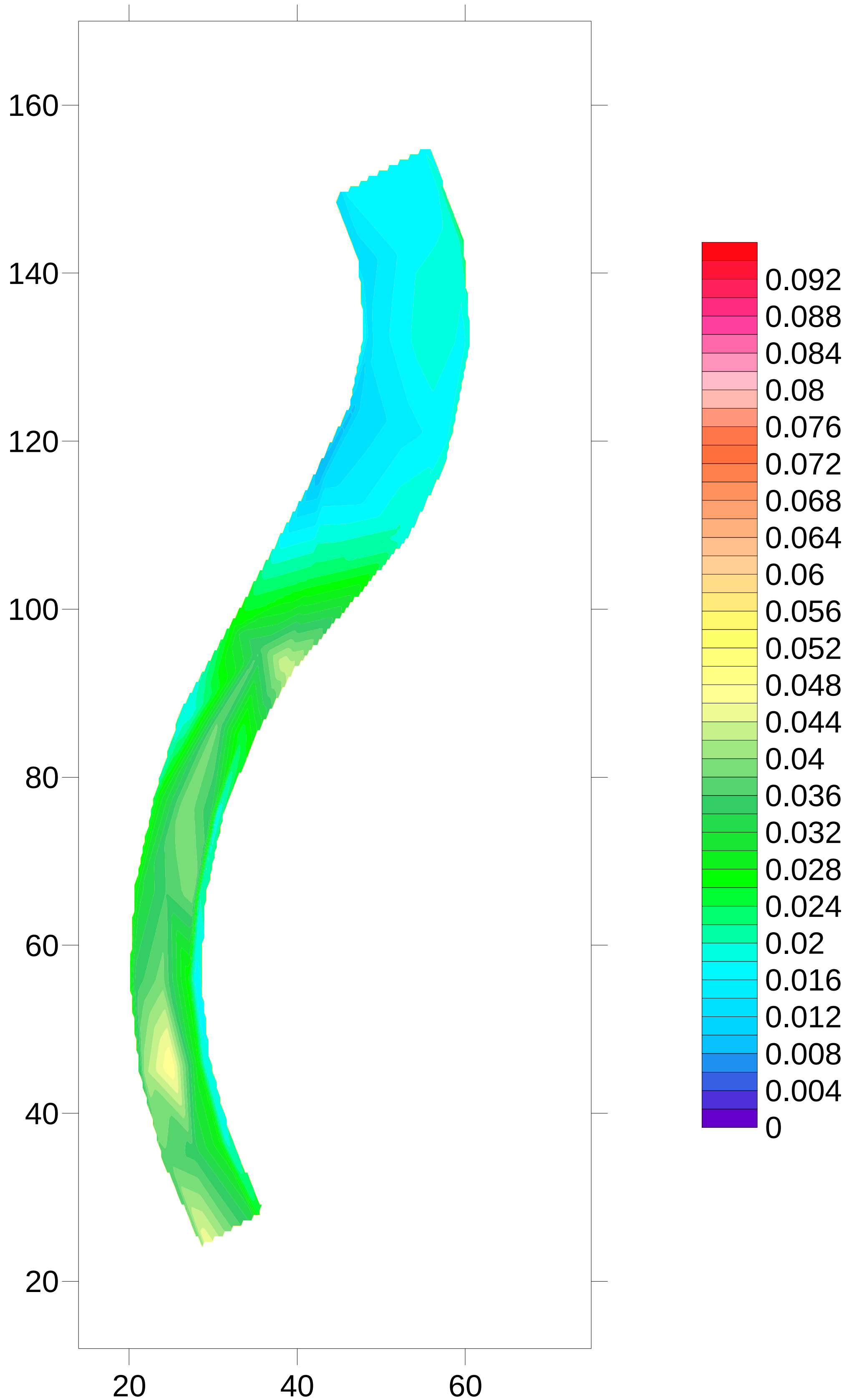

Figure 3.1 Shear Stress Distribution, τ_x, from Preston Tube for 8 cfs (psf)

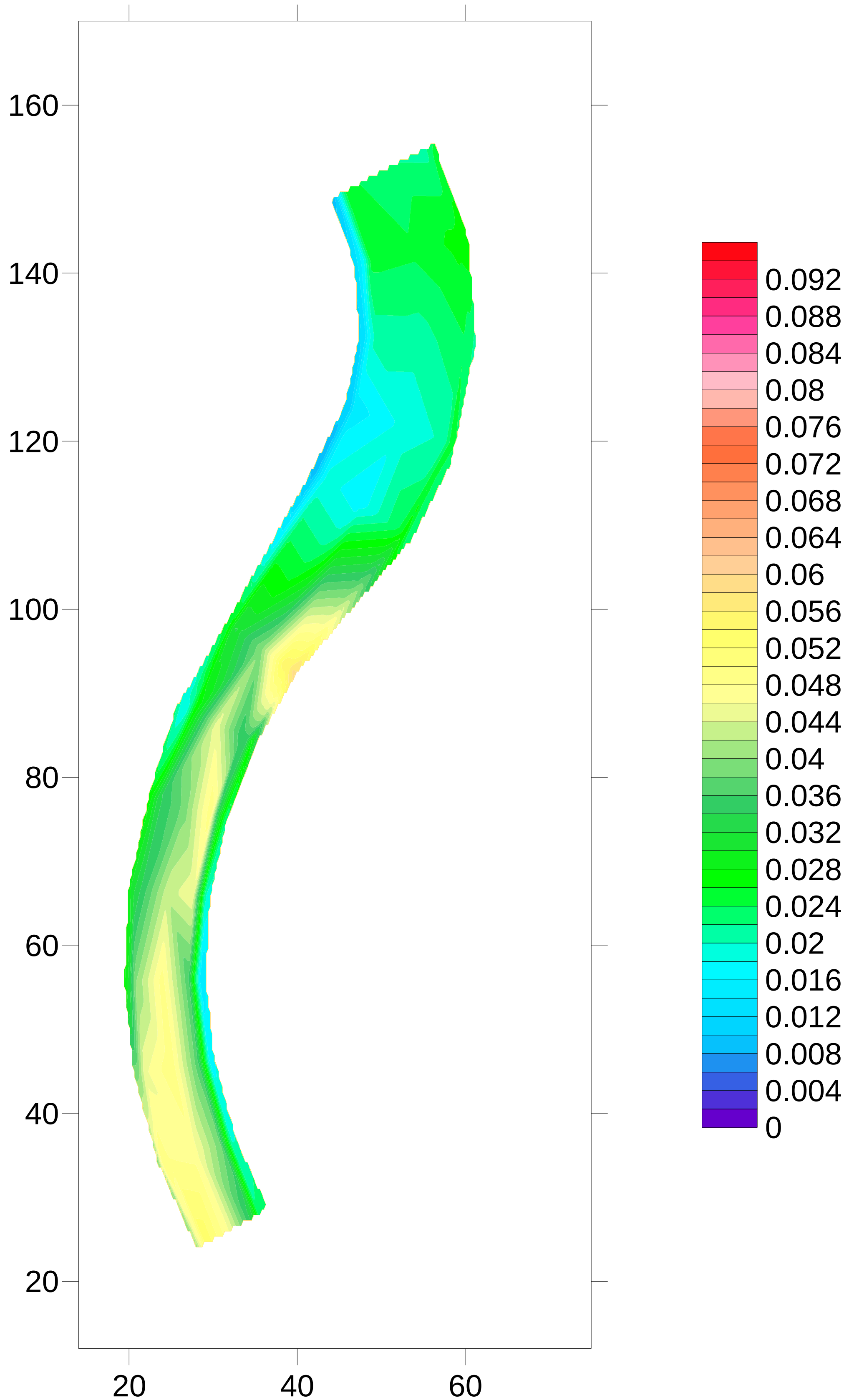

Figure 3.2 Shear Stress Distribution, τ_x, from Preston Tube for 12 cfs (psf)

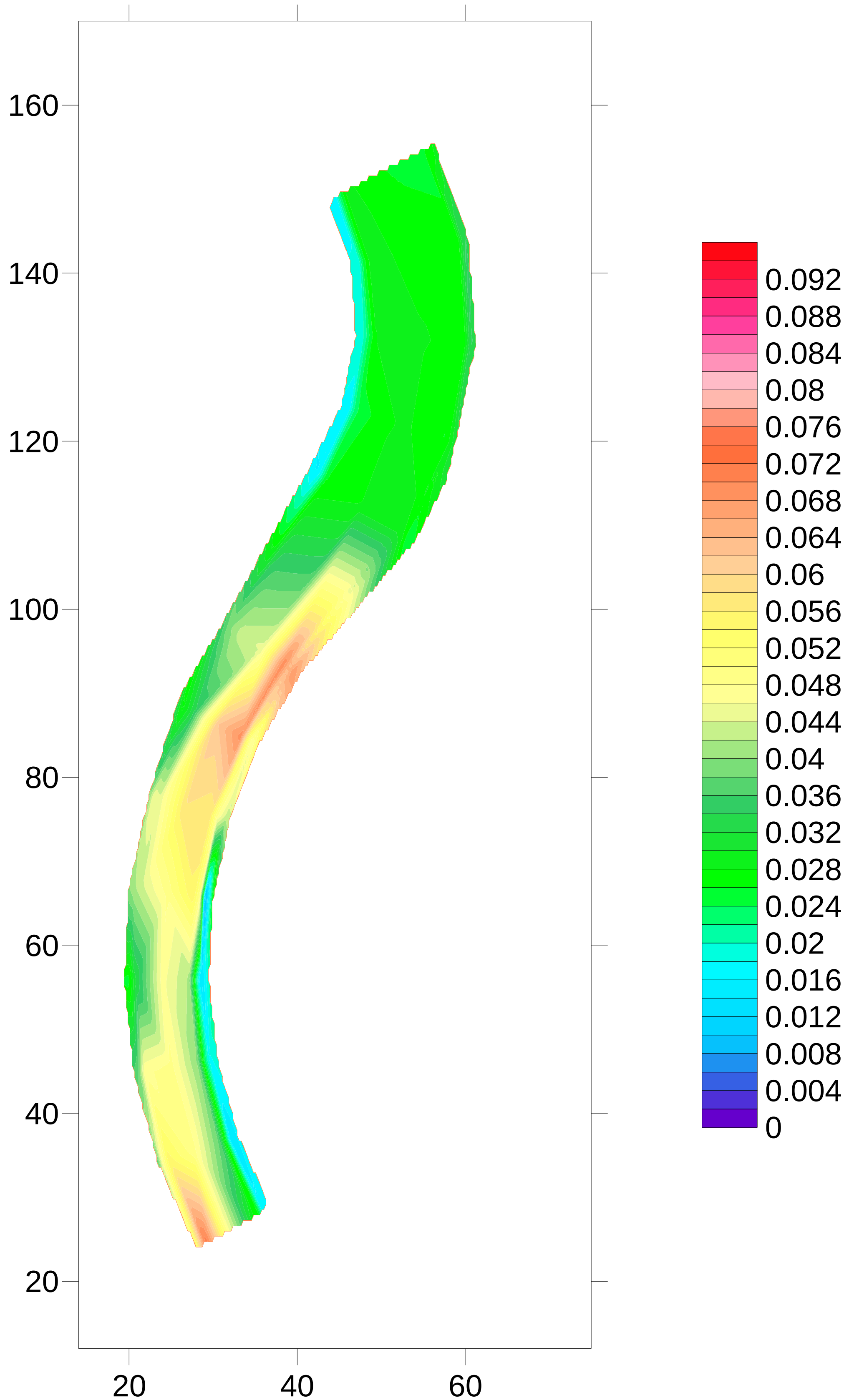

Figure 3.3 Shear Stress Distribution, τ_x, from Preston Tube for 16 cfs (psf)

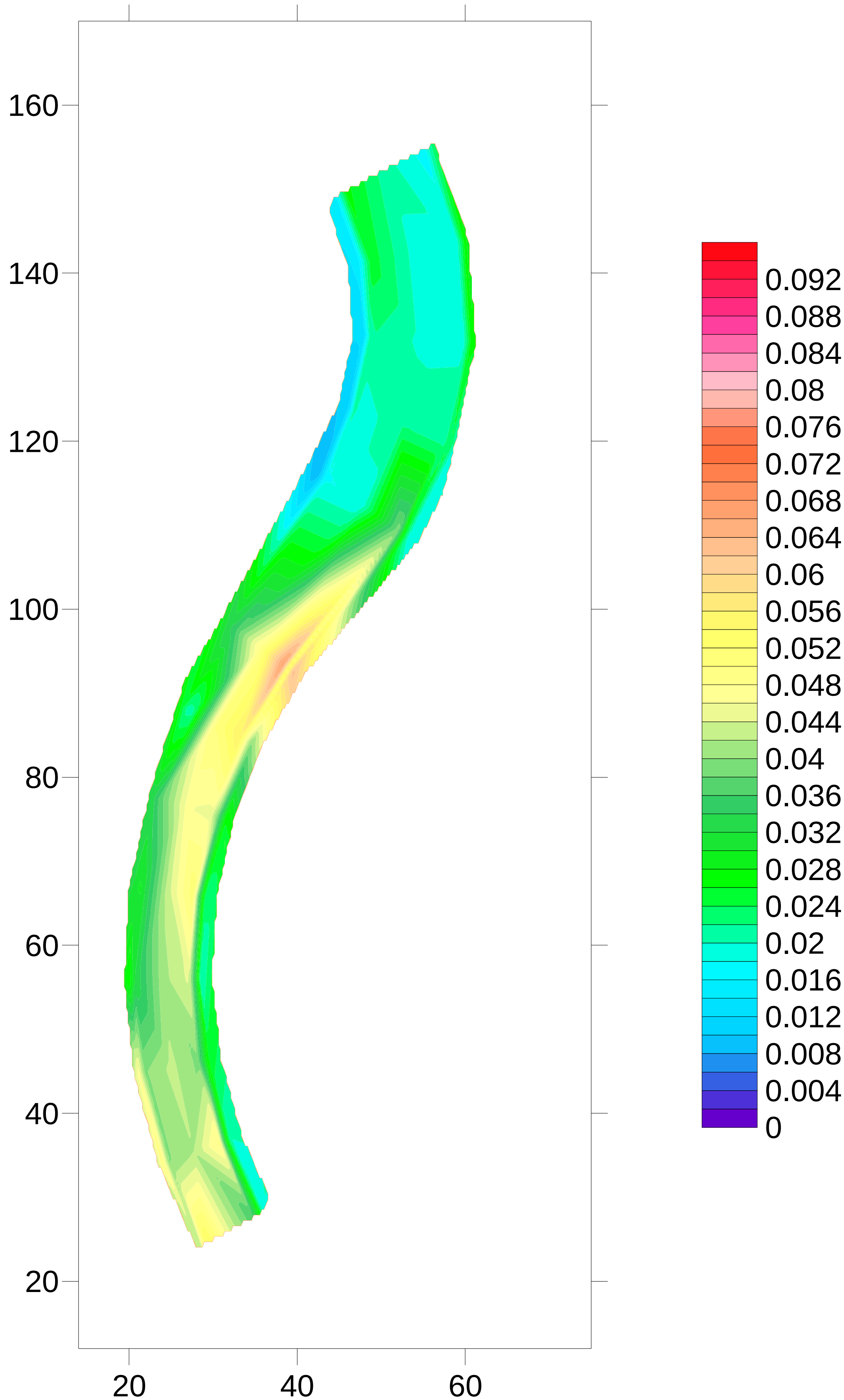

Figure 3.4 Shear Stress Distribution, τ_x, from Preston Tube for 20 cfs (psf)

3.2.2 Linear Regression of Flow Velocity Profile

Equation 2.17 through Equation 2.20 describes the method of linear regression of flow velocity profile. Ideally, the τ_x value that was obtained from this method is identical with the value of τ_x by Preston tube. Figure 3.5 presents the distribution of turbulent shear stress, τ_x for 20 cfs. The value of τ_x ranged between 0 psf and 0.076 psf. Just as in the case of τ_x by Preston tube, a higher value of τ_x was observed at the inside of the downstream bend of the channel. Proportionality of flow rate and shear stress also was observed. In addition, lateral shear stress, τ_y was calculated using same method to obtain τ_x. The result is presented in Figure 3.6. The shear stress distribution for 8, 12 and 16 cfs is presented in Appendix C.

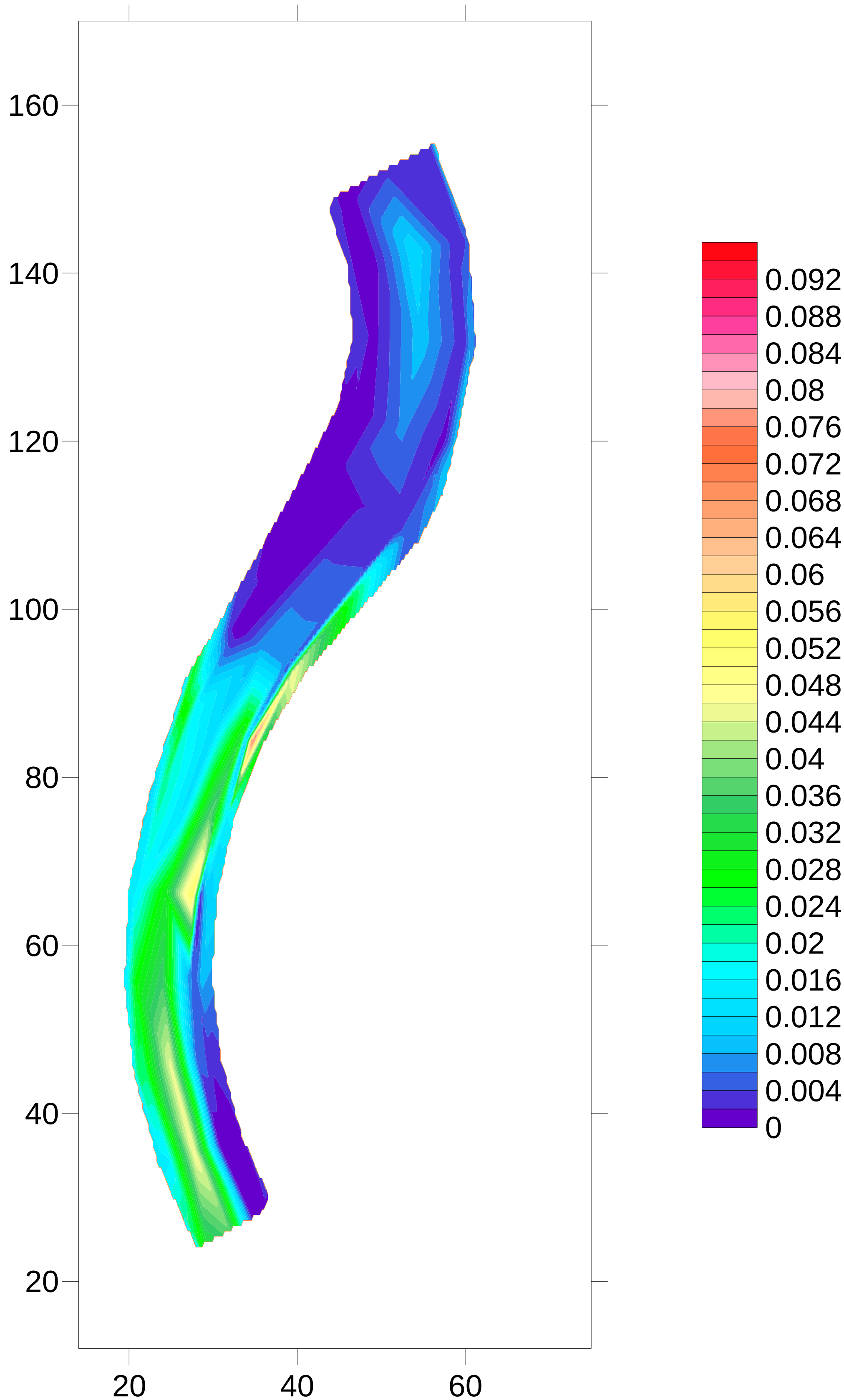

Figure 3.5 Shear Stress Distribution, τ_x, by Linear Regression for 20 cfs (psf)

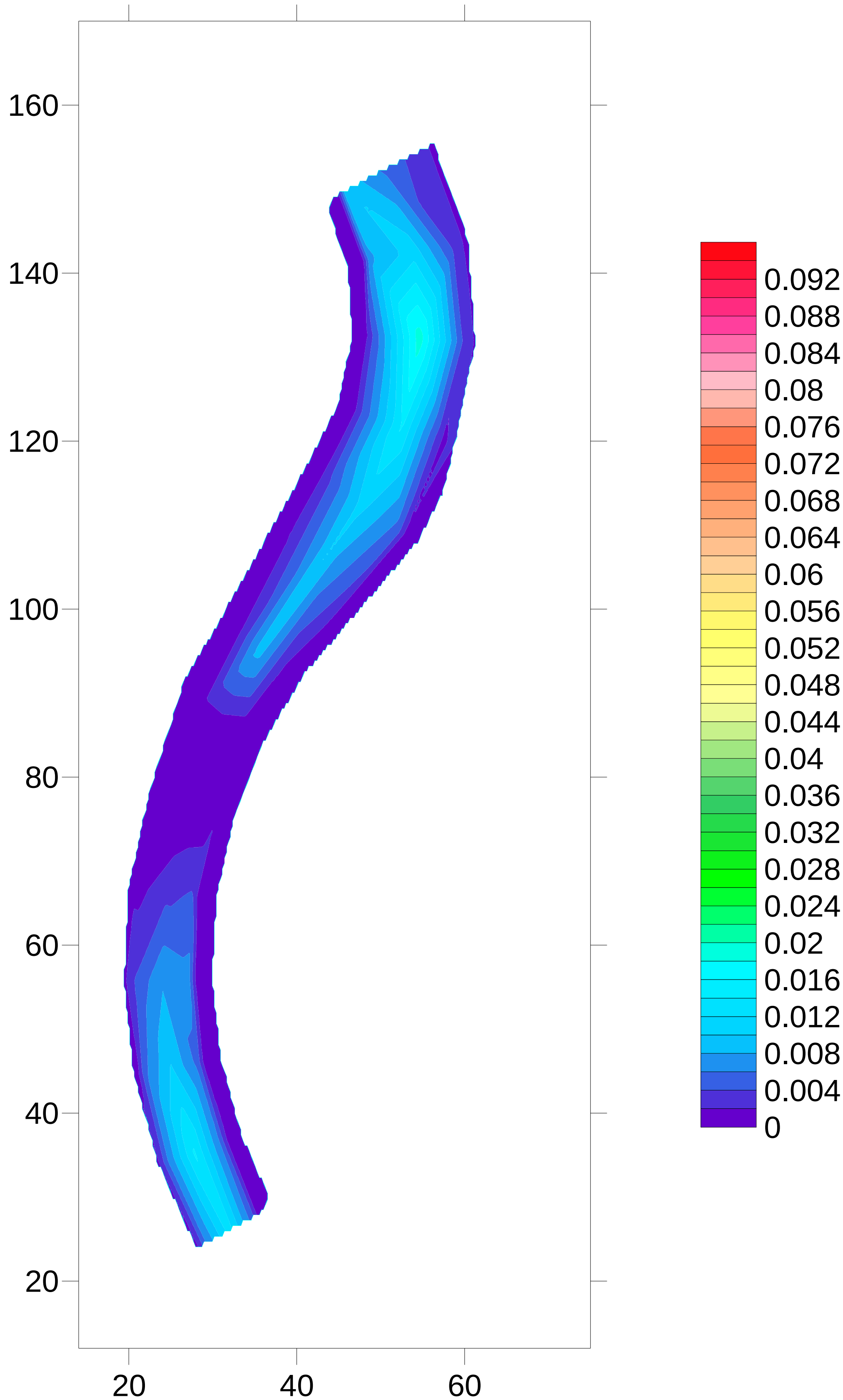

Figure 3.6 Shear Stress Distribution, τ_y, by Linear Regression for 20 cfs (psf)

3.2.3 Rozovskii Method

The shear stress calculation method presented by Rozovskii (1961) computes the radial shear stress in a meandering channel, τ_r by using Equation 2.22. A detailed calculation procedure for the water surface slope, S_r, and the second bracket in the right hand side of Equation 2.22 is presented in this section. The water surface slope can be expressed by Equation 3.1:

$$S_r = \frac{h}{D} \qquad \textbf{Equation 3.1}$$

Where, Sr = water surface slope (L/L);

h = difference of water surface elevation between piezo a and g (L);

D = horizontal distance of piezo between piezo a and piezo g (L).

Equation 4.2 shows the detailed calculation method for the distance between piezometer a and piezometer g. The multiplying factor of 3 comes from the 3:1 (Horizontal: Vertical) side slope of the trapezoidal channel. Equation 3.2 is presented below;

$$D = d_1 + d_2 + d_3 \qquad \textbf{Equation 3.2}$$

Where, D =Horizontal distance between Piezo a and Piezo g (L);

d_1 = 3 times of the difference of height of Piezo a and d (L);

d_2 = Channel bottom width (L); and d_3 is 3 times of the difference of height of Piezo g and d (L).

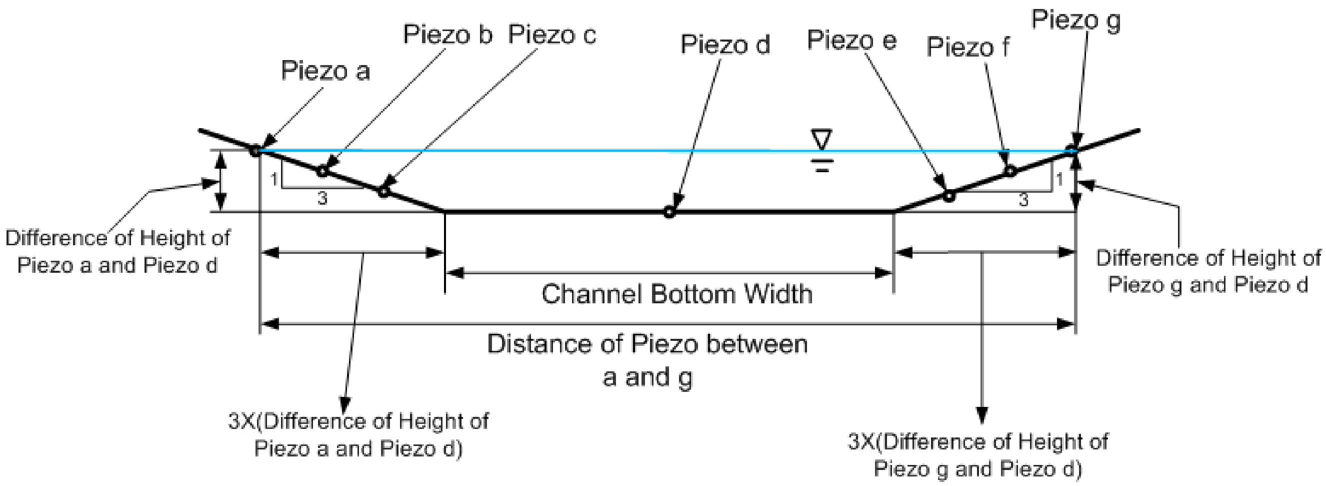

Figure 3.7 Schematic Sketch of Distance between Piezo a and Piezo g

For the calculation of the second bracket in the right-hand-side of Equation 2.22, a manual integration method was used. Figure 3.8 illustrates the idealized flow velocity profile. The term $\int_0^H \frac{v_\theta^2}{r} dz$ can be described by Equation 3.3;

$$\frac{1}{r}\left\{\left(\frac{v_1+v_o}{2}\right)^2(z_1-z_{Bed})+...+\left(\frac{v_n+v_{n+1}}{2}\right)^2\times(z_{n+1}-z_n)+v_n^2\times(z_{WSE}-z_n)\right\} \quad \textbf{Equation 3.3}$$

Where, v_1 = flow velocity value that locates in the lowest data collection point (L/T);

v_2 = flow velocity value that locates just above of the location of v_1 (L/T);

v_n = flow velocity value that locates in the highest point (L/T);

z_{Bed} = bed elevation of the Channel; and ΔZ is differential flow depth (L).

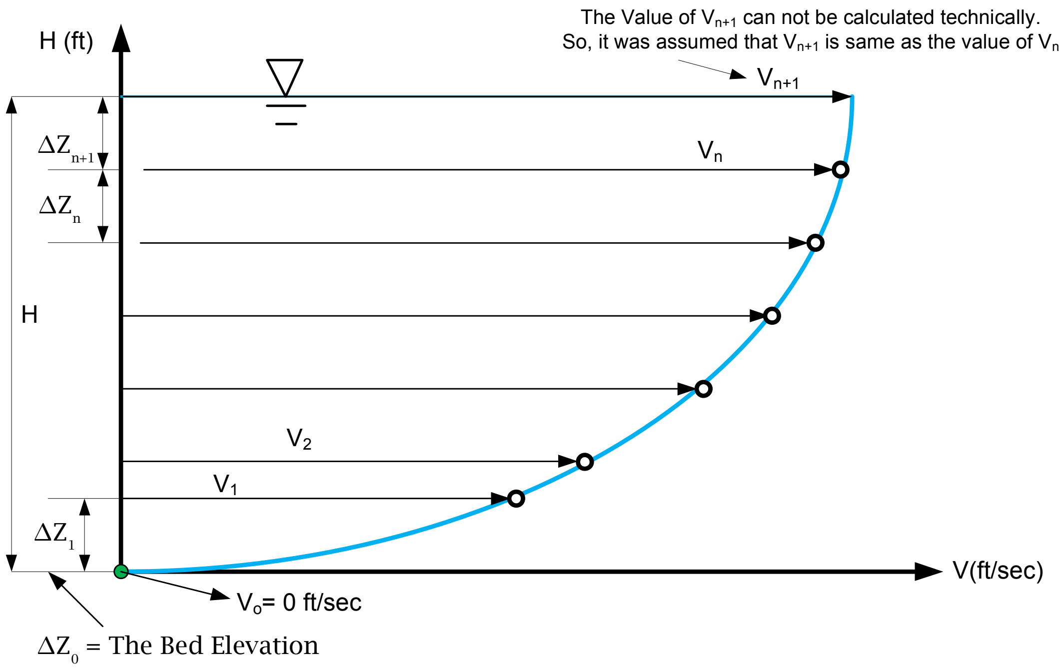

Figure 3.8 Idealized Flow Velocity Profile

The shear stress distribution from the Rozovskii method is presented in Figure 3.9 for 20 cfs. The range of the values of τ_r were between -0.048 psf and 0.13 psf. Differently from the method of Preston tube and linear regression of flow velocity profile, shear stress by Rozovskii method did not show proportionality with increase of the flow rate. Also, negative shear stress values were observed: the point of negative shear stress has a less steep water surface slope. That means the S_r value is the dominant parameter of shear stress from the Rozovskii method. To validate the observation, the water surface slope distribution for each flow rate is presented in Figure 3.10 for 20 cfs. The plots show good agreement between the change of water surface slope and shear stress distribution from Rozovskii.

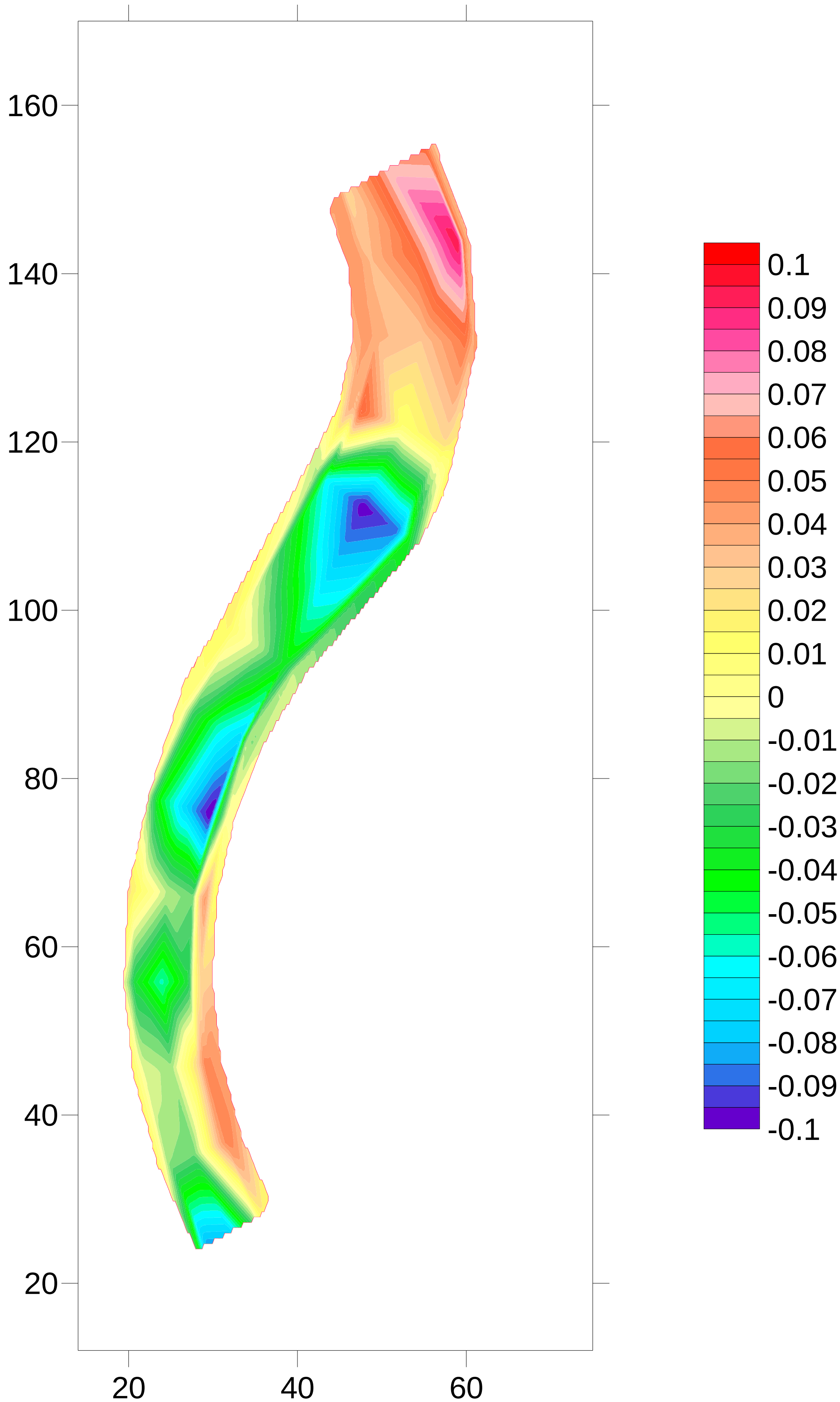

Figure 3.9 Radial Shear Stress Distribution, τ_r, from Rozovskii (1961) for 20 cfs (psf)

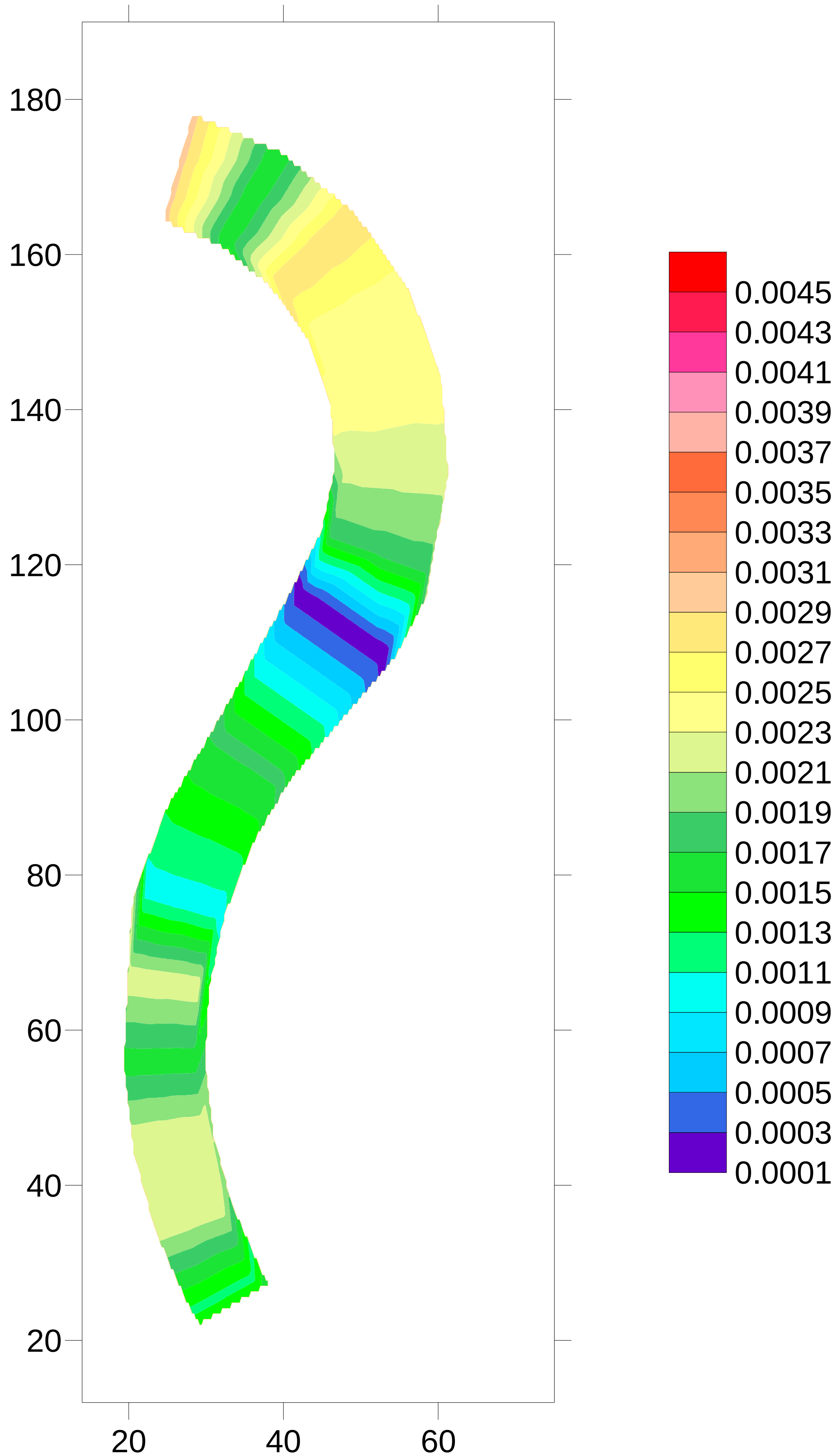

Figure 3.10 Water Surface Slope Distribution for 20 cfs

3.2.4 Reynolds Shear Stress

Reynolds shear stress is based on the ADV (Acoustic Doppler Velocity meter) data of each piezometer and each cross section of the model. As suggested by Montes (1998), Reynolds shear stress profile was plotted to take a linear regression of the linear portion of the Reynolds shear stress profile. The x axis of the linear regression equation is Reynolds shear stress and y axis is the relative depth. The non-linear portion of the Reynolds shear stress profile that was shown as pink dots in Figure 3.11 and Figure 3.12 was taken out for the linear regression. In addition, Wahl (2002) explained that when a data point of correlation is below 70 and the signal to noise ratio is below 15 has a high possibility of low accuracy. As a result, ADV data point covariance below 70 and signal to noise ratio below 15 were excluded from the plotting of the Reynolds shear stress profile. Montes (1998) explained the point where the linear regression equation intercepts the x axis is the bed shear stress. τ_{bed}, shear stress in the longitudinal direction that applies on the bed of the channel can be computed from Equation 3.4. Summaries of the calculation result from Reynolds shear stress extrapolation are presented in Appendix E.

$$\tau_{bed} = \sqrt{(\tau_{xz})^2 + (\tau_{zy})^2} \qquad \textbf{Equation 3.4}$$

Where, τ_{bed} = the turbulent shear stress in longitudinal direction that applies on the bed of the channel (M/L^{1}T^2);

τ_{zx} = the turbulent shear stress that applies in x axis caused by V_z (M/L^{1}T^2); and

τ_{zy} = the turbulent shear stress that applies in y axis and caused by V_z (M/L^{1}T^2).

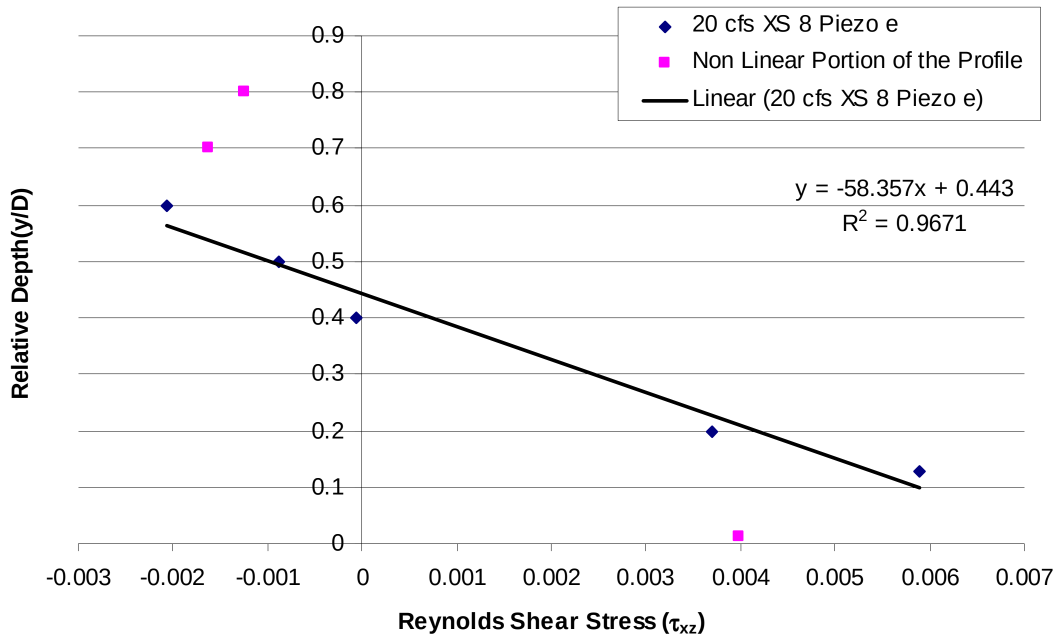

Figure 3.11 Profile of Reynolds Shear Stress of τ_{xz} for 20 cfs Cross Section 8 Piezo e

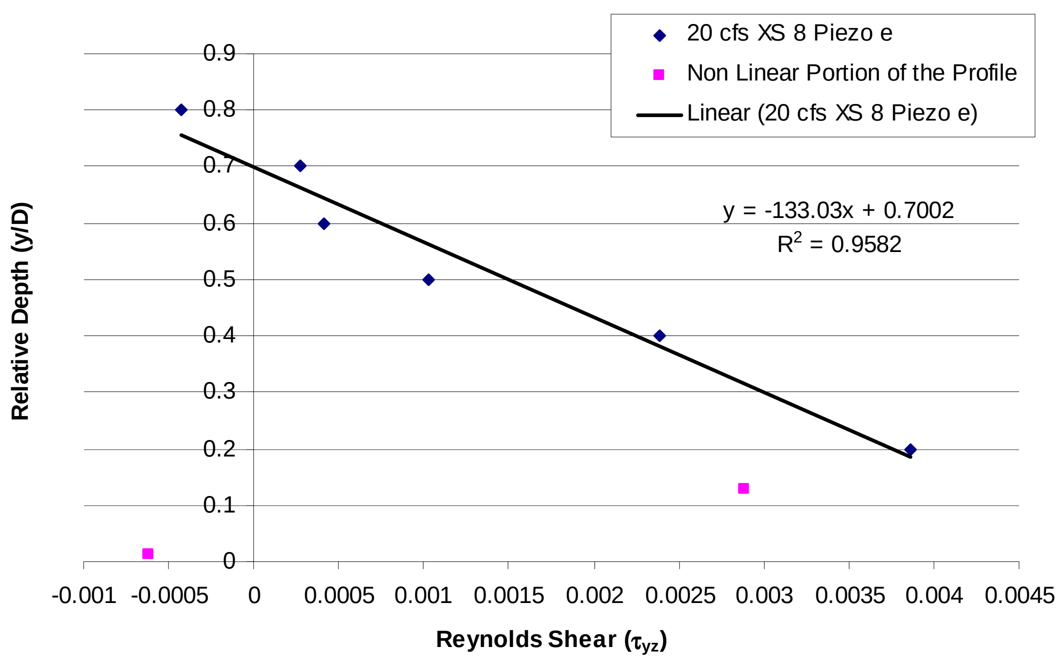

Figure 3.12 Profile of Reynolds Shear Stress of τ_{zy} for 20 cfs Cross Section 8 Piezo e

Figure 3.13 through Figure 3.16 present the shear stress distribution for overall flow rate of 8, 12, 16 and 20 cfs. The lowest value of Reynolds shear stress is indicated by a violet color and the highest value of turbulent shear stress is indicated by a red color. The value of τ_{bed} ranged from 0.002 psf to 0.058 psf. The location of the maximum value of τ_{bed} was observed at the near apex of the downstream bend.

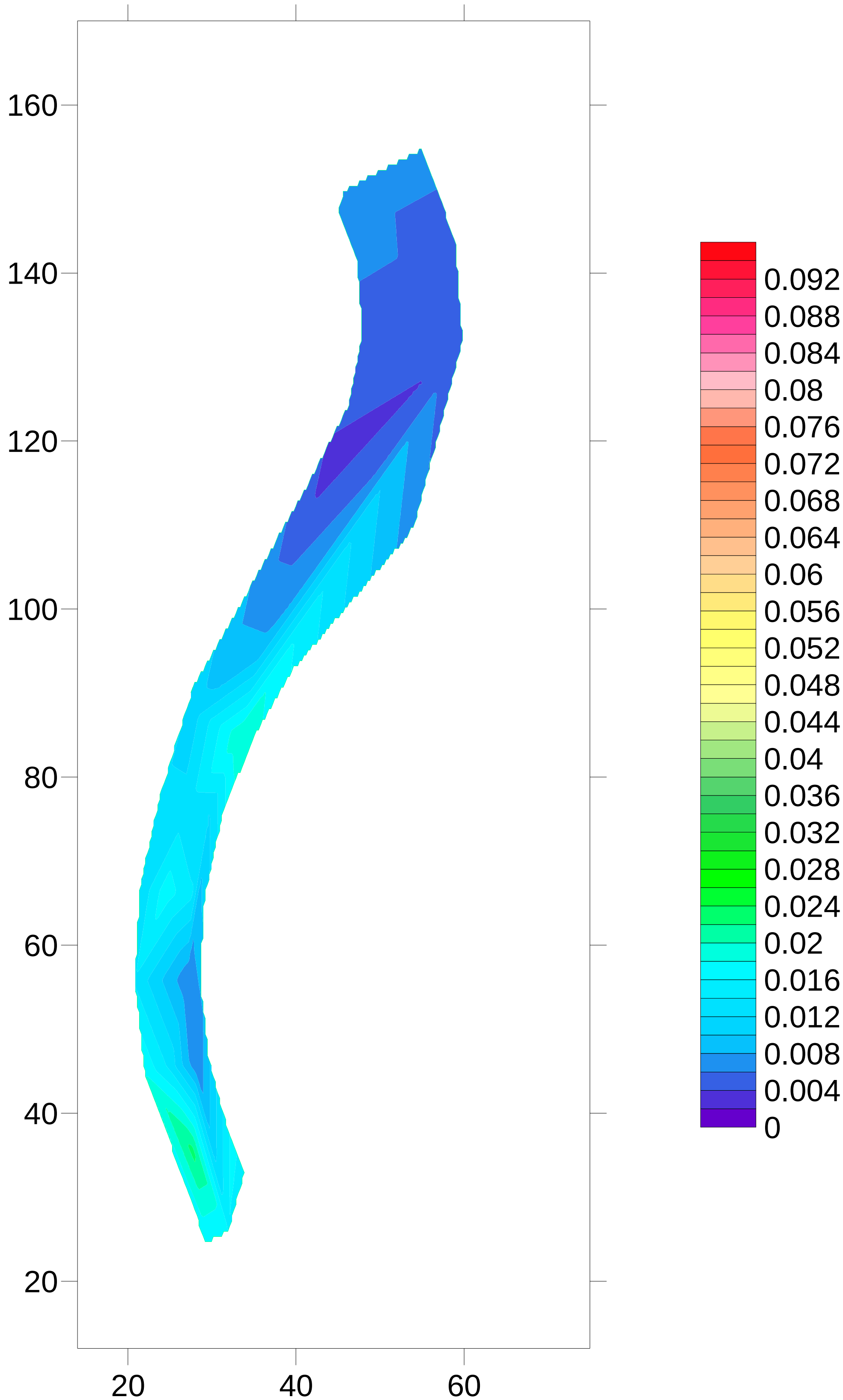

Figure 3.13 Contour Map of τ_{bed} from Reynolds Shear Stress for 8 cfs (psf)

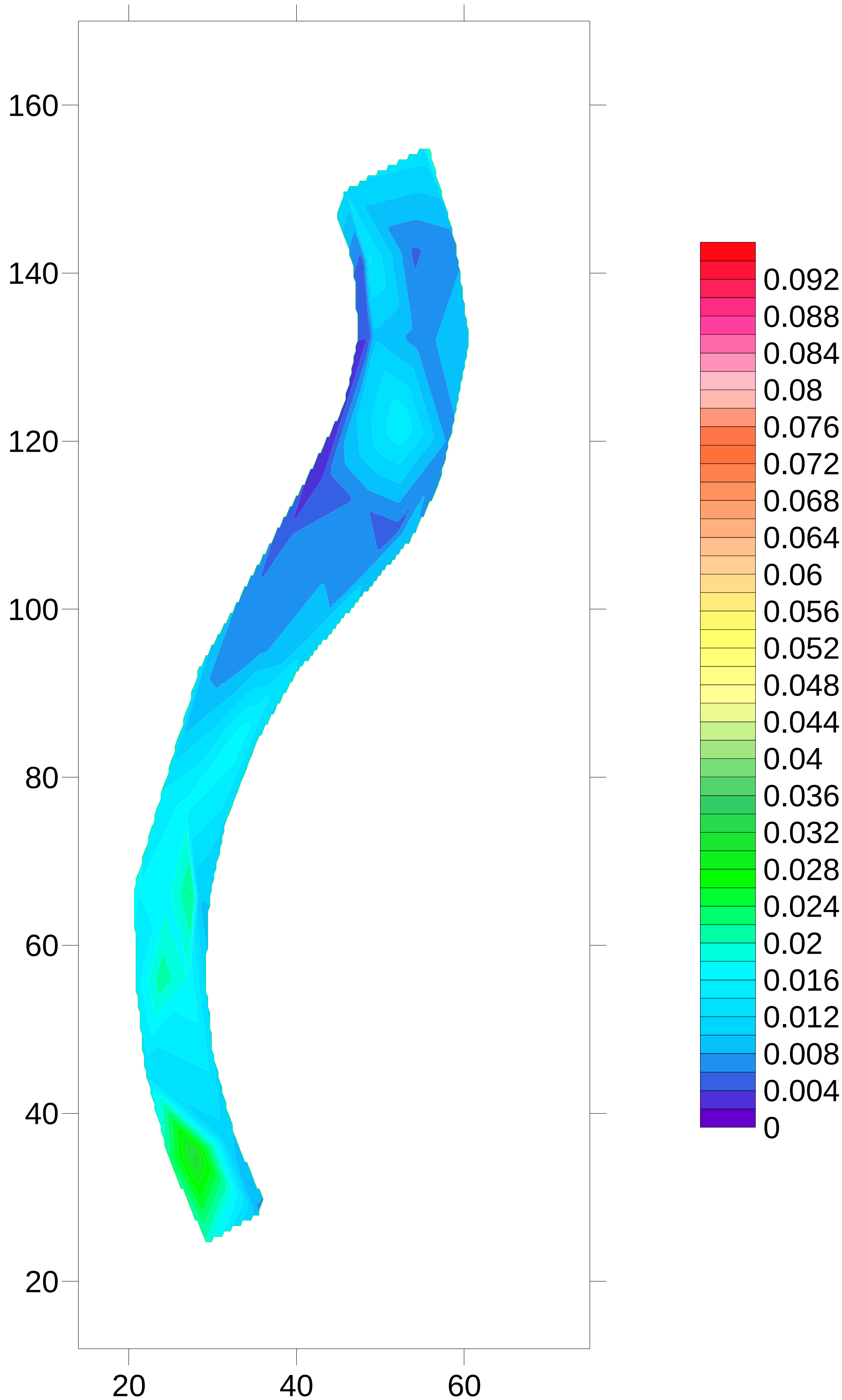

Figure 3.14 Contour Map of τ_{bed} from Reynolds Shear Stress for 12 cfs (psf)

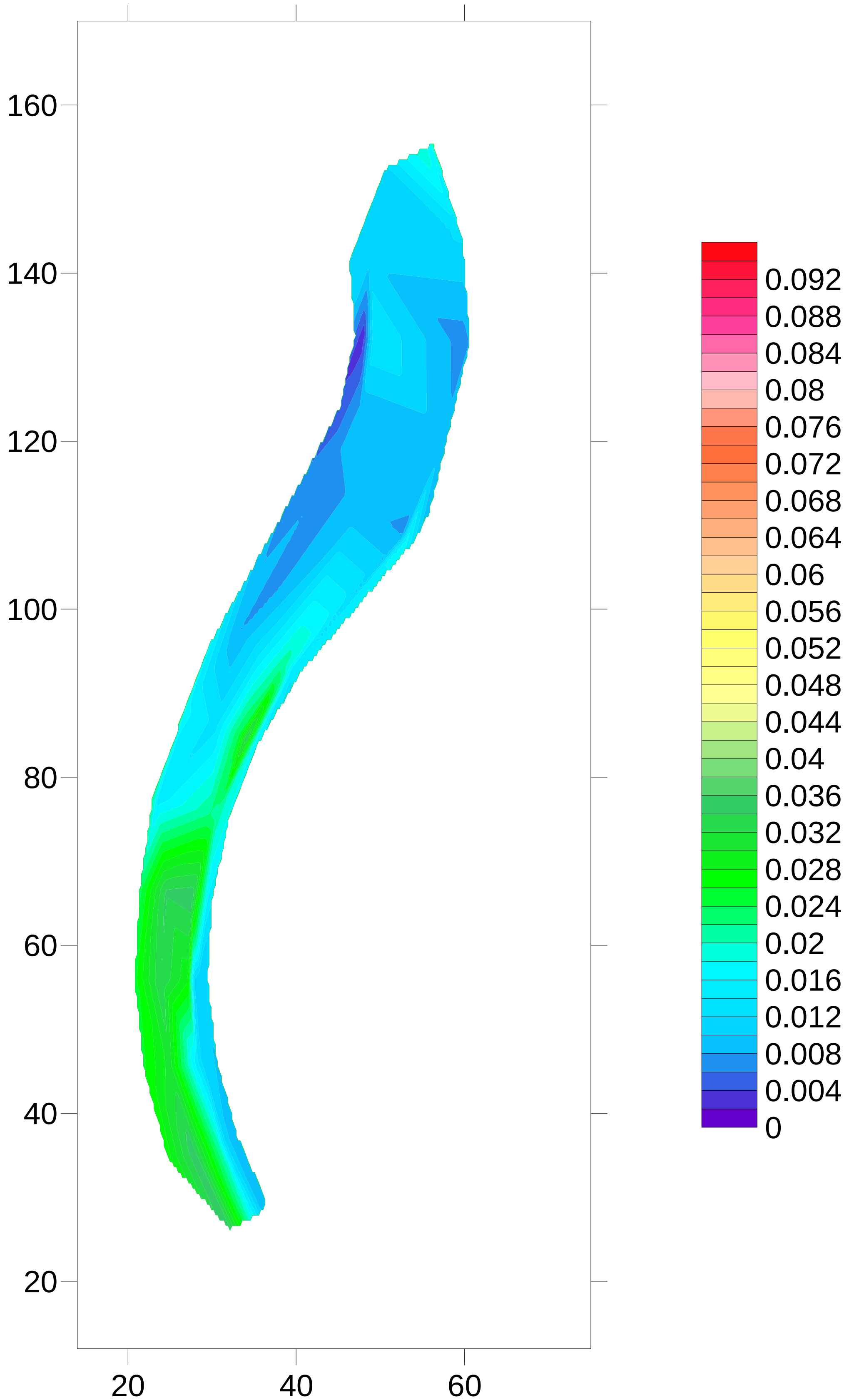

Figure 3.15 Contour Map of τ_{bed} from Reynolds Shear Stress for 16 cfs (psf)

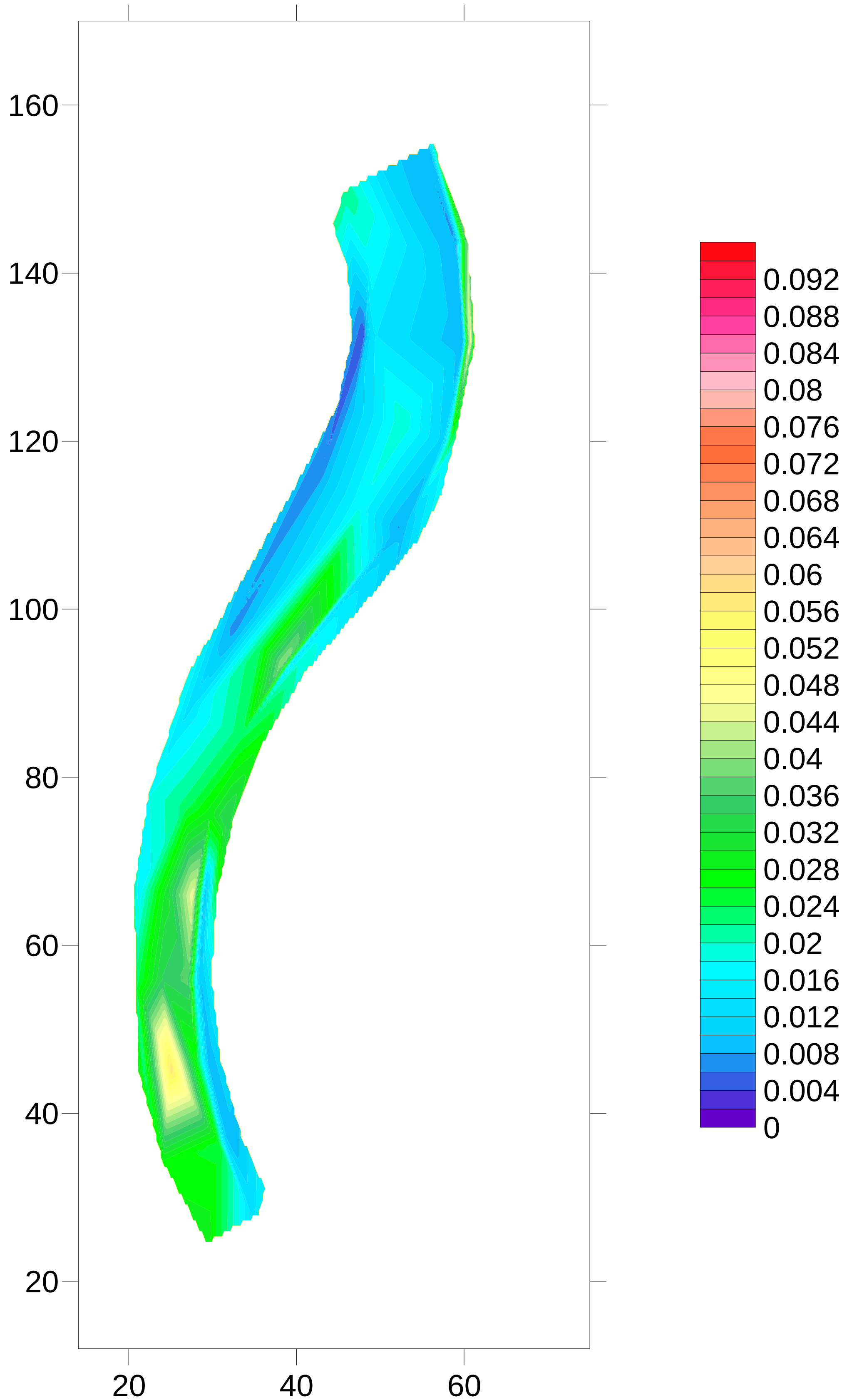

Figure 3.16 Contour Map of τ_{bed} from Reynolds Shear Stress for 20 cfs (psf)

3.3 Summary

During this study, data analysis was conducted to calculate shear stress by using the following methods; a) Preston tube b) Linear regression of flow velocity profile c) Rozovskii method d) Reynolds shear stress extrapolation. Generally, shear stress from Preston tube showed higher values than any other shear stress from different methods. According to the results of the data analysis, shear stress calculation from Preston tube and Reynolds shear stress extrapolation showed the best agreement because both methods showed proportionality of τ_x with the increase of flow rate and showed similar distribution of the value of τ_x. Especially, both methods showed that the similar trend of τ_x value that indicates reinforced bank protection is required at the inside of the downstream bend in the channel. In addition, the agreements indicated that the flow velocity from the ADV meter is a good parameter for predicting the shear stress distribution.

4 Comparisons of Shear Stress Calculation Methods

In Chapter 3, there were differences of shear stress calculation results due to the choice of different shear stress calculation methods. In this chapter, the differences in the shear stress calculations will be described. The method of comparison is presented in Figure 4.1.

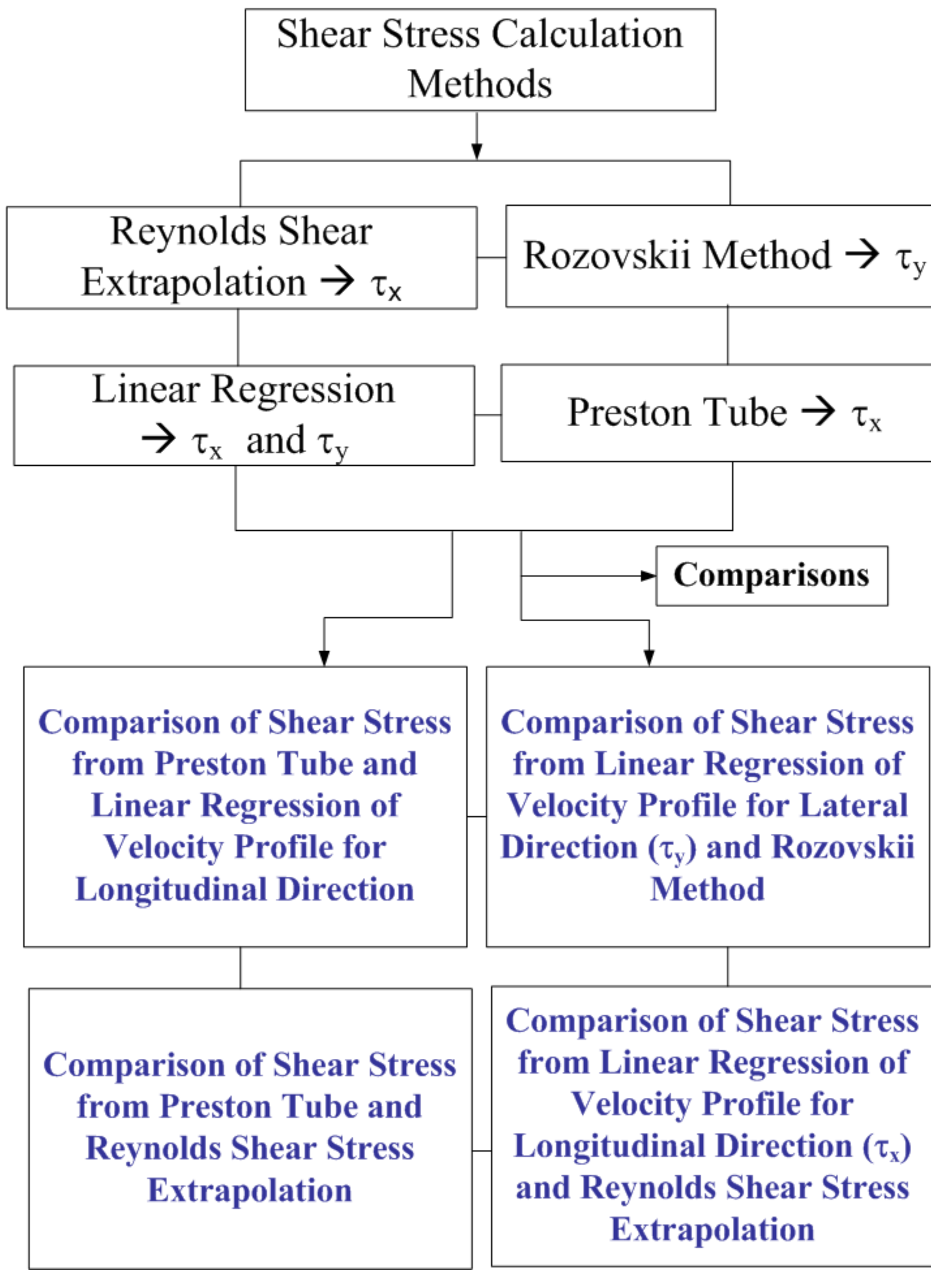

Figure 4.1 Chart of Shear Stress Calculation Methods Comparison

4.1 Comparison of Shear Stress from Preston Tube and Linear Regression of Velocity Profile for Longitudinal Direction

Plots to observe the difference of the two methods are presented in Figure 4.2 through Figure 4.5. The x-axis is shear stress from linear regression of flow velocity profile and y-axis is shear stress from Preston tube, respectively. If the points perfectly fit the y=x line, then the two methods have perfect agreement. Figure 4.2 through Figure 4.5 indicate that most of the points are concentrated in the vicinity of the y-axis, which means shear stress calculated from Preston tube is much greater. The green line in the plots indicates the best fit line from different shear stress calculation methods. The most persuasive reason for the difference of the two methods is the difference of measurement method. Preston tube was directly installed on the bed but the ADV can not be located on the bed because the ADV can not recognize the flow velocity on the bed. Therefore, shear stress from a linear regression of the flow velocity profile underestimates bed shear stress. Additionally, the averaged percentage difference of the two methods with change of discharge was presented in Figure 4.6.

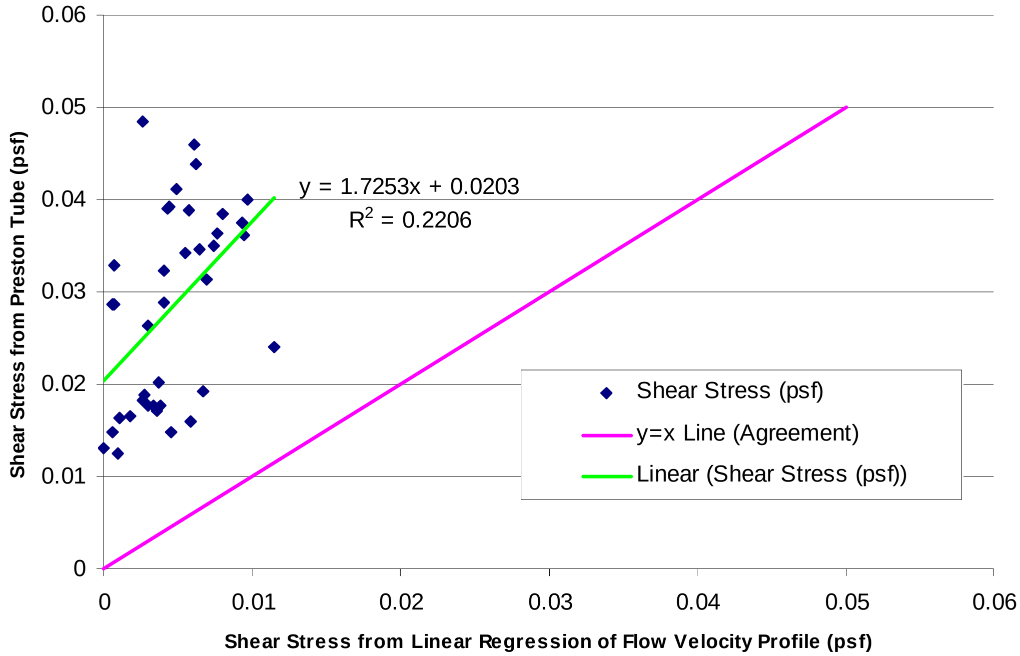

Figure 4.2 Comparison of Shear Stress from Preston Tube and Linear Regression of Flow Velocity Profile for 8 cfs

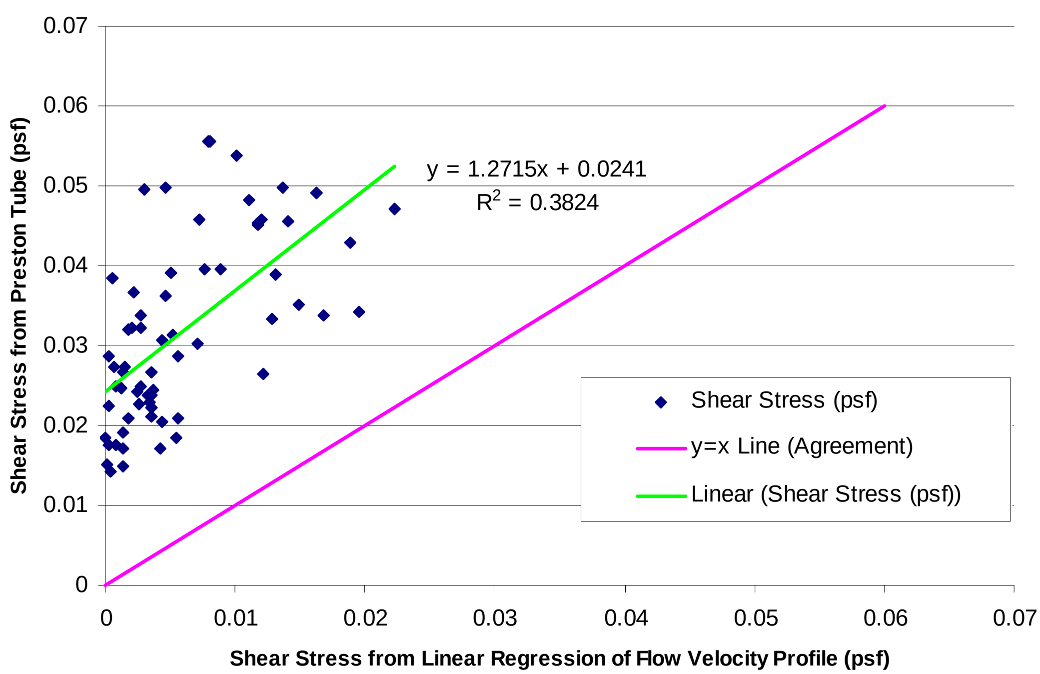

Figure 4.3 Comparison of Shear Stress from Preston Tube and Linear Regression of Flow Velocity Profile for 12 cfs

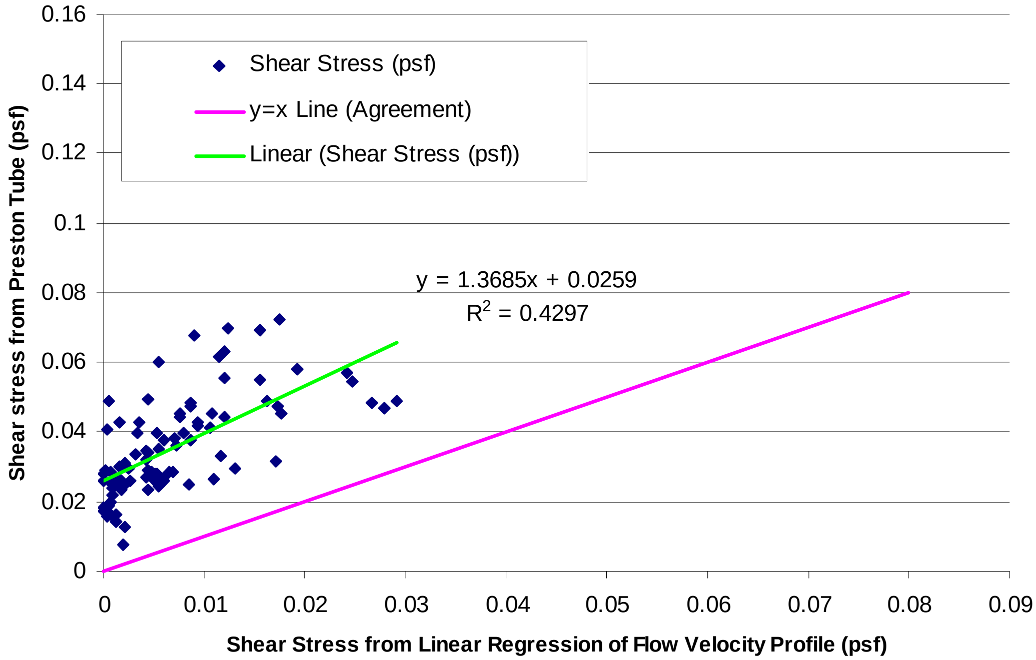

Figure 4.4 Comparison of Shear Stress from Preston Tube and Linear Regression of Flow Velocity Profile for 16 cfs

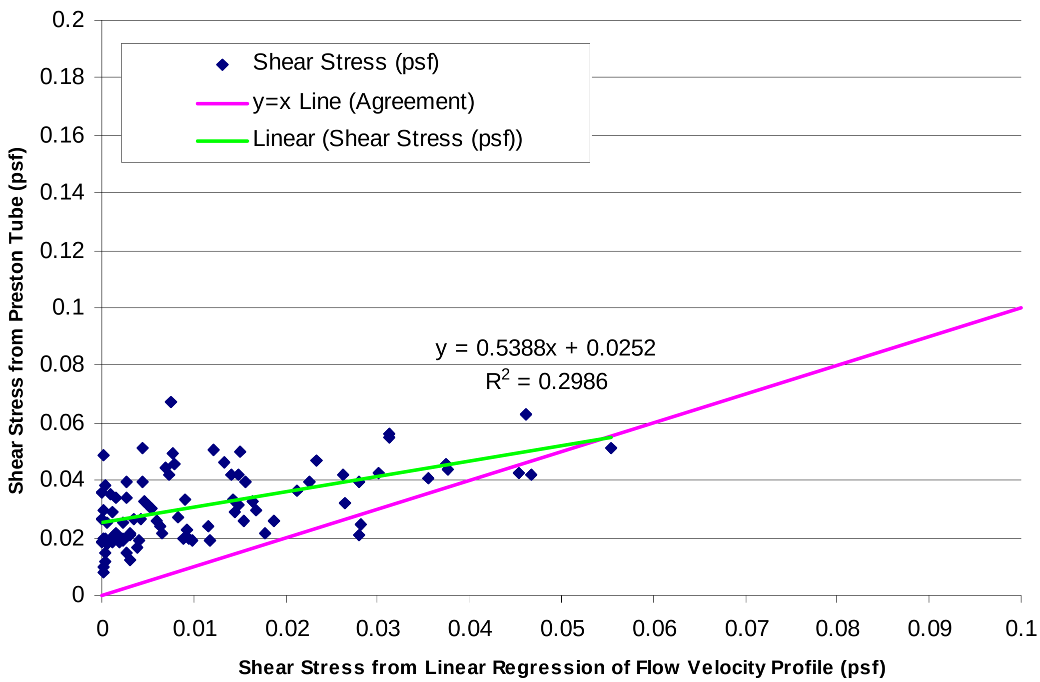

Figure 4.5 Comparison of Shear Stress from Preston Tube and Linear Regression of Flow Velocity Profile for 20 cfs

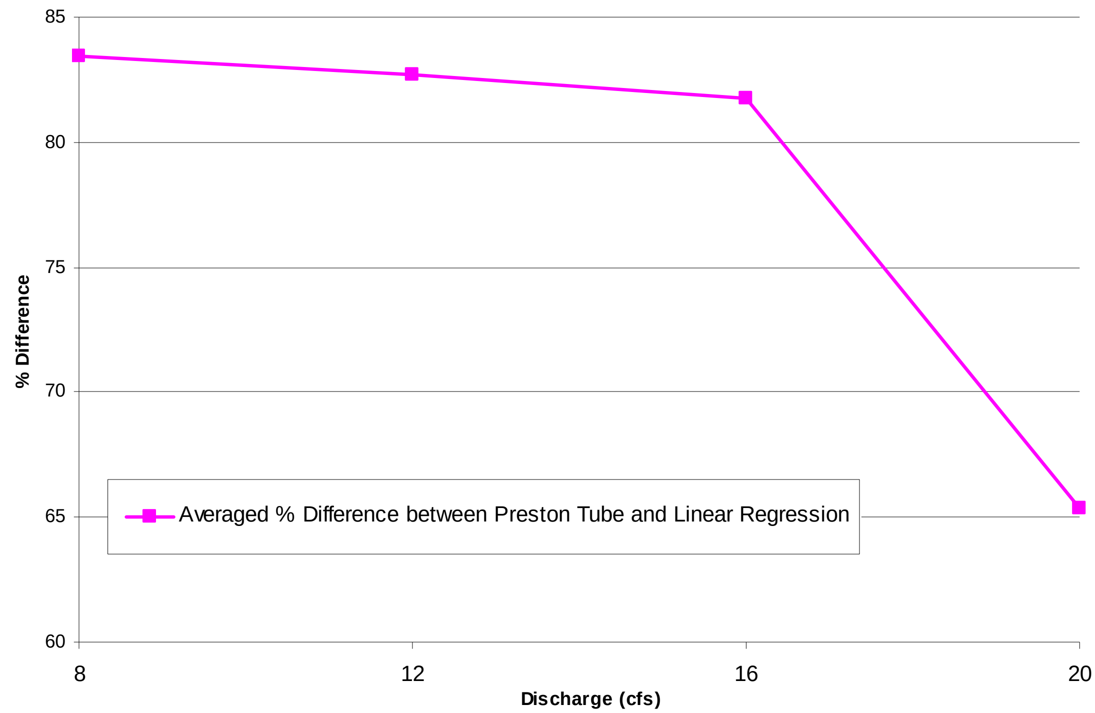

Figure 4.6 Averaged Percentage Difference between Preston Tube and Linear Regression with Change of Discharge

The percentage difference value of shear stress from Preston tube and linear regression of flow velocity profile was computed by using Equation 4.1.

$$\delta = \left(\frac{\alpha - \beta}{\alpha} \right) \times 100$$ **Equation 4.1**

Where, δ = the shear stress percentage difference between Preston tube and linear regression of flow velocity profile;

α = the value of shear stress by Preston tube; and

β = the hear stress from linear regression of flow velocity profile.

A summary table of the maximum and minimum of the percentage difference of the two methods is presented in Table 4.1.

Table 4.1 Calculation Results of Percentage Difference between Preston Tube and Linear Regression of Linear Flow Velocity Profile

Flow Rate (cfs)	Maximum Value (%)	Minimum Value (%)	Averaged Difference (%)
8	99.8	52.0	83.45
12	99.8	43.0	82.69
16	100	40.4	81.75
20	100	-6.7	67.42

4.2 Comparison of Shear Stress from Linear Regression of Velocity Profile for Lateral Direction (τ_y) and Rozovskii Method

For a detailed analysis of the differences between the two methods, plots are presented in Appendix F to show the difference of the two methods. The x-axis is the shear stress from Rozovskii method and the y-axis is shear stress from linear regression for lateral flow velocity, V_y. The plots indicate the points are mostly distributed horizontally because of the negative shear stress from Rozovskii method. The negative shear stress from Rozovskii method resulted from a lower water surface slope. As presented in Equation 2.22, the low water surface slope caused the right hand side bracket of Equation 2.22 to be greater. As a result, negative shear stress was observed from Rozovskii Method. The percentage difference between the shear stress from linear regression of the velocity profile for the lateral direction and Rozovskii method was calculated by using Equation 4.2. The summary of the comparison of two methods is shown in Table 4.2.

$$\delta_1 = \left(\frac{\alpha_1 - \beta_1}{\alpha_1}\right) \times 100 \qquad \textbf{Equation 4.2}$$

Where, δ_1 = the percentage difference between Preston tube and Rozovskii Method (%);

α_1 = the value of shear stress by linear regression of lateral flow velocity (V_y); and

β_1 = the value of shear stress from the Rozovskii method.

Table 4.2 Calculation Results of Percentage Difference between Linear Regression and Rozovskii Method

Flow Rate (cfs)	Maximum Value (%)	Minimum Value (%)	Averaged Difference (%)
8	-123.17	-84.64	-99.20
12	434.76	-19.95	-92.10
16	-757.42	-45.01	-104.78
20	-205.69	-2.83	-99.65

4.3 Comparison of Shear Stress from Preston Tube and Reynolds Shear Stress Extrapolation

Plots to compare the difference of shear stress from Preston tube and Reynolds shear stress are presented in Figure 4.7 through Figure 4.10. In addition, the averaged percentage difference of the two methods with change of discharge was presented in Figure 4.11. The x-axis is shear stress from Reynolds shear stress extrapolation obtained from Equation 4.3 and the y-axis is shear stress from Preston tube. The green line in the plots indicates the best fit line from different shear stress calculation methods. The plots indicates that the points are generally located between the y axis and the y=x curve. That means the shear stress from Preston tube is higher than shear stress from Reynolds shear stress extrapolation because the Preston tube directly touches on the bed surface of the flume but Reynolds shear from ADV does not touch the bed surface during data collection.

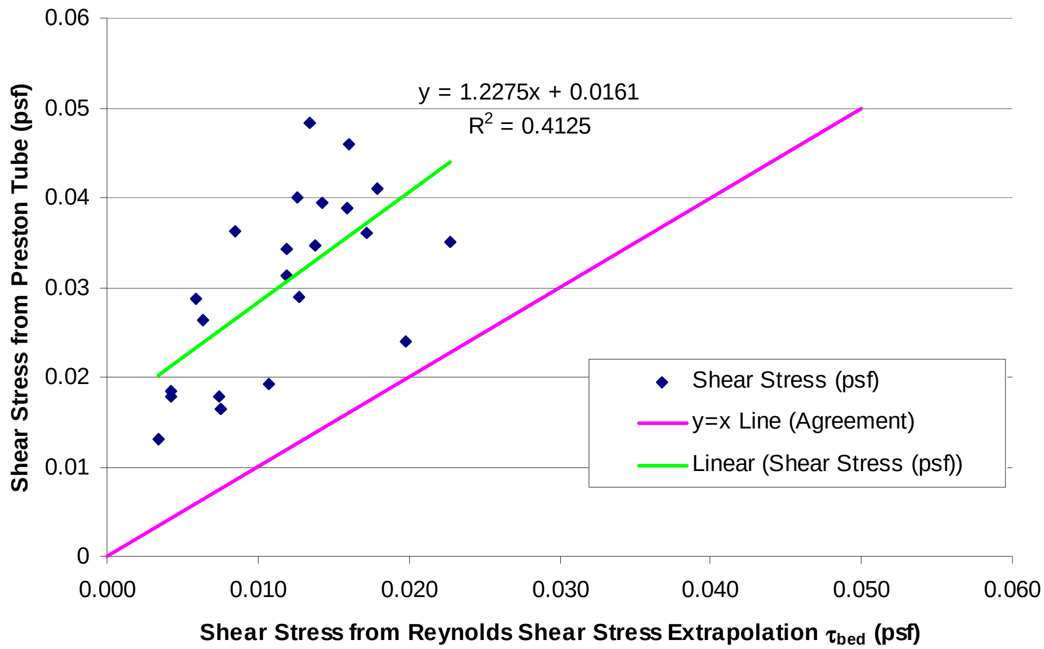

Figure 4.7 Comparison of Shear Stress from Preston Tube and Reynolds Shear Stress Extrapolation for 8 cfs

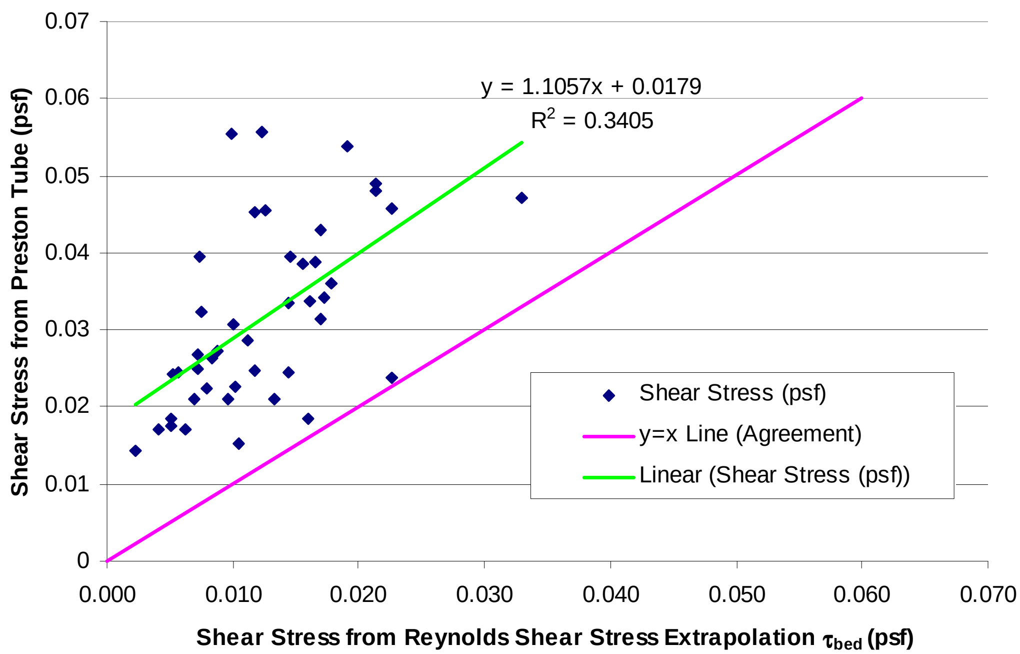

Figure 4.8 Comparison of Shear Stress from Preston Tube and Reynolds Shear Stress Extrapolation for 12 cfs

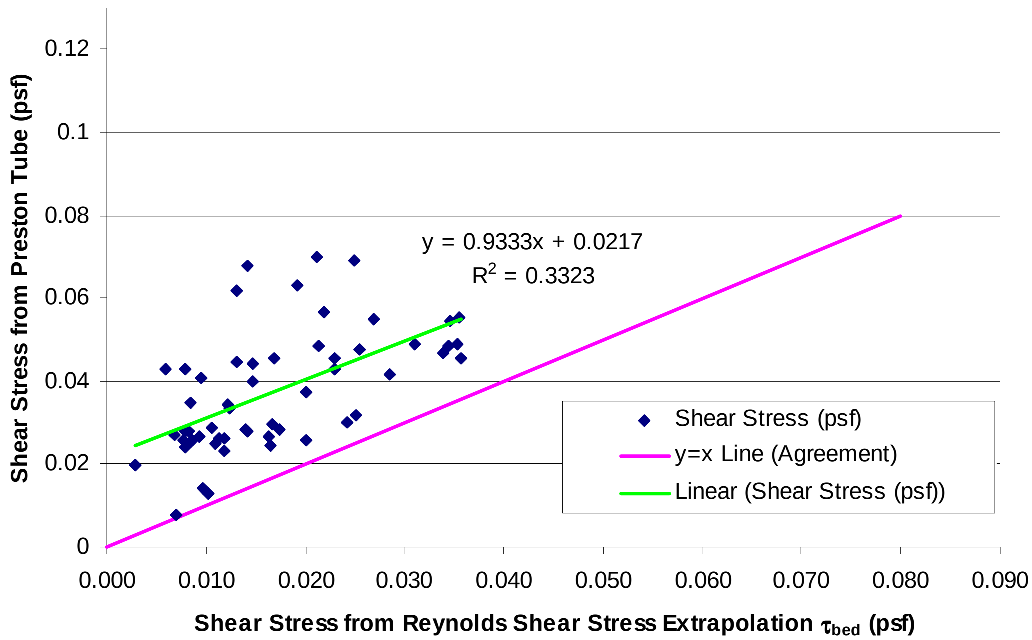

Figure 4.9 Comparison of Shear Stress from Preston Tube and Reynolds Shear Stress Extrapolation for 16 cfs

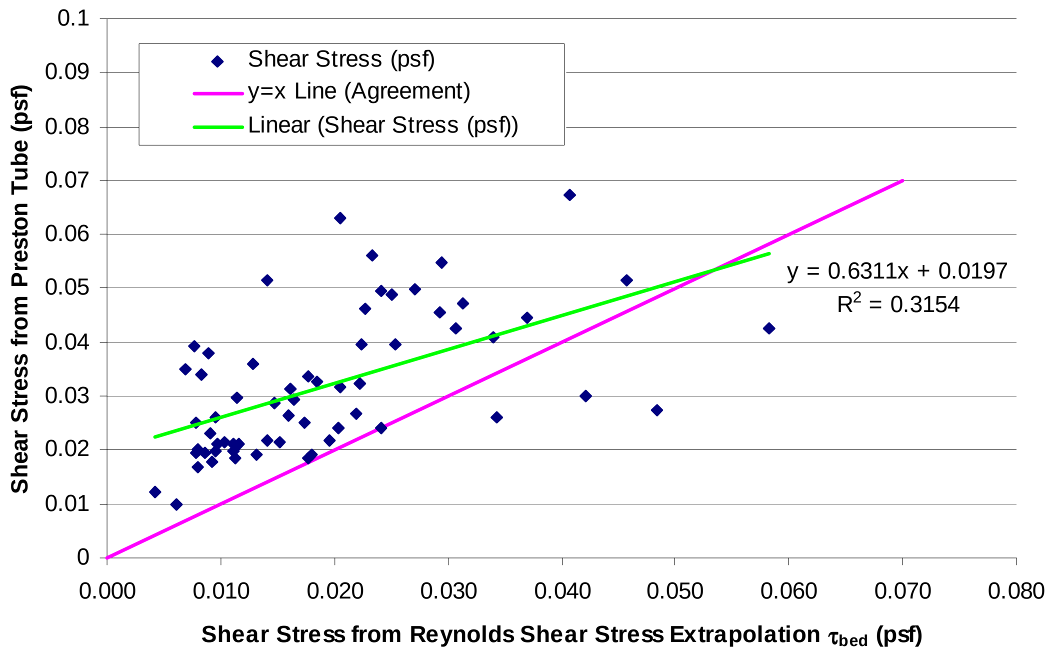

Figure 4.10 Comparison of Shear Stress from Preston Tube and Reynolds Shear Stress Extrapolation for 20 cfs

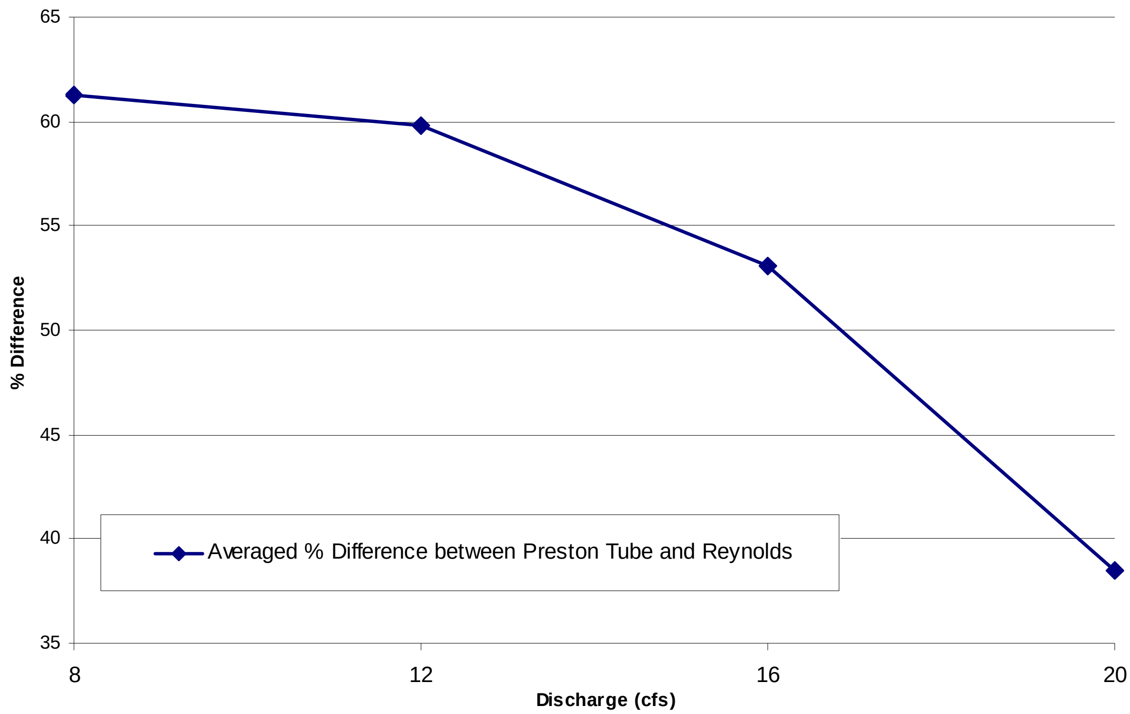

Figure 4.11 Averaged Percentage Difference between Preston Tube and Reynolds Shear Extrapolation with Change of Discharge

The percentage difference of shear stress from Preston tube and the Reynolds shear extrapolation method was obtained by using the Equation 4.3. Table 4.3 presents the difference of the calculation results.

$$\delta_2 = \left(\frac{\alpha_2 - \beta_2}{\alpha_2} \right) \times 100 \qquad \textbf{Equation 4.3}$$

Where, δ_2 = the shear stress percentage difference between Preston tube and Reynolds shear stress extrapolation (%);

α_2 = the value of shear stress calculated from the Preston tube; and

β_2 = the shear stress from Reynolds shear stress extrapolation.

Table 4.3 Calculation Results of Percentage Difference between Preston Tube and Reynolds Shear Extrapolation

Flow Rate (cfs)	Maximum Value (%)	Minimum Value (%)	Averaged Difference (%)
8	79.37	17.64	61.28
12	83.74	5.20	59.79
16	86.24	6.89	53.04
20	80.50	0.66	38.49

4.4 Comparison of Shear Stress from Linear Regression of Velocity Profile for Longitudinal Direction (τ_x) and Reynolds Shear Stress Extrapolation

Plots comparing differences of shear stress using a linear regression of the flow velocity profile along the x axis and Reynolds shear stress are presented in Figure 4.12 through Figure 4.15. The x-axis is shear stress from linear regression of longitudinal flow direction and y-axis is shear stress from Reynolds shear stress extrapolation. The plots indicate shear stress from Reynolds shear stress extrapolation is greater than shear stress from linear regression because Reynolds shear extrapolation was calculated by obtaining the x-axis intercept point of the linear portion of relative depth and shear stress, but shear stress from linear regression of the longitudinal flow velocity was obtained from the slope of the linear regression equation. The green line in the plots indicates the best fit line from different shear stress calculation methods. Additionally, the averaged percentage difference of the two methods with change of discharge is presented in Figure 4.16.

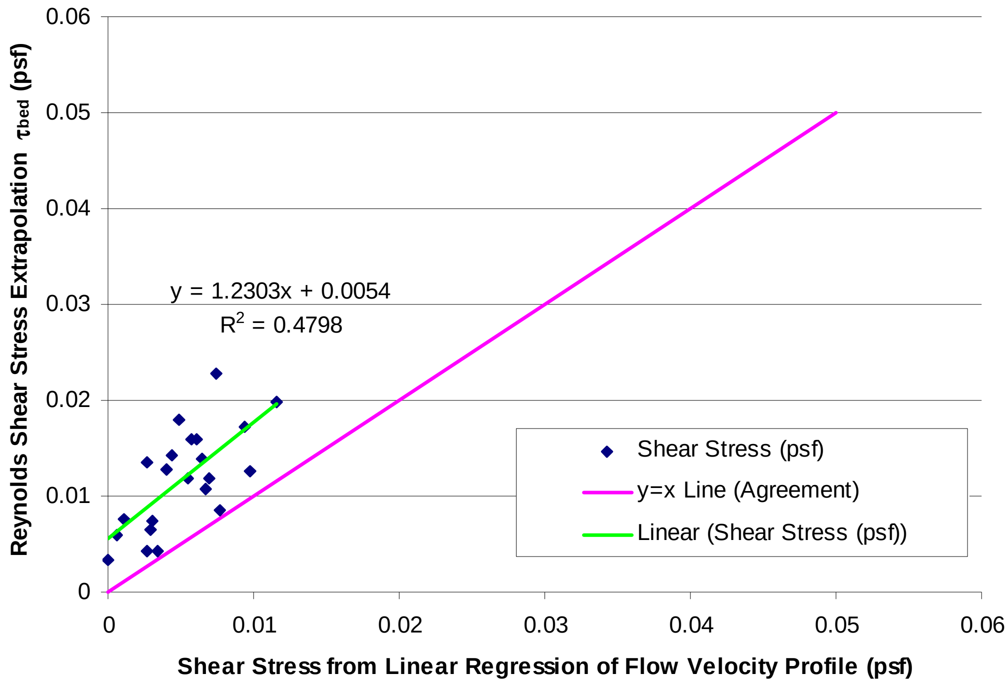

Figure 4.12 Comparison of Shear Stress from Linear Regression and Reynolds Shear Stress Extrapolation for 8 cfs

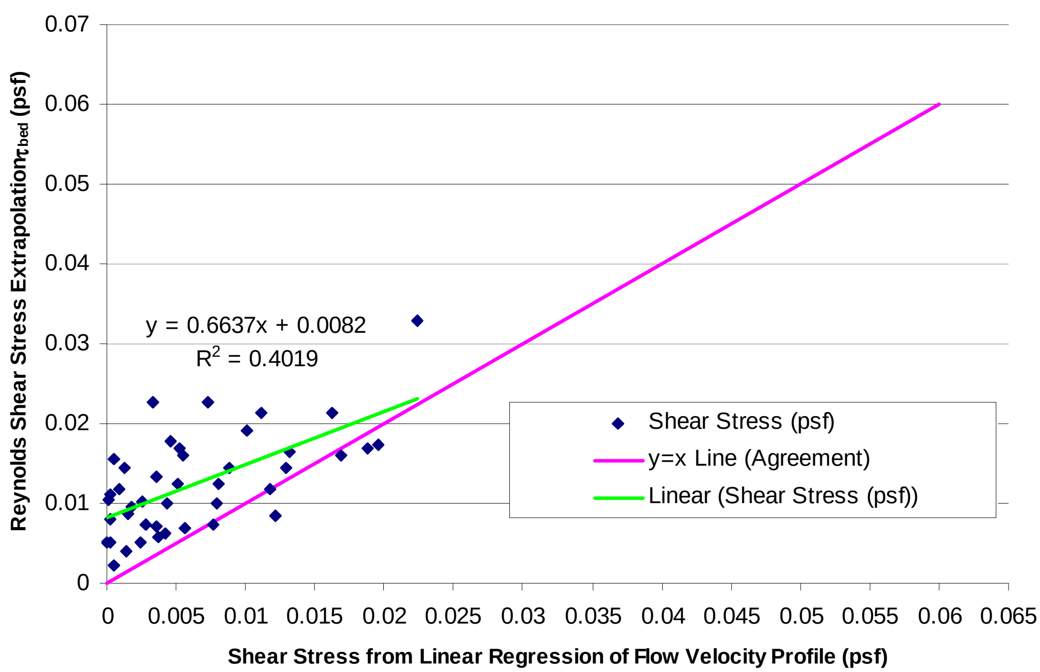

Figure 4.13 Comparison of Shear Stress from Linear Regression and Reynolds Shear Stress Extrapolation for 12 cfs

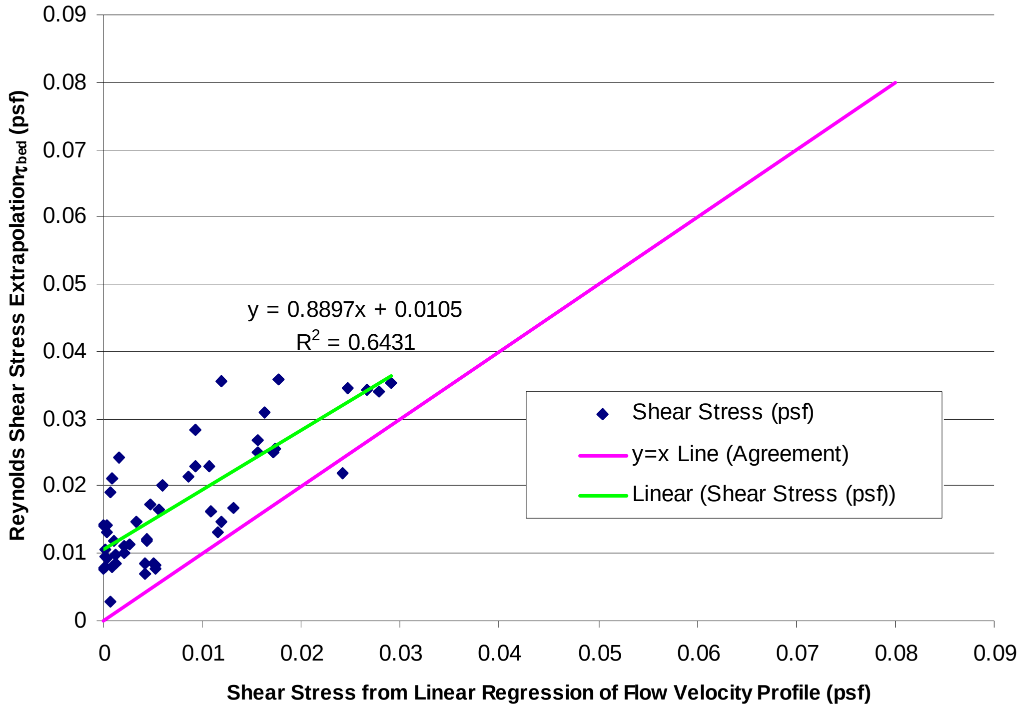

Figure 4.14 Comparison of Shear Stress from Linear Regression and Reynolds Shear Stress Extrapolation for 16 cfs

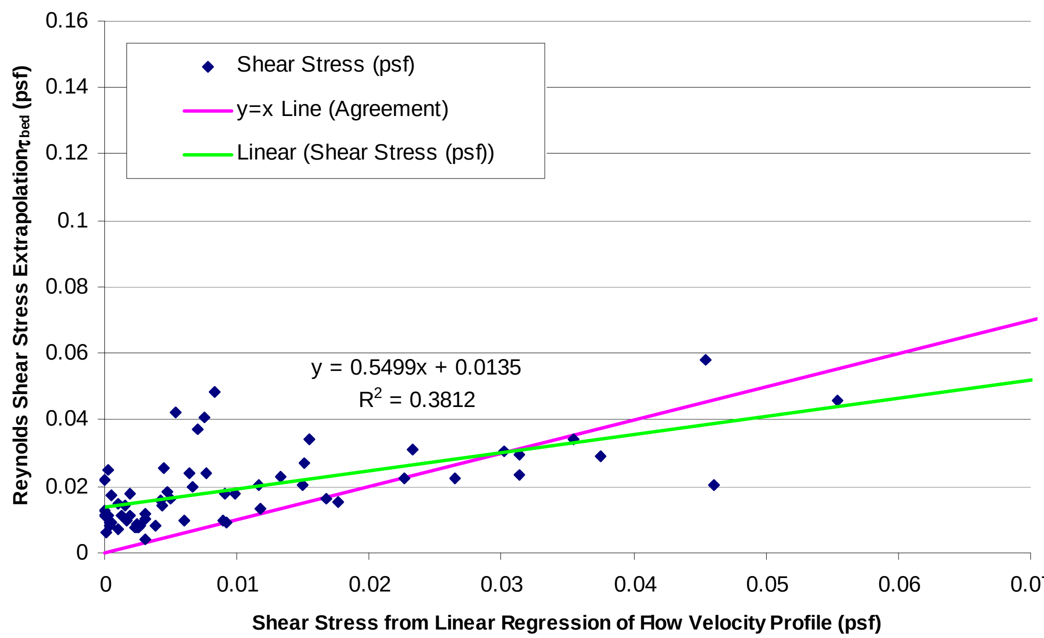

Figure 4.15 Comparison of Shear Stress from Linear Regression and Reynolds Shear Stress Extrapolation for 20 cfs

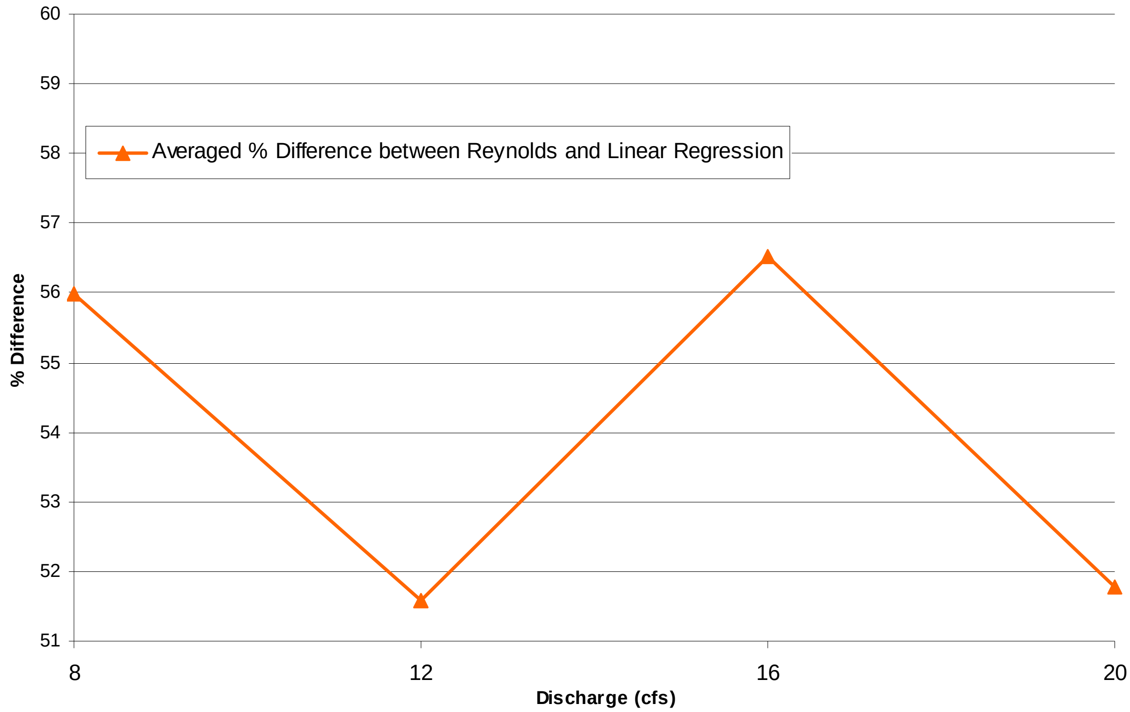

Figure 4.16 Averaged Percentage Difference between Reynolds Shear Extrapolation and Linear Regression with Change of Discharge

Another way to compare with shear stress calculation method is comparing shear stress from linear regression of x-direction flow velocity and shear stress by extrapolating Reynolds shear stress that applies in the bed (τ_{bed}). The percentage difference of shear stress calculated from linear regression of longitudinal flow velocity and Reynolds shear stress extrapolation was obtained using Equation 4.4. Table 4.4 presents the difference of the calculation results.

$$\delta_3 = \left(\frac{\alpha_3 - \beta_3}{\alpha_3} \right) \times 100 \qquad \textbf{Equation 4.4}$$

Where, δ_3 = the shear stress percentage difference between linear regression of the longitudinal flow velocity and Reynolds shear stress extrapolation (%);

α_3 = the value of shear stress by Reynolds shear stress extrapolation; and

β_3 = the shear stress from linear regression.

Table 4.4 Calculation Results of Percentage Difference between Linear Regression of longitudinal velocity and Reynolds Shear Extrapolation

Flow Rate (cfs)	Maximum Value (%)	Minimum Value (%)	Averaged Difference (%)
8	99.25	9.24	55.99
12	99.23	0.14	51.59
16	99.93	-10.07	56.53
20	-125.32	-1.1	51.77

4.5 Comprehensive Comparisons

Section 4.1 through Section 4.4 described the differences of shear stress calculation methods from Preston tube, linear regression of longitudinal flow velocity, Rozovskii method and Reynolds shear stress extrapolation. This chapter shows the shear stress calculated from Preston tube is the most accurate method because the Preston tube directly touched on the bed of the channel during data collection. In the case of Reynolds shear stress extrapolation and linear regression method, these methods are based on the ADV data, and the ADV that does not directly touch the bed of the channel during measurements.

Bar charts are presented in Figure 4.17 through Figure 4.20 that shows the percentage difference between maximum shear stress from Preston tube and other maximum shear stress values by using Reynolds shear stress extrapolation, linear regression and HEC-RAS. Due to the low accuracy, shear stress from Rozovskii method was excluded in the bar charts. The plots indicate that Reynolds shear stress extrapolation has relatively better agreement with shear stress from Preston tube than a linear regression of flow velocity profile.

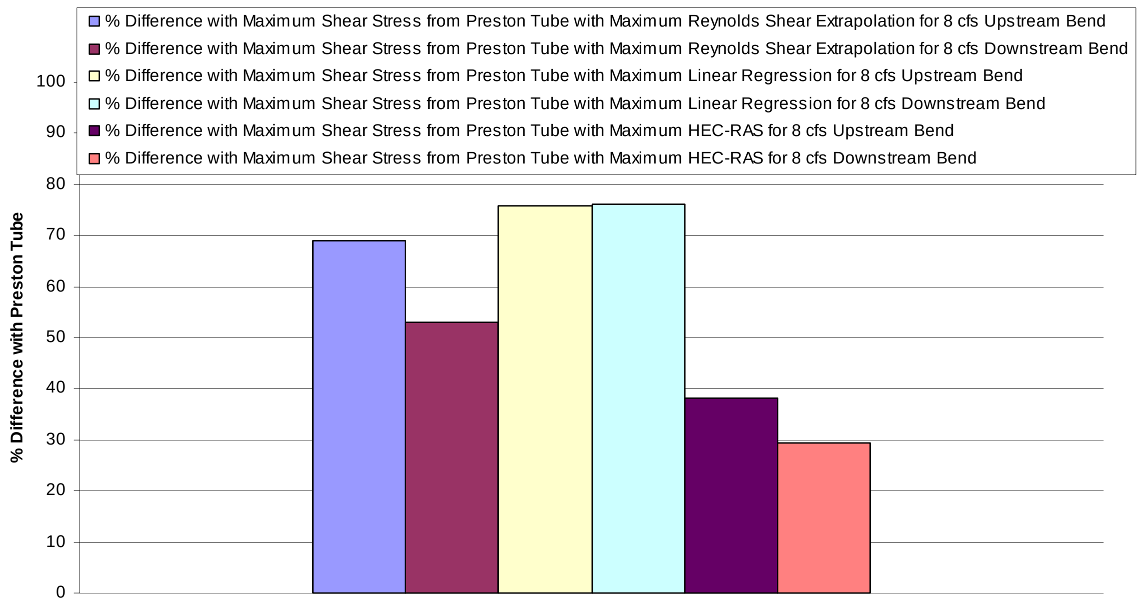

Figure 4.17 Percentage Difference of Maximum Shear Stress with Preston Tube for 8 cfs

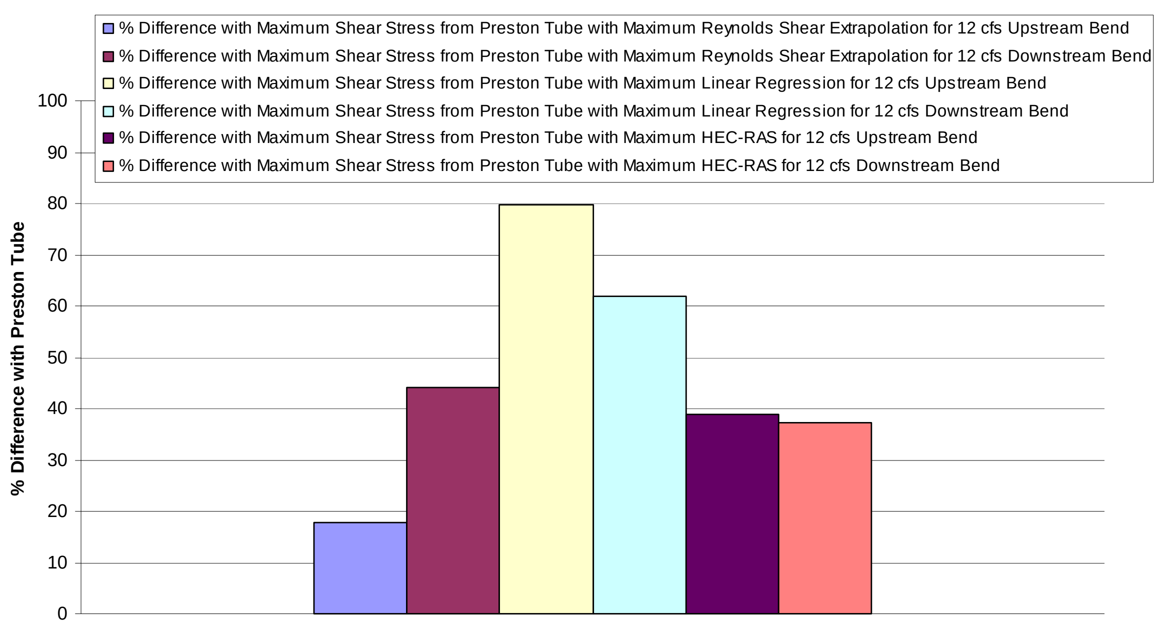

Figure 4.18 Percentage Difference of Maximum Shear Stress with Preston Tube for 12 cfs

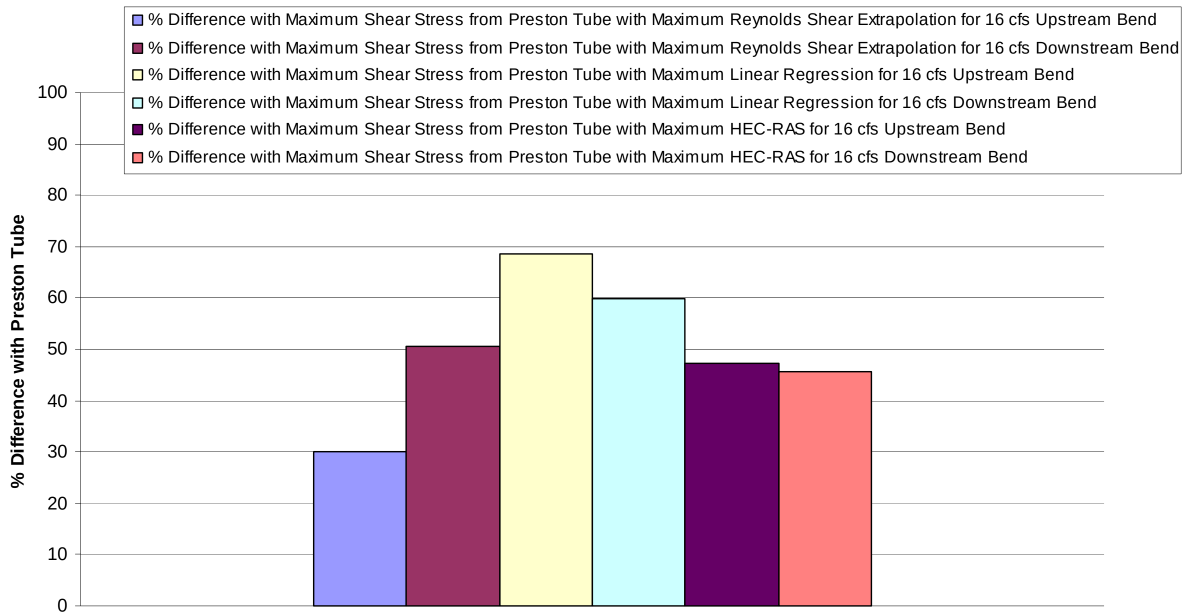

Figure 4.19 Percentage Difference of Maximum Shear Stress with Preston Tube for 16 cfs

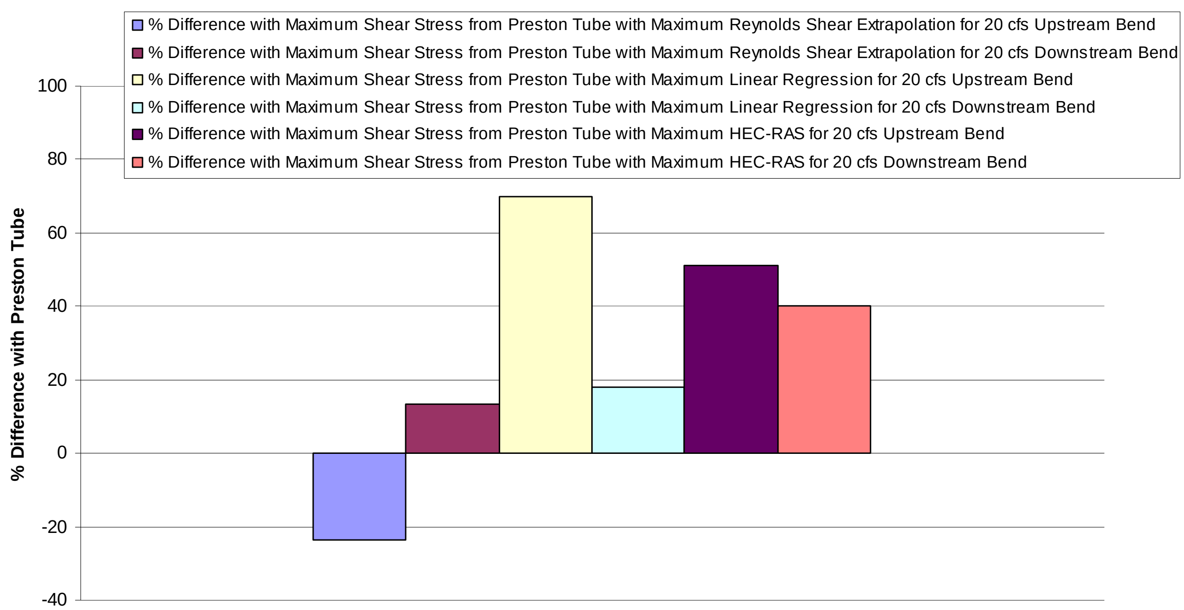

Figure 4.20 Percentage Difference of Maximum Shear Stress with Preston Tube for 20 cfs

4.6 Averaged Shear Stress from HEC-RAS and K_b Value

Heintz (2002) explained that an adjustment factor, K_b should be developed due to the different geometry condition between the upstream and downstream bend. The definition of K_b is the ratio of maximum shear stress to averaged shear stress. In this study, averaged shear stress was calculated by taking average the HEC-RAS shear stress output of cross section 1 and 2 for the upstream bend and taking the average output of cross section 10 and 11 for the downstream bend to calculate cross section averaged shear stress. HEC-RAS modeling output for shear stress is presented in Table 4.5 and Table 4.6. Two maximum shear stresses were selected for analysis; from extrapolation of Reynolds shear stress profile and from Preston tube method. The K_b value, computed by dividing maximum shear stress by cross section averaged shear stress from HEC-RAS, is presented and summarized in Table 4.7 and Table 4.8.

Table 4.5 HEC-RAS Output for Shear Stress for Upstream Bend (psf)

XS	8 cfs	12 cfs	16 cfs	20 cfs
1	0.014551	0.016432	0.018744	0.02055
2	0.012438	0.014542	0.016896	0.018763
3	0.014991	0.016844	0.019166	0.020974
4	0.014289	0.016125	0.018418	0.020209
5	0.013597	0.01551	0.01782	0.019631
6	0.014445	0.016236	0.018536	0.020332
7	0.012989	0.015048	0.017457	0.019347
8	0.013057	0.015025	0.017375	0.019229

Table 4.6 HEC-RAS Output for Shear Stress for Downstream Bend (psf)

XS	8 cfs	12 cfs	16 cfs	20 cfs
10	0.025227	0.029593	0.034569	0.038344
11	0.028996	0.032956	0.038042	0.041828
12	0.034162	0.036949	0.041766	0.045203
13	0.025574	0.029527	0.034338	0.037916
14	0.025627	0.029753	0.034675	0.038318
15	0.02509	0.029061	0.033865	0.037415
16	0.025559	0.029464	0.034246	0.037739
17	0.028973	0.032477	0.037302	0.040723
18	0.028534	0.031707	0.036329	0.039591

Table 4.7 K_b Value from Maximum Shear Stress of Reynolds Shear Stress

	Flow Rate	Averaged Shear Stress (psf)	Maximum Shear Stress (psf)	R_c/T_w	K_b Value	Location
Upstream	8 cfs	0.0134945	0.007502549	2.788572251	0.55597	XS 4 Piezo e
Downstream	8 cfs	0.0271115	0.022733373	6.913463558	0.83851	XS 16 Piezo d
Upstream	12 cfs	0.015487	0.022623014	2.617889474	1.46077	XS 4 Piezo b
Downstream	12 cfs	0.0312745	0.032936826	6.202185792	1.05315	XS 16 Piezo d
Upstream	16 cfs	0.01782	0.024180063	2.476354806	1.35691	XS 4 Piezo a
Downstream	16 cfs	0.0363055	0.03574071	5.720368439	0.98444	XS 17 Piezo d
Upstream	20 cfs	0.0196565	0.048435716	2.41252646	2.46411	XS 6 Piezo b
Downstream	20 cfs	0.040086	0.058249589	5.442294974	1.45312	XS 15 Piezo d

Table 4.8 K_b Value from Maximum Shear Stress of Preston Tube

	Flow Rate	Averaged Shear Stress (psf)	Maximum Shear Stress (psf)	R_c/T_w	K_b Value	Location
Upstream	8 cfs	0.0134945	0.024213	2.819001891	1.794286	XS 8 Piezo c
Downstream	8 cfs	0.0271115	0.048366069	6.814699793	1.78397	XS 15 Piezo d
Upstream	12 cfs	0.015487	0.027531493	2.620013523	1.77772	XS 5 Piezo a
Downstream	12 cfs	0.0312745	0.05886005	6.122581845	1.88205	XS 10 Piezo a
Upstream	16 cfs	0.01782	0.034551784	2.485886579	1.93893	XS 6 Piezo b
Downstream	16 cfs	0.0363055	0.072179902	5.720368439	1.98813	XS 17 Piezo e
Upstream	20 cfs	0.0196565	0.039212852	2.354478065	1.99491	XS 8 Piezo c
Downstream	20 cfs	0.040086	0.067410083	5.444995864	1.68164	XS 10 Piezo c

Before this study, Ippen and Drinker (1962), USBR (1964) and Yen (1965) performed research to figure out the empirical equations of K_b. After K_b values are obtained by using Reynolds shear stress and Preston tube, the empirical equations and upper envelope curves of K_b were obtained by taking the regression of the power function, including the data from previous studies by Ippen and Drinker (1962), USBR (1964) and Yen (1965). The plots are presented in Figure 4.21 and Figure 4.22.

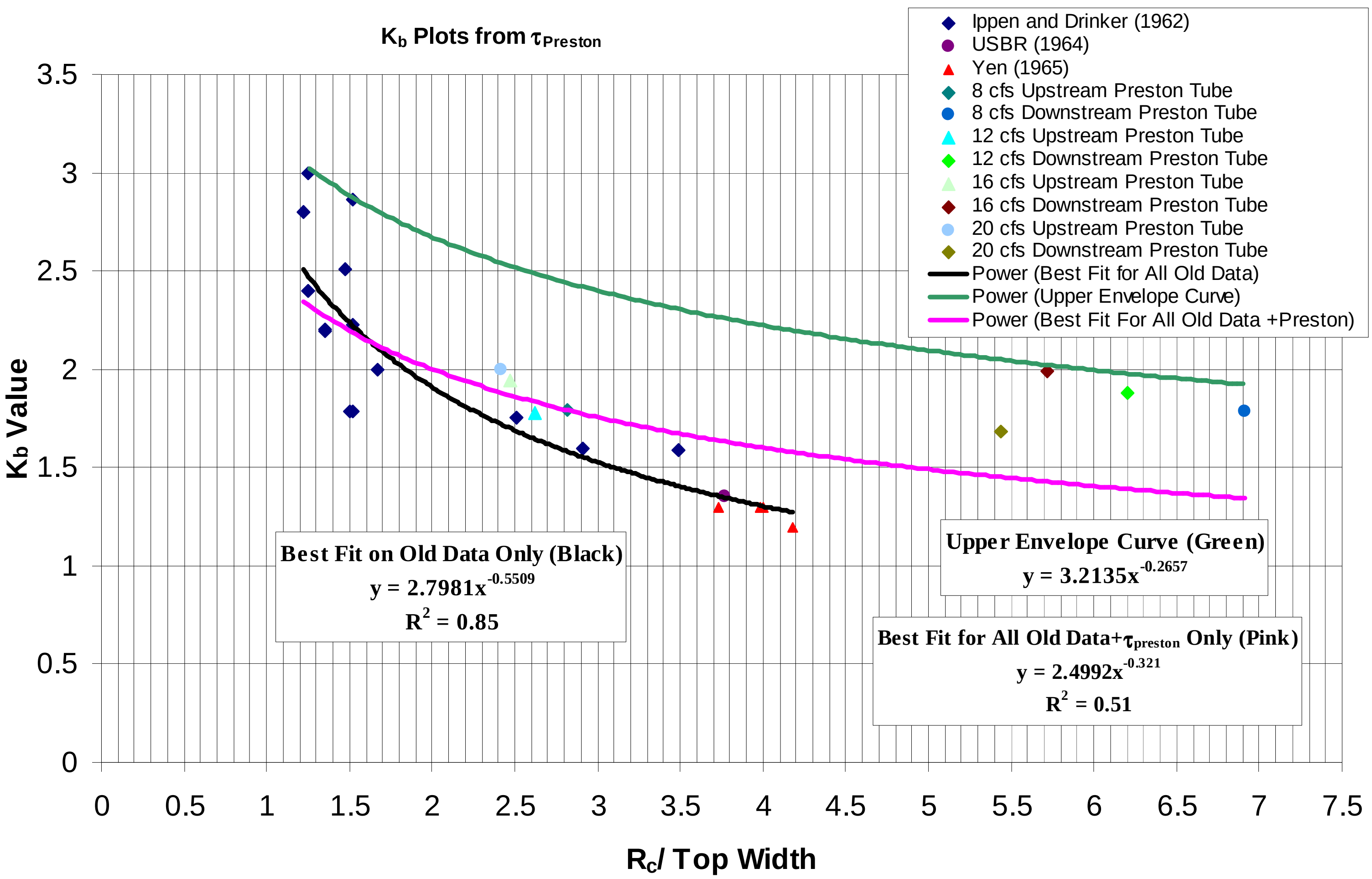

Figure 4.21 K_b Plots from the Ratio of Maximum Shear Stress from Preston Tube to Cross Section Averaged Shear Stress from HEC-RAS

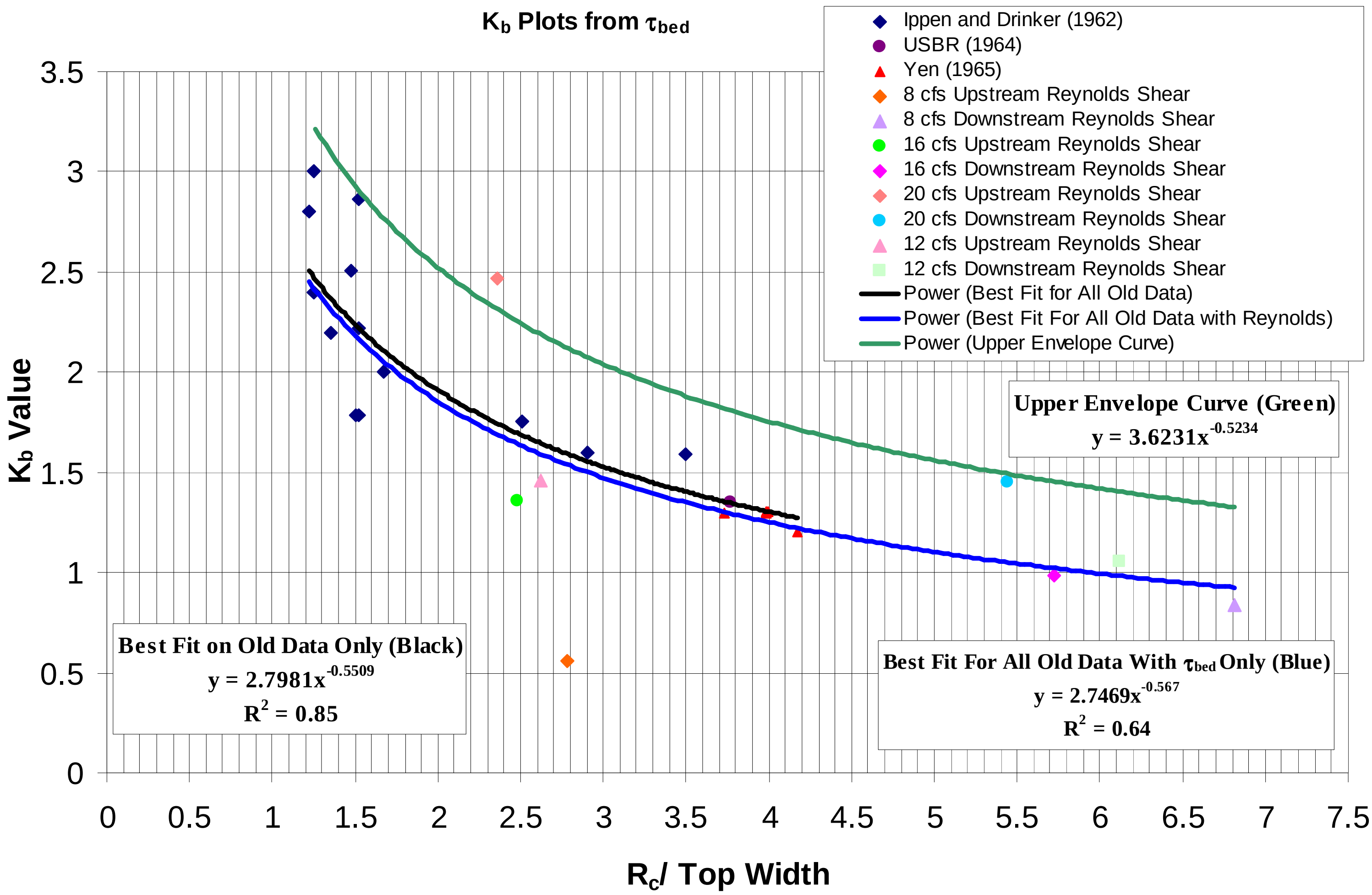

Figure 4.22 K_b Plots from the Ratio of Maximum Shear Stress from Reynolds Shear Stress to Cross Section Averaged Shear Stress from HEC-RAS

5 Conclusions and Recommendations

5.1 Overview

The physical model study provided the distribution of shear stress in a meandering channel. The previous research and laboratory experiments presented a guideline of shear stress analysis in a meandering channel. However, the previous studies about flow in bends have limitations because they focused on the distribution of shear stress in a single bend. This study presented data analysis results to determine shear stress in a meandering channel by performing laboratory tests. The flume is constructed as the combination of two types of bends; type 1 and type 3. The ratio of radius of curvature and top width of type 1 and type 3 bend in the flume was 2.02 and 4.39, respectively.

5.2 Conclusions

To determine the shear stress distribution in a meandering channel, the physical modeling study was conducted in the following phases.

a) Model construction and calibration;

b) Data collection of flow depth, flow velocity and boundary shear stress;

c) Data analysis.

After the study procedures presented above, the following conclusions were drawn from this experimental study.

- The shear stress from the method of Rozovskii (1961) that was presented in Equation 2.2 only shows the shear stress that applies in the lateral direction. On the other hand, the shear stress from the Preston tube and the Reynolds shear extrapolation show total shear stress. Therefore, the shear stress from Rozovskii (1961) was significantly smaller than the shear stress from the Preston tube and the Reynolds shear stress extrapolation.
- The shear stress from the Preston tube is the most accurate value among those obtained by four different methods because the Preston tube collects directly on the surface of the channel but the other methods used ADV data. In other words, ADV has instrumentation limitations because it can not touch the bed of the channel.
- The shear stress from the Reynolds shear stress extrapolation showed the best agreement with the shear stress from the Preston tube because Reynolds shear stress extrapolation considers the limitation of instrumentation using ADV by extrapolating shear stress.
- This study obtained equations to estimate K_b value (the ratio of maximum shear stress to averaged shear stress) in meandering channels by using the Preston tube and the Reynolds shear stress extrapolation. The equations derived are: 1) the best fit equation by taking regression of K_b points from previous studies (Ippen and Drinker (1962), USBR (1964) and Yen (1965)) and this study; and 2) an upper envelope equation that was obtained from the maximum values of K_b. The K_b values from the upper envelope curve using the Preston tube were 27% higher in average than the K_b values from

the best fit curve. Also, the K_b values from the upper envelope curve using the Reynolds shear stress extrapolation was 28% higher in average than the K_b values from the best fit curve. Therefore, it was concluded that the effect of enveloping in both methods were similar.

- In design situations, the upper envelope equation from the Preston tube is recommended for design because the upper envelope equation from Preston tube considers the worst case scenario. The best fit and upper envelope equation for K_b value from the Preston tube is presented in Equation 5.1 and Equation 5.2 respectively.

$$K_b = 2.4992 \times \left(\frac{R_c}{T_w} \right)^{-0.321}$$ **Equation 5.1**

$$K_b = 3.2135 \times \left(\frac{R_c}{T_w} \right)^{-0.2657}$$ **Equation 5.2**

Where, K_b = ratio of maximum shear stress and averaged shear stress from HEC-RAS modeling (dimensionless);

R_c = radius of curvature of meandering channel (L); and

T_w = top width of channel (L).

- The upper envelope curve for the K_b value from the Preston tube showed that previous studies (Ippen and Drinker (1962), USBR (1964) and Yen (1965)) were underestimated by 46% when the ratio of radius of curvature and top width of channel was greater than 4. Therefore, cautious observation of the K_b value from the Preston tube is necessary for application of the upper envelope curve of K_b in real world situation.

- Due to the limitation of range of data points, it is recommended that use K_b chart presented in Figure 4.21 when the ratio of radius of curvature and top width of channel ranged between 1 and 7.

5.3 Recommendations for Future Research

During the physical modeling study, model construction, data collection and experimental data analysis were conducted. The shear stress distribution was calculated and plotted by selecting four different ways. For future research, several recommendations are provided;

- It is recommended to investigate shear stress distribution in case of native topography geometry by using the same methods of this study that are applicable to hydraulic design in the real world.
- The number of data points (seven or eight) that were collected by the ADV in the velocity profile was not good enough to obtain an accurate result from a linear regression of the flow velocity profile. To increase the accuracy of the linear regression, the number of data points collected should be at least fifteen for a reasonable linear regression (about twice of current number of data points).

5.4 Limitations of this Study

This experimental study introduced four different methods to calculate shear stress in a bend. Also, the study obtained equations to estimate how much shear stress in a bend is higher than in a straight channel, but this study is limited in the following points;

- This study was based on the laboratory data only from four discharges; 8, 12, 16 and 20 cfs.
- In the low flow rate case (8 and 12 cfs), data collection was limited because the ADV could not be submerged in the water due to low water surface elevation.

6 References

Afzalimehr, H and Anctil, F. (2000) Accelerating shear velocity in gravel-bed channels. Hydrological Sciences-Journal-des Sciences Hydrologiques, 45(1) February 2000 p113-124

Baird, D.C. (2004) Turbulent and Suspended Sediment Transport in a Mobile, Sand Bed Channel With Riprap Side Slopes. Ph.D Dissertation The University of New Mexico Albuquerque, New Mexico, NM.

Bagnold, R.A. (1960) Some Aspects of the Shape of River Meanders. *United States Geological Survey Professional Paper* 282E, 135-44.

Clauser, F. (1956). The Turbulent Boundary Layer". Adv. Appl. Mech. Vol. 4, p1-51.

Darrow, J. (2004). Effects of Bendway Weir Characteristics on Resulting Flow Conditions. M.S. Thesis, Colorado State University, Department of Civil Engineering, Fort Collins, CO.

Federal Highway Administration (FHWA) (2005). Design of Roadside Channels With Flexible Linings. Report No. FHWA-NHI-05-114.

Federal Highway Administration (FHWA) (2001). River Engineering for Highway Encroachments. Report No. FHWA NHI 01-004 HDS 6.

FISRWG (Federal Interagency Stream Restoration Working Group) (1998). Stream Corridor Restoration, Principles, Processes, and Practice.

Heintz, M.L. (2002). Investigation of Bendway Weir Spacing. M.S. Thesis, Colorado State University, Department of Civil Engineering, Fort Collins, CO.

Hickin, E.J. and Nanson, G.C. (1975) The Character of Channel Migration on the Beatton River, North-East British Columbia, Canada. *Bulletin of the Geological Society of America* 86, 487-94.

Hickin, E.J. and Nanson, G.C. (1986) A statistical examination of bank erosion and channel migration in western Canada. *Bulletin of the Geological Society of America* 97, 497-504.

Ippen, A.T. and Drinker, P.A. (1962) Boundary Shear Stresses in Curved Trapezoidal Channels. *ASCE Journal of the Hydraulics Division*, September, 143-175.

Julien, P.Y. (1998). Erosion and Sedimentation. Cambridge University Press, New York, NY.

Julien, P.Y. (2002). River Mechanics. Cambridge University Press, New York, NY.

Keller, E.A (1971). Areal Sorting of Bed Load Material: the Hypothesis of Velocity Reversal. *Bulletin of the Geological Society of America* 82, 753-6

Keller, E.A (1972). Development of Alluvial Stream Channels: A Five-Stage Model. *Bulletin of the Geological Society of America* 83, 1531-6

Knighton, D.A. (1998). Fluvial Forms and Processes. Oxford Press, (Published under license from Arnold Publishing, London), New York, NY.

Lane, E.W. (1955). Design of Stable Channels. *ASCE Trans.*, 120 (Paper No. 2776): 1234-1260.

Montes, S. (1998), Hydraulics of Open Channel Flow. ASCE Press, Reston, MA

Muste, M., and Patel, V.C., (1997). Velocity Profiles for Particles and Liquid in Open-Channel Flow with Suspended Sediment. Journal of Hydraulic Engineering., ASCE Vol, 123, No.(9), p.742-751.

Nikora, V., and Gohring, D., (2000) "Flow Turbulence over Fixed and Weakly Mobile Gravel Beds" Journal of Hydraulic Engineering., ASCE Vol, 126(9), p.679-690.

Odgaard, A.J (1986) Meander Flow Model. I: Development. *ASCE Journal of the Hydraulics Engineering*, December, 1117-1134.

Preston, J. H. (1954) "The Determination of Turbulent Skin Friction by Means of Pitot Tubes." *Journal of the Toyal Aeronautical Society*, Vol. 58: 109-121.

Raupach, M.R (1991), "Saltation Layers, Vegetation Canopies and Roughness lengths." Acta Mechanica, 1, p83-96. From Nikora and Gohring (2000).

Rosgen, D. (1996). Applied River Morphology. Printed Media Companies, Minneapolis, MN.

Rozovskii, I.L. (1961). Flow of Water in Bends of Open Channels. Academy of Sciences of the Ukrainian SSR

Schmidt P.G (2005). Effects of Bendway Weir Field Geometric Characteristics on Channel Flow Conditions. M.S. Thesis, Colorado State University, Department of Civil Engineering, Fort Collins, CO

Schlicting H. (1987). Boundary Layer Theory (7th Edition) McGraw-Hill: New York

Sclafani, P. (2008) Preston Tube Calibration. Open File Report Colorado State University Engineering Research Center Fort Collins, Colorado

Sear, D.A. (1996) Sediment Transport in Pool-Riffle Sequences. *Earth Surface Processes and Landforms* 21, 241-62.

Sear, D.A., Newson, M.D. and Brookes, A. (1995) Sediment-Related River Maintenance: The Rule of Fluvial Geomorphology. *Earth Surface Processes and Landforms* 20, 629-47.

Smart, G.M. (1999), "Turbulent Velocity Profiles and Boundary Shear in Gravel Bed Rivers" Journal of Hydraulic Engineering., ASCE Vol, 125(2), p.106-116.

Stephens, A. V. and Haslam, J. A.G. (1938) Flight Experiments on Boundary Layer Transition in Relation to Profile Drag. R.& M. 1800. August 1938

United Stated Bureau of Reclamation (1964). Progress Report I Boundary Shear Distribution around a Curve in a Laboratory Canal. Report No. Hyd-526, June.

Wahl, T.L (1996) User's Manual of WinADV. Bureau of Reclamation's Water Resources Research Laboratory

Wahl, T.L (2000) Analyzing ADV Data Using WinADV. 2000 Joint Conference on Water Resources Engineering and Water Resources Planning & Management July 30-August 2, 2000 – Minneapolis, Minnesota.

Watson, C.C., Biedenharn, D.S., Thorne, C.R. (2005). Stream Rehabilitation. Cottonwood Research, Fort Collins, CO USA.

Yen, B.C. (1965) Characteristics of Subcritical Flow in a Meandering Channel. Ph.D Dissertation, University of Iowa, Department of Mechanics and Hydraulics, Iowa City, Iowa, June.

Appendix A. Model Description

A.1 Introduction

In order to facilitate analysis of shear stress distribution in a meandering channel, physical modeling was conducted at the Colorado State University Engineering Research Center. In this chapter, the geometry of the model, construction procedure and methods of measurements will be introduced.

A.2 Model Description

The physical model is an undistorted, 1:12 Froude scale model. The boundary of the channel is prismatic. That means the geometry of the channel is constant. The composition of the physical model is; two kinds of bends and one transitional area between two bends. A data collection cart was mounted on the top of the physical model with a point gage for the measurement of three dimensional flow velocity (V_x, V_y and V_z), flow depth (h) and boundary shear stress (τ) (Heintz 2002). Figure A.1 presents the schematic view of the physical model.

Figure A.1 Schematic View of the Physical Model

A.2.1 Model Geometry

It is impossible to construct a physical model that describes the whole of the study reach because study reach length of the prototype is 29 miles. Therefore, a representative section of the reach was selected to describe the flow in a meandering channel (Heintz 2002). The data of the reach geometry were obtained by using 1992 aerial photographs (Heintz 2002). The measured parameters of the study reach were; top width, radius of curvature, the length of the bend, relative curvature and the rotation angle of the bend. Table A.1 shows the geometry of the prototype. In addition, Table A.2 provides the information of the physical model geometry. Figure A.2 describes the geometry measurement results of the study reach. To maintain the 1:12 Froude scale, type 1 and type 3 bend were selected for the physical model (Heintz 2002).

Table A.1 The Geometry of the Prototype of Study Reach (from Heintz 2002)

Type	Top Width	Radius of Curvature	Bend Angle	Relative Curvature	Channel Length
	ft (m)	ft (m)	degrees	r/b	ft (m)
1	230.4 (70.2)	465 (141.73)	125	2.02	1014 (309)
3	180 (54.86)	789.96 (240.77)	73	4.39	1002 (305)

Table A.2 The Geometry Information of the Physical Model (from Heintz 2002)

Type	Top Width	Radius of Curvature	Bend Angle	Relative Curvature	Channel Length
	ft (m)	ft (m)	(degrees)	r/b	ft (m)
1	19.2 (5.9)	38.75 (11.81)	125	2.02	84.5 (25.8)
3	15 (4.6)	65.83 (20.06)	73	4.39	83.5 (25.5)

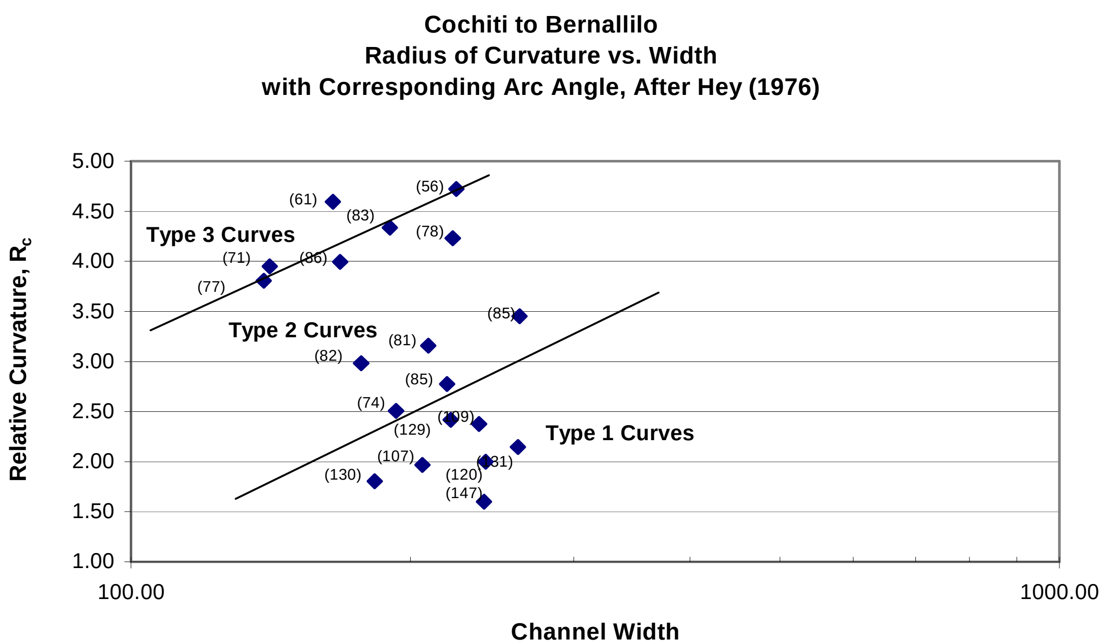

Figure A.2 The Type of the Bend of the Study Reach (from Heintz 2002)

The shape of the model is trapezoidal and the side slope of the channel is 1:3 (Vertical: Horizontal). The channel depth of 1.5ft (0.46m) was selected to satisfy the flow rate of the data collection (Heintz 2002). The bed slope of the model, 0.000863, was close enough as measured in the prototype reach. A straight transition area 10:1

for the smooth connection between upper bend and lower bend was installed (Heintz 2002). Figure A.3 provides the sketch of the physical model.

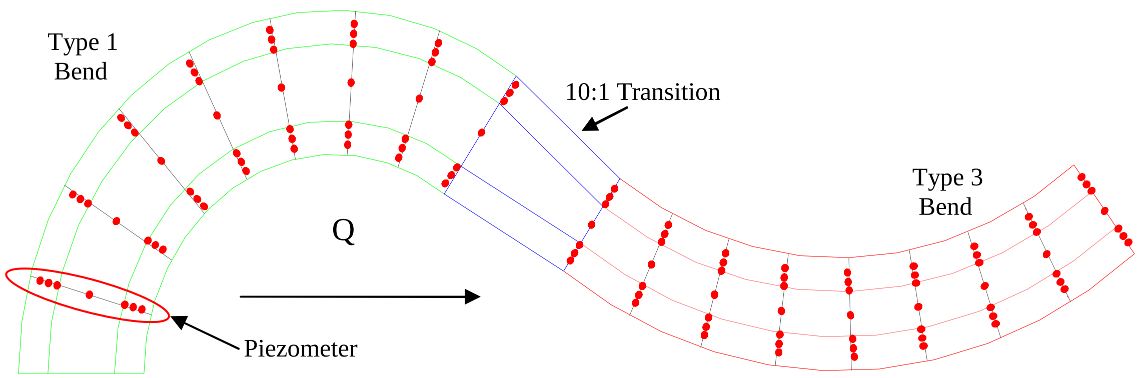

Figure A.3 Sketch of the Main Channel

A.2.2 Model Construction

Model construction began in early August 2000. About 8 months were spent on the construction. During the construction project, the headbox, main channel and tailbox were constructed. Figure A.4 illustrates the schematic sketch of Hydromachinery Laboratory. In the end of the physical model, the tailbox was constructed for energy dissipation and consistent flow conditions. The components of the headbox are; pipe manifold, a rock baffle and side and bed transitional boundaries (Heintz 2002).

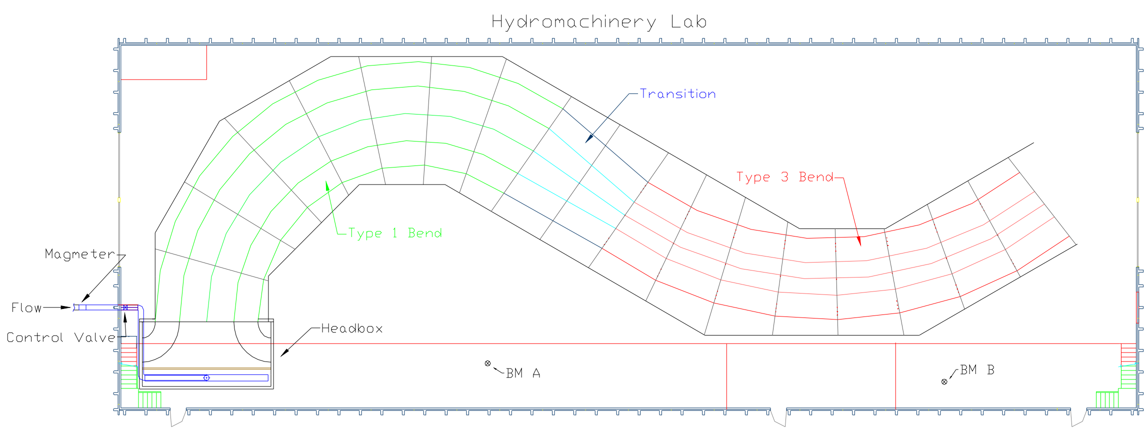

Figure A.4 Schematic Sketch of Hydromachinery Laboratory

The source of water used for the experiment is Horsetooth Reservoir (Heintz 2002). A 12 inch pipe line is directly connected to the headbox of the model from the reservoir (Heintz 2002). For energy dissipation and flow condition maintenance, a rock baffle was installed in the headbox. The averaged size of the rock is 2 inches. In addition, 4 ft high walls are located in the floor of the laboratory for reinforcement of the model security (Heintz 2002). Figure A.5 shows the walls of the model. To construct rigid channel geometry, a plywood skeleton was used in each cross section.

The plywood skeleton of the model placed eight pieces in the upstream bend and the other eight pieces located in the downstream bend. For the construction of the main channel, sand was filled, saturated, compacted and leveled for the construction of the main channel (Heintz 2002). Figure A.6 and Figure A.7 show the sand filling and leveling for main channel construction.

Figure A.5 4 ft High Walls of the Model

Figure A.6 Skeleton of the Main Channel and Filling Material of Main Channel

Figure A.7 Leveling of Fill Sand of the Main Channel

To maintain a rigid geometry in the bend, the cross section skeletons were connected to each other with 4 inch by 1/8th inch steel flashing (Heintz 2002). The flash was installed at each top bank point and channel toe in each cross section (Heintz 2002). Figure A.8 shows the installation of the steel flashing. After the completion of steel flashing and welding, a 2 inch thick concrete cap was placed over the top of the finished sand to reinforce the strength of the channel geometry. The next procedure of model construction was concrete placement. About 40 cubic yards of concrete and 600 tons of sand were used for the model construction. To obtain the roughness of the channel, a broom finish of concrete was applied. In addition, water sealant was sprayed on the main channel to prevent leaking. Figure A.9 and Figure A.10 present concrete placement and broom finish for desired channel roughness.

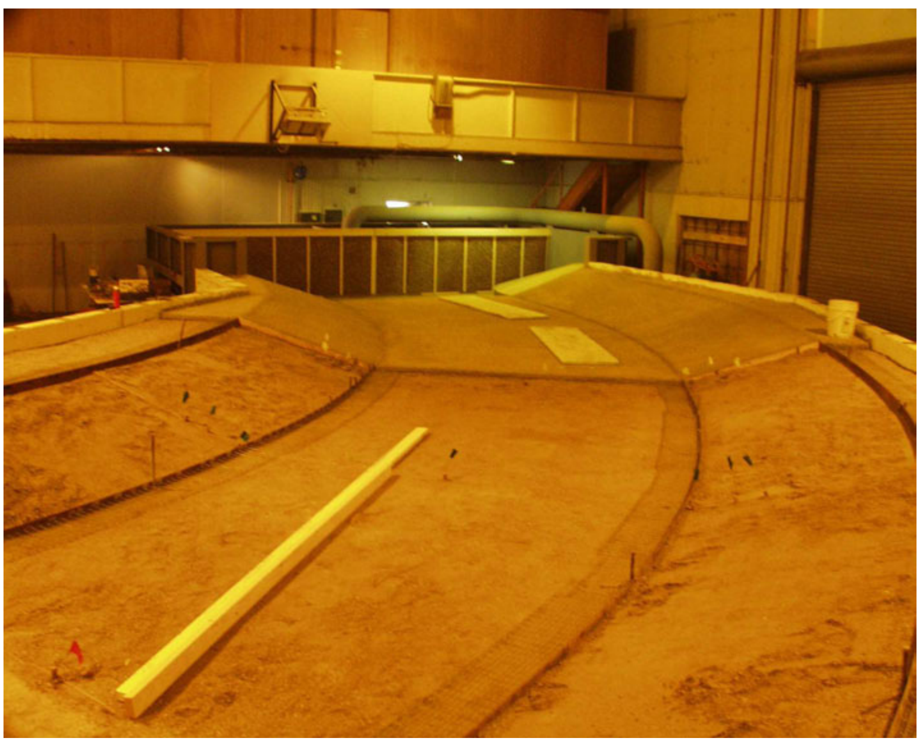

Figure A.8 Installation of Steel Flashing

Figure A.9 Concrete Placement for Model Construction

Figure A.10 Concrete Broom Finish for Desired Channel Roughness

In the downstream end of the model, a stop log was installed to develop backwater to generate the proper relationship between discharge and stage. Also, a 10 inch pipe and two 12 inch culverts were installed in tailbox to convey water flow to College Lake (Heintz 2002).

A.3 Instrumentation

The physical model was constructed for the measurements of flow velocity, flow depth, flow rate and shear stress. Data collection facilities were placed on the cart that was installed above the main channel. In this section, the procedure and method of data collection will be introduced.

A.3.1 Flow Rate Measurement

For the measurement of the flow rate, a Georg Fischer® SIGNET 2550 Insertion Magmeter with an accuracy of ±2% was used. The water source is Horsetooth Reservoir. The pipeline that connects Horsetooth Reservoir and the model is 12 inches and the material of the pipe is PVC (Polyvinyl Chloride). Figure A.11 shows the photographs of the flow meter.

Figure A.11 SIGNET Meters and Electronic Display Boxes (from Kinzli, 2005)

A.3.2 Flow Depth Measurement

Two methods of flow depth measurement were used in the procedure of data collection. The first method is point gauge measurement that was presented in Figure A.12. For this method, a point gauge was installed on the data collection cart.

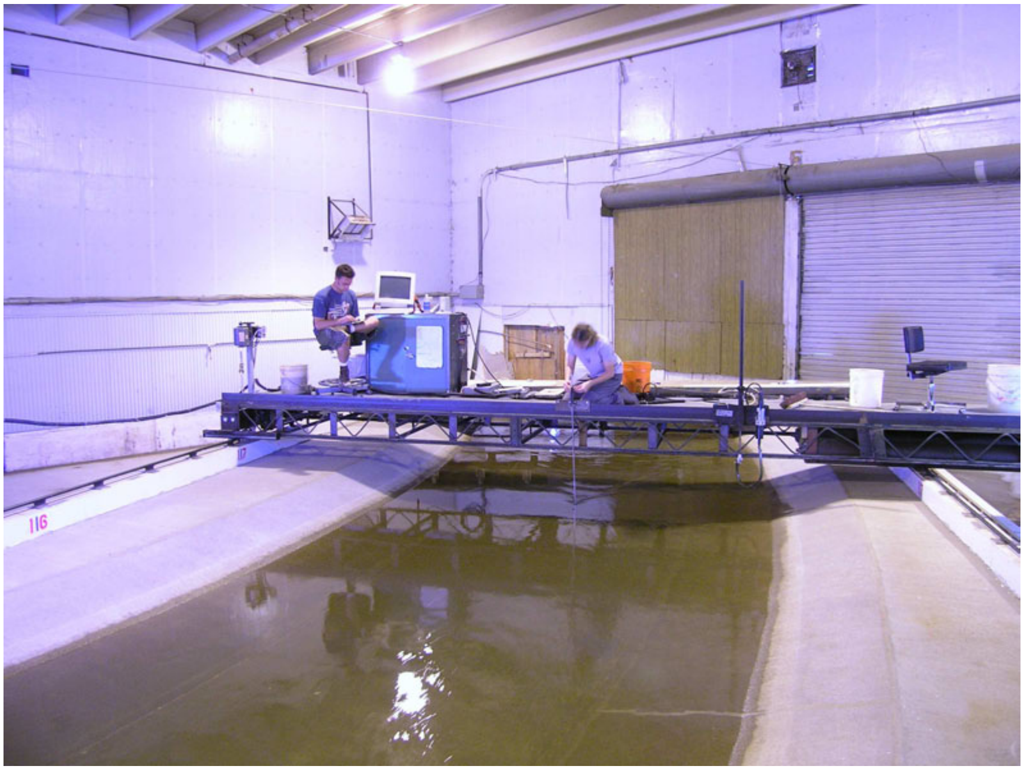

Figure A.12 Point Gauge Installation for Flow Depth Measurement

In addition to the point gage, piezometer taps were installed throughout the model. During the main channel construction procedure, a piezometer was placed at the skeleton of main channel. In each cross section, 7 piezo meters were installed. In total, 122 piezometers installed for data collection. The label in each piezometer was assigned a through g from left to right. Figure A.13 shows the sketch of the piezometer used. In addition, Figure A.14 shows the installation of the piezometers.

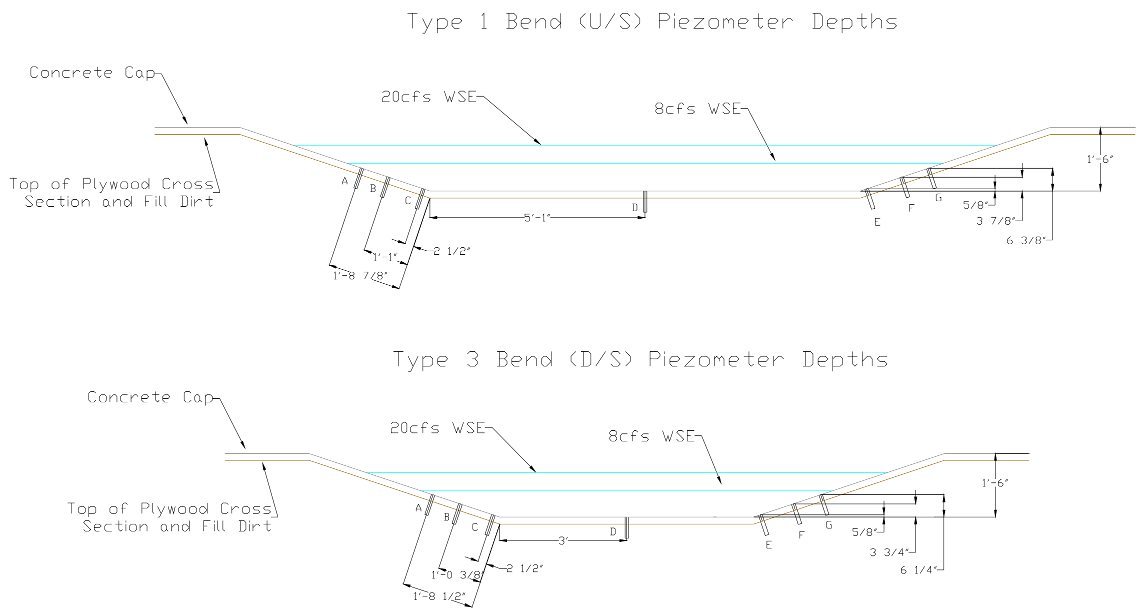

Figure A.13 The Location of Piezometer Type 1 and Type 3 Bend (from Heintz, 2002)

Figure A.14 Installation of Piezometer for Flow Depth Measurement

The piezometers installed in the main channel are connected with a stilling well to allow data collection of water surface elevation (Heintz 2002). 2 inch diameter PVC pipe was placed in the stilling well. All piezometer taps were equipped with a back-flushing system to ensure that the stilling wells and the connecting tubing and taps would not clog (Heintz 2002). Figure A.15 shows the stilling wells used for water surface elevation measurement. The bed elevation of the channel also was measured using a point gauge. Flow depth was calculated by subtracting the bed elevation from water surface elevation.

Figure A.15 Stilling wells for water surface elevation measurement

A.3.3 Velocity Measurement

Since 1993, the ADV has been a popular instrument to collect flow data in field and laboratory studies (Wahl 2000). The installation of the ADV allowed for the measurement of flow velocity in each cross section of the model. The data of an

ADV is three- dimensional velocity measurements that were composed with V_x, V_y and V_z. The ADV measured velocity from a sampling volume located 0.164 ft (5 cm) below the probe head. The sampling rate of the ADV is 10 Hz. The time period of data collection in each point is approximately 30 seconds. In each point, 300 measurements of flow velocity data were collected. The three-dimensional velocity measurements were collected with the probe of the ADV directed perpendicular to the cart, which was always oriented perpendicular to direction of the flow (Heintz 2002). Figure A.16 presents the photograph of ADV. Also, Figure A.17 shows ADV installation in the data collection cart. After data collection by ADV, data processing is necessary because it is impossible to perform data analysis with the original ADV file. As a result, computer software, WinADV was developed by Wahl (2000). The initial purpose of the software development was to provide the method of displaying the velocity time series (Wahl 2000).

Figure A.16 Photograph of ADV (from Heintz 2002)

Figure A.17 Installation of ADV in Data Collection Cart

A.3.4 Shear Stress Measurement

Sclafani (2008) performed shear stress data calibration in a 60-foot long, 4-foot wide, 2.5-foot tall flume. To collect data for the calculation of shear stress on the bed and bank of the channel, a Preston tube was used. The Preston tube presented in Figure A.18 allows for measuring boundary shear stress of the model. The Preston tube technique utilizes a modified pitot tube that is placed directly on the bed of the channel at the point of measurement. A pressure transducer was used for the collection of pressure data.

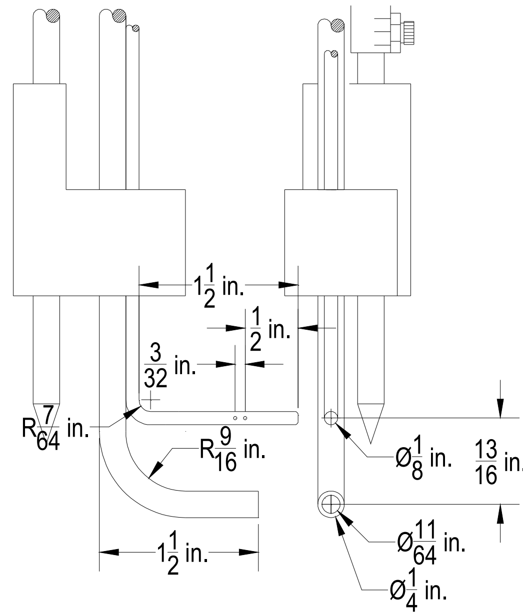

Figure A.18 Preston Tube for Shear Stress Measurement (from Sclafani (2008))

A.4 Model Calibration

There are two kinds of calibration of the model; the first one is channel roughness calibration. Heintz (2002) conducted the model calibration by using the HEC-RAS program. As a result of the roughness calibration, the value of Manning's n, the roughness value was determined to be 0.018. The second calibration of the model is backwater calibration by installing stop logs in the tailbox of the model. Using the computed roughness value of 0.018, the HEC-RAS model was then used to calculate a water surface profile for normal depth conditions at all flow rates (Heintz 2002). For the confirmation of the model calibration, Heintz (2002) compared the measured value of water surface profile and calculated value of water surface profile by using HEC-RAS. Figure A.19 and Figure A.20 show the installed stop logs of the model.

Figure A.19 Stop Log Installation of the Model

Figure A.20 Stop Log for Calibration of the Model

A.5 Test Program (Test Matrix)

There are four different discharge cases (8, 12, 16 and 20 cfs), 18 cross sections and 7 piezometers (a through g) in each cross section. Figure A.21 shows a test matrix for the case of baseline test condition. In case of the discharge of 8 cfs and 12 cfs, several piezometers are not submerged due to the low flow depth. Therefore, data of piezometer a, b, f and g for 8 cfs, are excluded from test matrix. Also, piezometer a and g for 12 cfs could not collected data due to the same situation of 8 cfs.

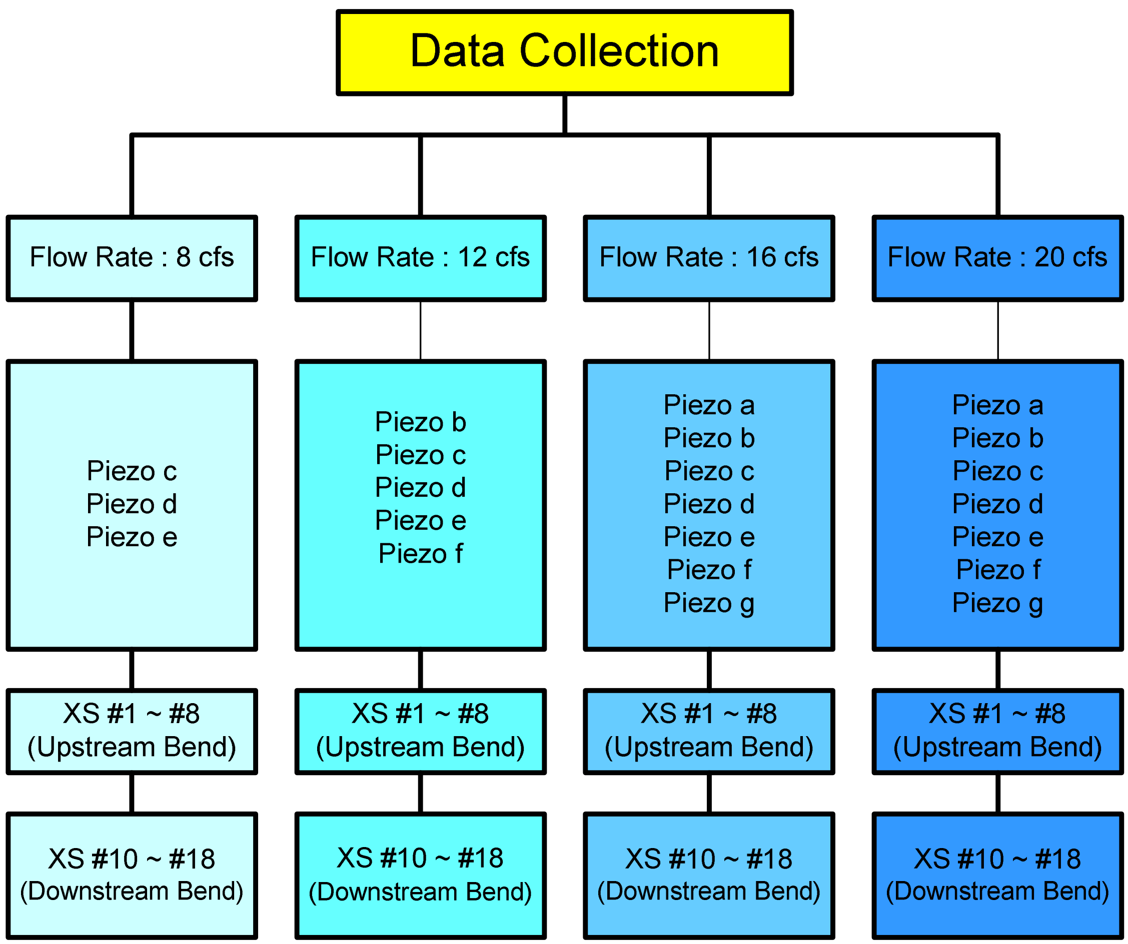

Figure A.21 Test Program of Baseline Condition

Appendix B. Preston Tube Calibration

Table B.1 Shear Stress from Preston Tube Calibration for 8 cfs

XSEC	Piezo	Shear Stress (psf)
4	c	0.0178
4	d	0.0166
4	e	0.0164
5	c	0.0183
5	d	0.0177
5	e	0.0000
6	c	0.0178
6	d	0.0189
6	e	0.0147
7	c	0.0172
7	d	0.0148
7	e	0.0125
8	c	0.0203
8	d	0.0160
8	e	0.0130
10	c	0.0438
10	d	0.0363
10	e	0.0322
11	c	0.0240
11	d	0.0384
11	e	0.0193
12	c	0.0342
12	d	0.0400
12	e	0.0289
13	c	0.0393
13	d	0.0361
13	e	0.0313
14	c	0.0263
14	d	0.0390
14	e	0.0346
15	c	0.0287
15	d	0.0484
15	e	0.0411
16	c	0.0286
16	d	0.0350
16	e	0.0376
17	c	0.0328
17	d	0.0388
17	e	0.0460

Table B.2 Shear Stress from Preston Tube Calibration for 12 cfs

XSEC	Piezo	Shear Stress (psf)	XSEC	Piezo	Shear Stress (psf)
4	b	0.0239	14	b	0.0230
4	c	0.0211	14	c	0.0361
4	d	0.0223	14	d	0.0490
4	e	0.0248	14	e	0.0395
4	f	0.0175	14	f	0.0303
5	b	0.0273	15	b	0.0266
5	c	0.0267	15	c	0.0367
5	d	0.0244	15	d	0.0498
5	e	0.0246	15	e	0.0454
5	f	0.0175	15	f	0.0390
6	b	0.0227	16	b	0.0287
6	c	0.0238	16	c	0.0385
6	d	0.0209	16	d	0.0471
6	e	0.0210	16	e	0.0481
6	f	0.0172	16	f	0.0498
7	b	0.0250	17	b	0.0224
7	c	0.0205	17	c	0.0321
7	d	0.0185	17	d	0.0457
7	e	0.0152	17	e	0.0539
7	f	0.0148	17	f	0.0453
8	b	0.0274			
8	c	0.0241			
8	d	0.0170			
8	e	0.0186			
8	f	0.0143			
10	b	0.0556			
10	c	0.0555			
10	d	0.0396			
10	e	0.0320			
10	f	0.0323			
11	b	0.0352			
11	c	0.0343			
11	d	0.0452			
11	e	0.0264			
11	f	0.0192			
12	b	0.0337			
12	c	0.0496			
12	d	0.0389			
12	e	0.0334			
12	f	0.0287			
13	b	0.0307			
13	c	0.0457			
13	d	0.0430			
13	e	0.0338			
13	f	0.0313			

Table B.3 Shear Stress from Preston Tube Calibration for 16 cfs

XSEC	Piezo	Shear Stress (psf)	XSEC	Piezo	Shear Stress (psf)
4	a	0.0299	11	d	0.0617
4	b	0.0266	11	e	0.0331
4	c	0.0258	11	f	0.0297
4	d	0.0260	11	g	0.0271
4	e	0.0285	12	a	0.0429
4	f	0.0234	12	b	0.0483
4	g	0.0165	12	c	0.0568
5	a	0.0335	12	d	0.0579
5	b	0.0343	12	e	0.0444
5	c	0.0261	12	f	0.0455
5	d	0.0271	12	g	0.0380
5	e	0.0289	13	a	0.0075
5	f	0.0251	13	b	0.0494
5	g	0.0185	13	c	0.0555
6	a	0.0311	13	d	0.0487
6	b	0.0346	13	e	0.0429
6	c	0.0270	13	f	0.0415
6	d	0.0283	13	g	0.0397
6	e	0.0280	14	a	0.0129
6	f	0.0238	14	b	0.0232
6	g	0.0198	14	c	0.0417
7	a	0.0321	14	d	0.0469
7	b	0.0290	14	e	0.0317
7	c	0.0259	14	f	0.0249
7	d	0.0285	14	g	0.0256
7	e	0.0251	15	a	0.0174
7	f	0.0219	15	b	0.0248
7	g	0.0162	15	c	0.0397
8	a	0.0243	15	d	0.0488
8	b	0.0278	15	e	0.0476
8	c	0.0293	15	f	0.0377
8	d	0.0280	15	g	0.0361
8	e	0.0259	16	a	0.0142
8	f	0.0188	16	b	0.0263
8	g	0.0158	16	c	0.0375
10	a	0.0678	16	d	0.0488
10	b	0.0630	16	e	0.0551
10	c	0.0700	16	f	0.0472
10	d	0.0445	16	g	0.0351
10	e	0.0428	17	a	0.0160
10	f	0.0408	17	b	0.0264
10	g	0.0395	17	c	0.0283
11	a	0.0454	17	d	0.0455
11	b	0.0543	17	e	0.0722
11	c	0.0691	17	f	0.0599
			17	g	0.0490

Table B.4 Shear Stress from Preston Tube Calibration for 20 cfs

XSEC	Piezo	Shear Stress (psf)	XSEC	Piezo	Shear Stress (psf)
4	a	0.0240	11	d	0.0505
4	b	0.0213	11	e	0.0213
4	c	0.0170	11	f	0.0209
4	d	0.0210	11	g	0.0249
4	e	0.0268	12	a	0.0262
4	f	0.0198	12	b	0.0397
4	g	0.0151	12	c	0.0455
5	a	0.0299	12	d	0.0461
5	b	0.0265	12	e	0.0366
5	c	0.0194	12	f	0.0333
5	d	0.0192	12	g	0.0336
5	e	0.0252	13	a	0.0230
5	f	0.0197	13	b	0.0337
5	g	0.0150	13	c	0.0515
6	a	0.0265	13	d	0.0426
6	b	0.0273	13	e	0.0294
6	c	0.0196	13	f	0.0317
6	d	0.0195	13	g	0.0327
6	e	0.0219	14	a	0.0198
6	f	0.0199	14	b	0.0327
6	g	0.0123	14	c	0.0445
7	a	0.0193	14	d	0.0410
7	b	0.0242	14	e	0.0322
7	c	0.0212	14	f	0.0257
7	d	0.0219	14	g	0.0289
7	e	0.0186	15	a	0.0252
7	f	0.0210	15	b	0.0314
7	g	0.0119	15	c	0.0395
8	a	0.0194	15	d	0.0426
8	b	0.0260	15	e	0.0397
8	c	0.0392	15	f	0.0472
8	d	0.0186	15	g	0.0419
8	e	0.0177	16	a	0.0200
8	f	0.0099	16	b	0.0296
8	g	0.0080	16	c	0.0490
10	a	0.0630	16	d	0.0420
10	b	0.0514	16	e	0.0397
10	c	0.0674	16	f	0.0499
10	d	0.0493	16	g	0.0420
10	e	0.0381	17	a	0.0188
10	f	0.0349	17	b	0.0287
10	g	0.0339	17	c	0.0360
11	a	0.0399	17	d	0.0441
11	b	0.0459	17	e	0.0549
11	c	0.0562	17	f	0.0420
			17	g	0.0421

Appendix C. Linear Regression of Flow Velocity Profile

Table C.1 Shear Stress (τ_x) from Linear Regression of Flow Velocity Profile for 8 cfs

XSEC	Piezo	Shear Stress (psf)
4	c	0.0030
	d	0.0018
	e	0.0011
5	c	0.0027
	d	0.0038
	e	0.0009
6	c	0.0034
	d	0.0028
	e	0.0006
7	c	0.0036
	d	0.0045
	e	0.0010
8	c	0.0037
	d	0.0059
	e	0.0000
10	c	0.0063
	d	0.0077
	e	0.0041
11	c	0.0115
	d	0.0081
	e	0.0067
12	c	0.0055
	d	0.0097
	e	0.0041
13	c	0.0044
	d	0.0094
	e	0.0070
14	c	0.0030
	d	0.0043
	e	0.0064
15	c	0.0006
	d	0.0027
	e	0.0049
16	c	0.0007
	d	0.0074
	e	0.0094
17	c	0.0007
	d	0.0057
	e	0.0061

Table C.2 Shear Stress (τ_x) from Linear Regression of Flow Velocity Profile for 12 cfs

XSEC	Piezo	Shear Stress (psf)	XSEC	Piezo	Shear Stress (psf)
4	b	0.0033	14	b	0.0034
4	c	0.0036	14	c	0.0046
4	d	0.0035	14	d	0.0163
4	e	0.0008	14	e	0.0089
4	f	0.0008	14	f	0.0071
5	b	0.0007	15	b	0.0014
5	c	0.0036	15	c	0.0022
5	d	0.0037	15	d	0.0137
5	e	0.0013	15	e	0.0140
5	f	0.0002	15	f	0.0051
6	b	0.0025	16	b	0.0003
6	c	0.0036	16	c	0.0005
6	d	0.0056	16	d	0.0223
6	e	0.0018	16	e	0.0111
6	f	0.0014	16	f	0.0047
7	b	0.0028	17	b	0.0003
7	c	0.0043	17	c	0.0021
7	d	0.0055	17	d	0.0121
7	e	0.0001	17	e	0.0101
7	f	0.0014	17	f	0.0118
8	b	0.0015			
8	c	0.0024			
8	d	0.0042			
8	e	0.0000			
8	f	0.0005			
10	b	0.0081			
10	c	0.0079			
10	d	0.0077			
10	e	0.0017			
10	f	0.0028			
11	b	0.0149			
11	c	0.0195			
11	d	0.0118			
11	e	0.0122			
11	f	0.0013			
12	b	0.0027			
12	c	0.0030			
12	d	0.0132			
12	e	0.0129			
12	f	0.0056			
13	b	0.0043			
13	c	0.0073			
13	d	0.0188			
13	e	0.0168			
13	f	0.0052			

Table C.3 Shear Stress (τ_x) from Linear Regression of Flow Velocity Profile for 16 cfs

XSEC	Piezo	Shear Stress (psf)	XSEC	Piezo	Shear Stress (psf)
4	a	0.0016	11	d	0.0115
4	b	0.0109	11	e	0.0116
4	c	0.0060	11	f	0.0131
4	d	0.0026	11	g	0.0059
4	e	0.0006	12	a	0.0036
4	f	0.0018	12	b	0.0086
4	g	0.0012	12	c	0.0241
5	a	0.0032	12	d	0.0193
5	b	0.0044	12	e	0.0119
5	c	0.0018	12	f	0.0107
5	d	0.0053	12	g	0.0070
5	e	0.0002	13	a	0.0019
5	f	0.0009	13	b	0.0045
5	g	0.0000	13	c	0.0119
6	a	0.0022	13	d	0.0267
6	b	0.0042	13	e	0.0093
6	c	0.0042	13	f	0.0107
6	d	0.0069	13	g	0.0079
6	e	0.0001	14	a	0.0021
6	f	0.0009	14	b	0.0044
6	g	0.0007	14	c	0.0093
7	a	0.0042	14	d	0.0278
7	b	0.0044	14	e	0.0171
7	c	0.0050	14	f	0.0086
7	d	0.0065	14	g	0.0054
7	e	0.0013	15	a	0.0000
7	f	0.0009	15	b	0.0022
7	g	0.0008	15	c	0.0033
8	a	0.0055	15	d	0.0163
8	b	0.0053	15	e	0.0173
8	c	0.0024	15	f	0.0087
8	d	0.0052	15	g	0.0072
8	e	0.0000	16	a	0.0012
8	f	0.0006	16	b	0.0011
8	g	0.0003	16	c	0.0060
10	a	0.0090	16	d	0.0290
10	b	0.0120	16	e	0.0156
10	c	0.0123	16	f	0.0086
10	d	0.0077	16	g	0.0055
10	e	0.0015	17	a	0.0004
10	f	0.0004	17	b	0.0016
10	g	0.0054	17	c	0.0048
11	a	0.0076	17	d	0.0177
11	b	0.0247	17	e	0.0174
11	c	0.0155	17	f	0.0054
			17	g	0.0006

Table C.4 Shear Stress (τ_x) from Linear Regression of Flow Velocity Profile for 20 cfs

XSEC	Piezo	Shear Stress (psf)	XSEC	Piezo	Shear Stress (psf)
4	a	0.0116	11	d	0.0121
4	b	0.0030	11	e	0.0177
4	c	0.0038	11	f	0.0280
4	d	0.0030	11	g	0.0282
4	e	0.0000	12	a	0.0154
4	f	0.0001	12	b	0.0280
4	g	0.0027	12	c	0.0375
5	a	0.0054	12	d	0.0133
5	b	0.0036	12	e	0.0212
5	c	0.0024	12	f	0.0143
5	d	0.0118	12	g	0.0091
5	e	0.0005	13	a	0.0093
5	f	0.0003	13	b	0.0015
5	g	0.0004	13	c	0.0554
6	a	0.0042	13	d	0.0301
6	b	0.0083	13	e	0.0168
6	c	0.0024	13	f	0.0149
6	d	0.0094	13	g	0.0164
6	e	0.0016	14	a	0.0089
6	f	0.0019	14	b	0.0047
6	g	0.0031	14	c	0.0070
7	a	0.0099	14	d	0.0355
7	b	0.0064	14	e	0.0265
7	c	0.0013	14	f	0.0187
7	d	0.0066	14	g	0.0145
7	e	0.0001	15	a	0.0024
7	f	0.0017	15	b	0.0050
7	g	0.0004	15	c	0.0045
8	a	0.0040	15	d	0.0455
8	b	0.0060	15	e	0.0226
8	c	0.0026	15	f	0.0233
8	d	0.0019	15	g	0.0148
8	e	0.0005	16	a	0.0003
8	f	0.0002	16	b	0.0003
8	g	0.0002	16	c	0.0002
10	a	0.0461	16	d	0.0467
10	b	0.0044	16	e	0.0157
10	c	0.0075	16	f	0.0151
10	d	0.0077	16	g	0.0141
10	e	0.0004	17	a	0.0011
10	f	0.0010	17	b	0.0011
10	g	0.0027	17	c	0.0000
11	a	0.0756	17	d	0.0377
11	b	0.0079	17	e	0.0313
11	c	0.0313	17	f	0.0262
			17	g	0.0073

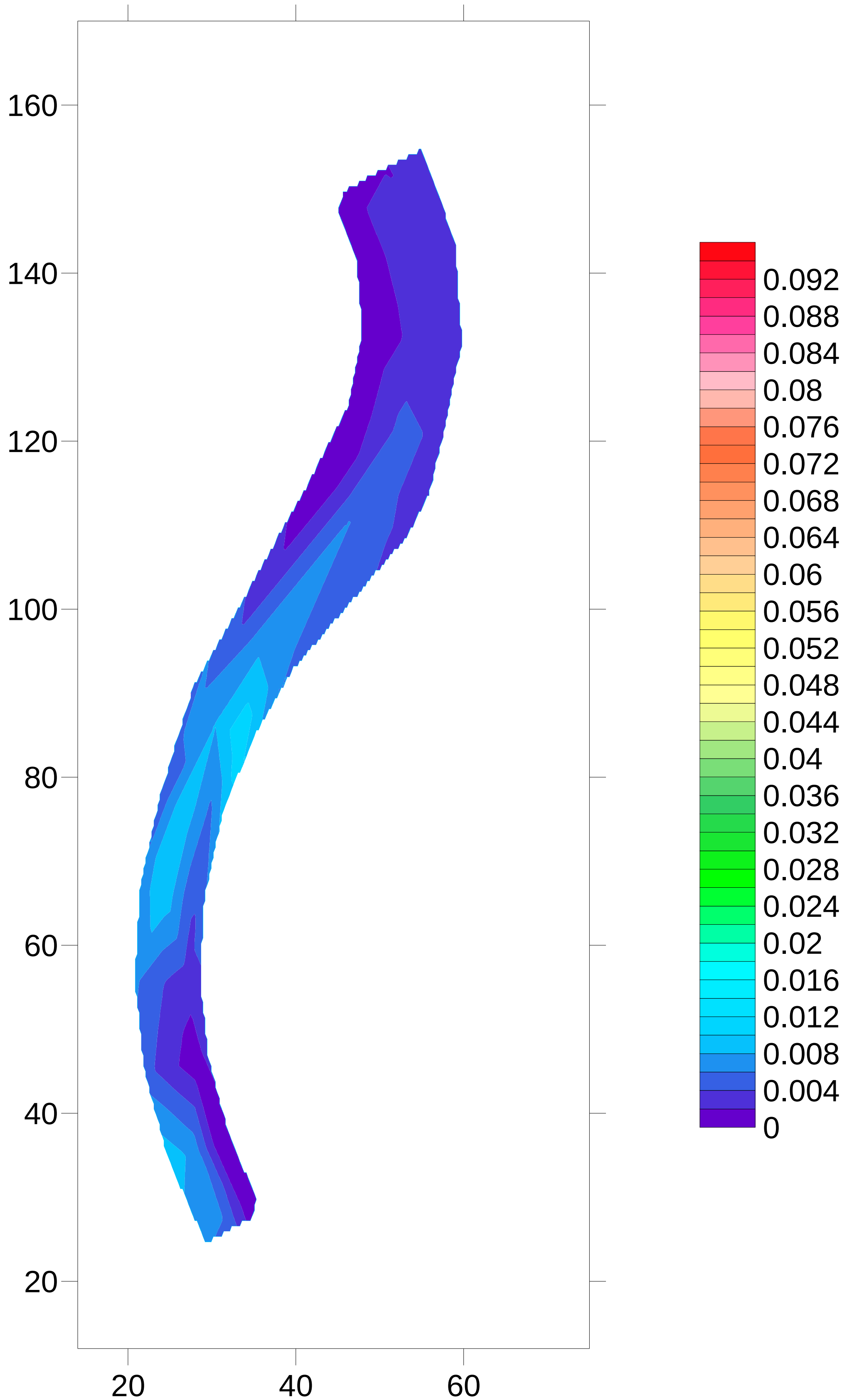

Figure C.1 Shear Stress Distribution τ_x, by Linear Regression for 8 cfs (psf)

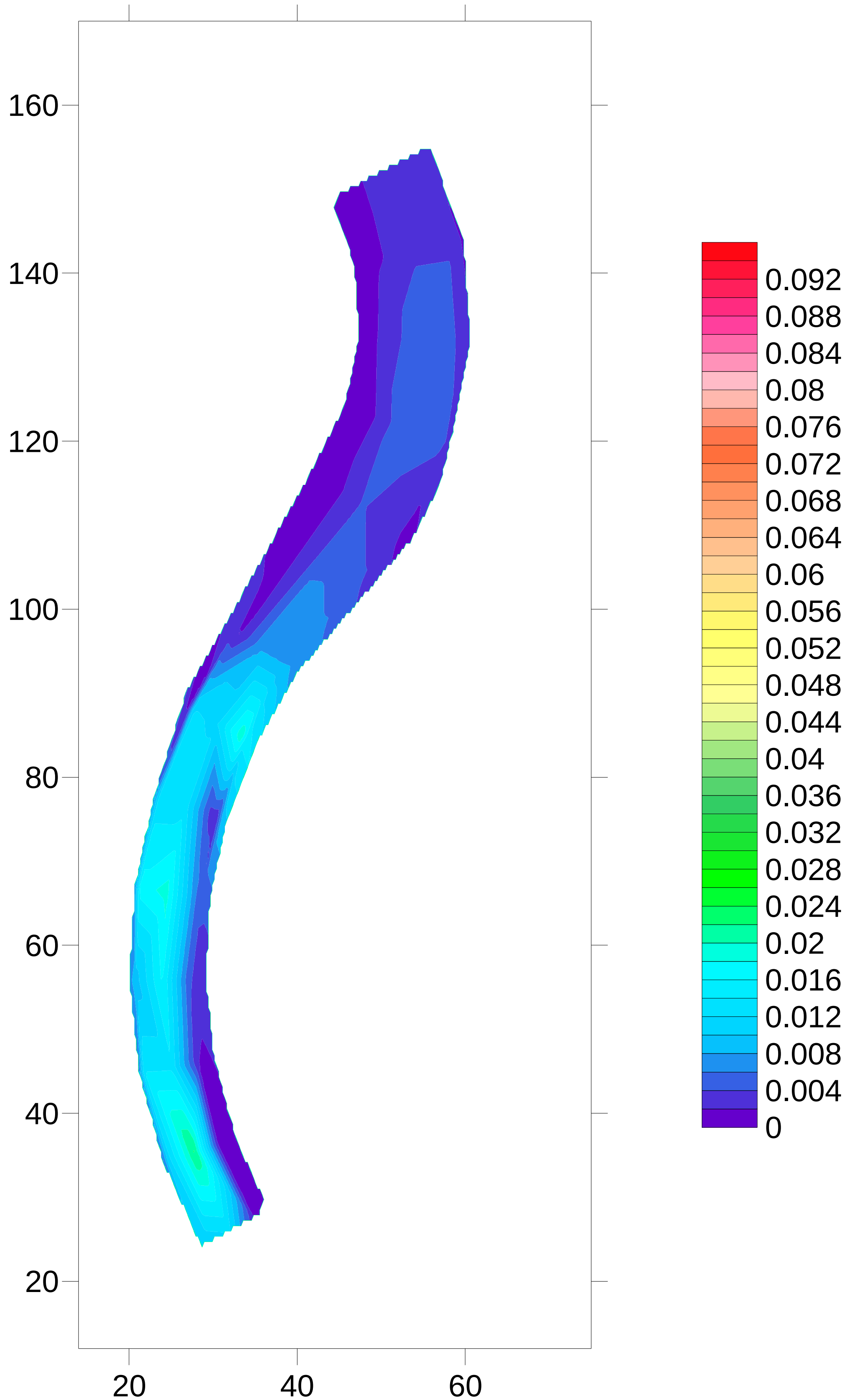

Figure C.2 Shear Stress Distribution τ_x, by Linear Regression for 12 cfs (psf)

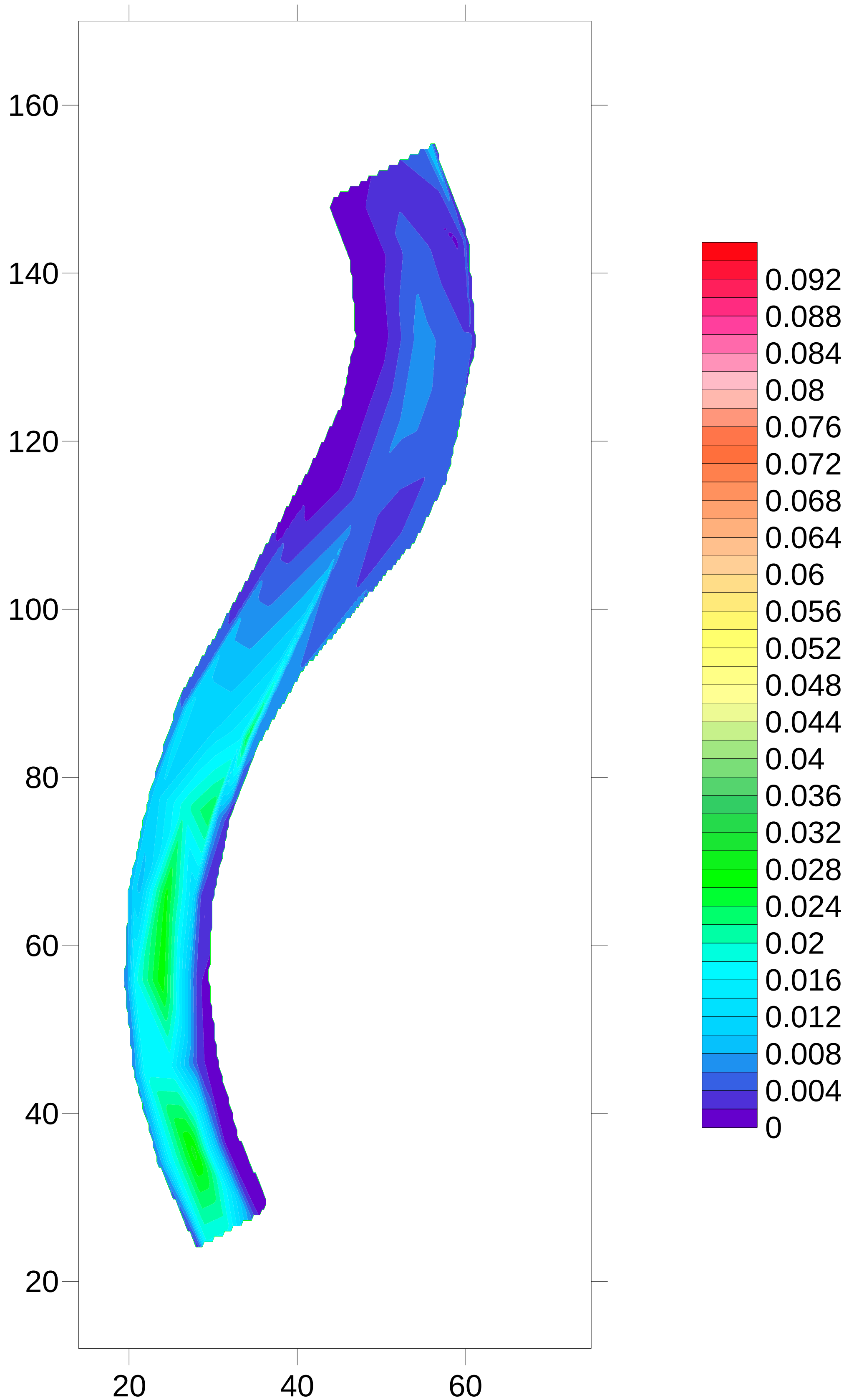

Figure C.3 Shear Stress Distribution, τ_x, by Linear Regression for 16 cfs (psf)

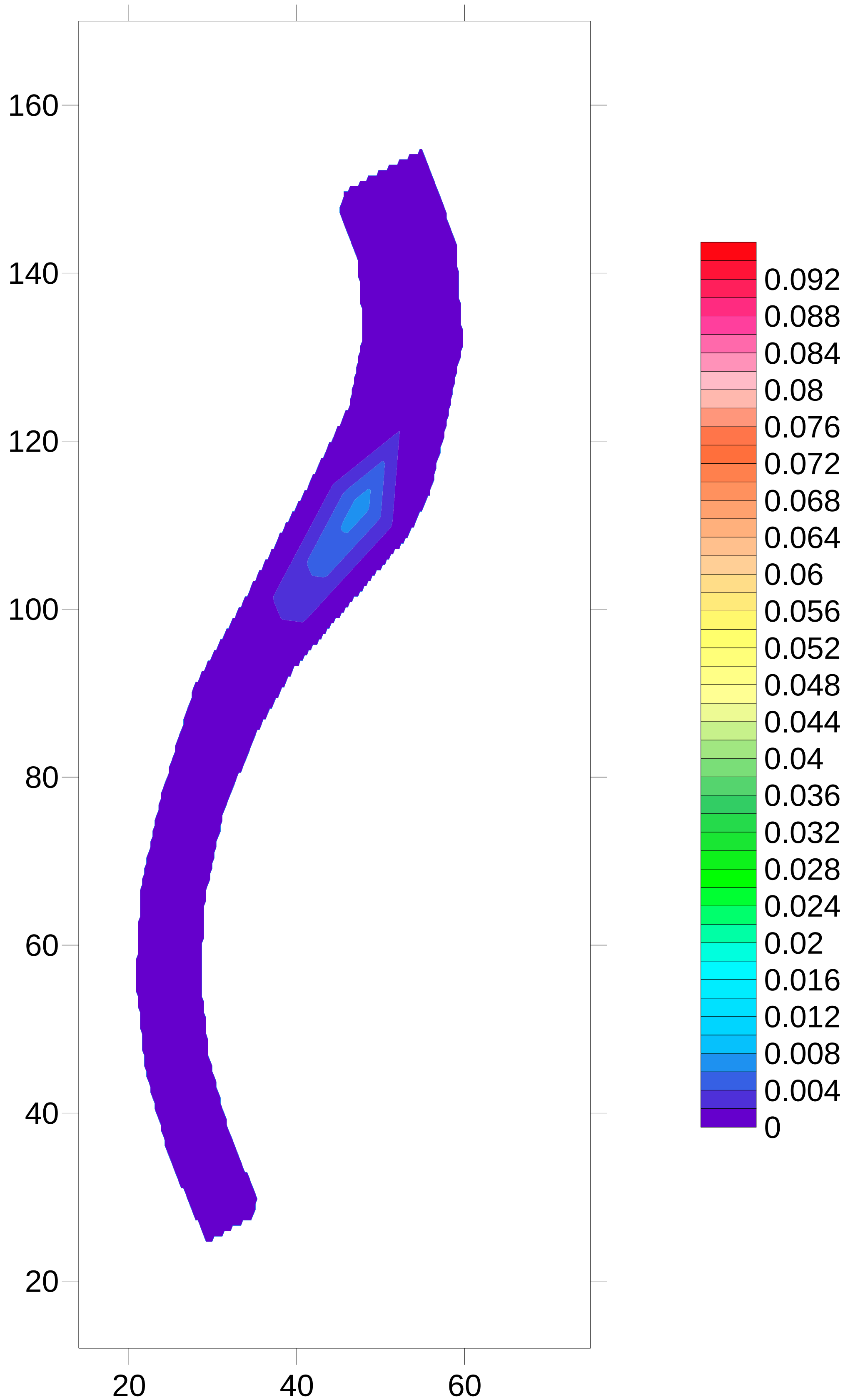

Figure C.4 Shear Stress Distribution, τ_y, by Linear Regression for 8 cfs (psf)

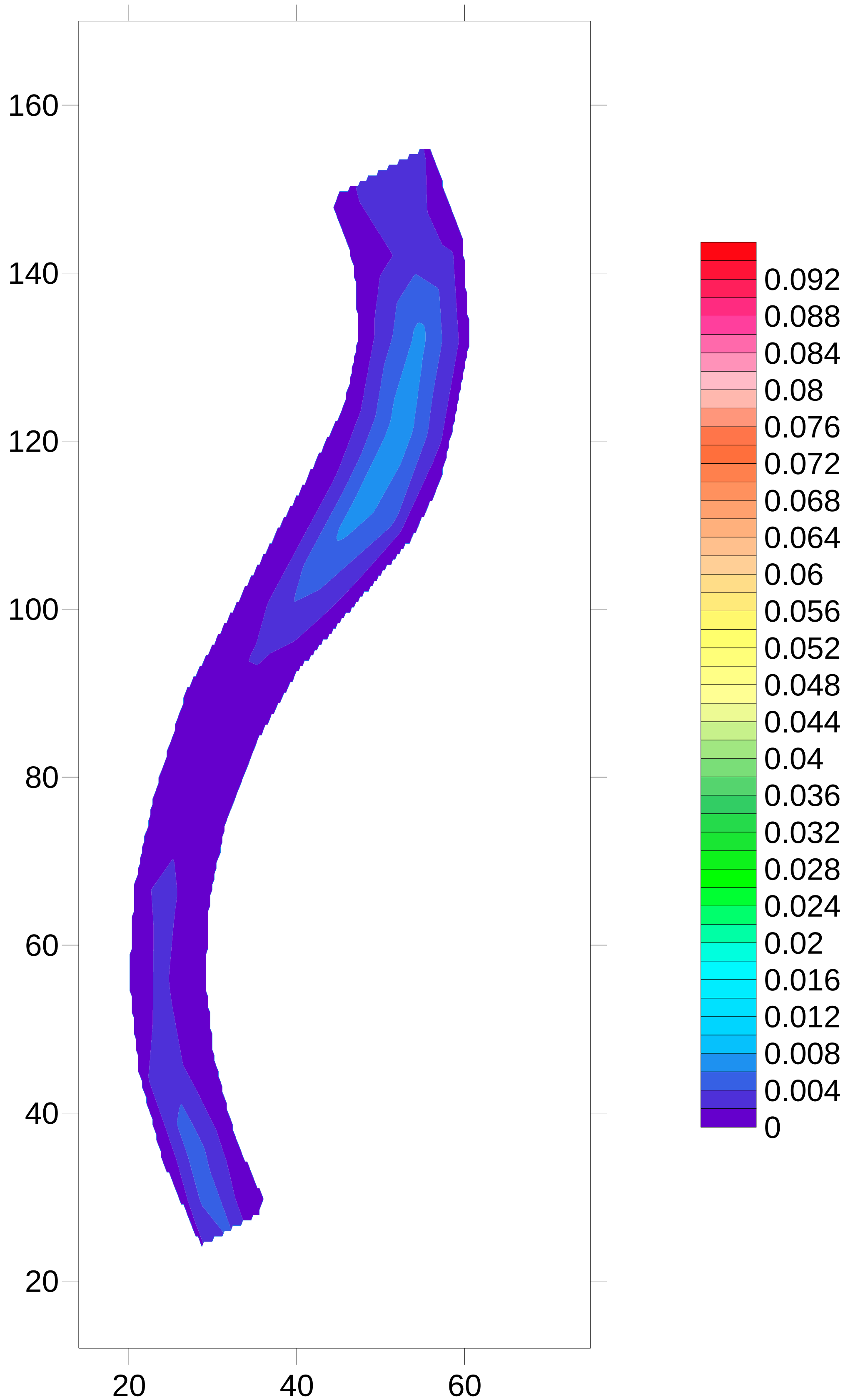

Figure C.5 Shear Stress Distribution, τ_y, by Linear Regression for 12 cfs (psf)

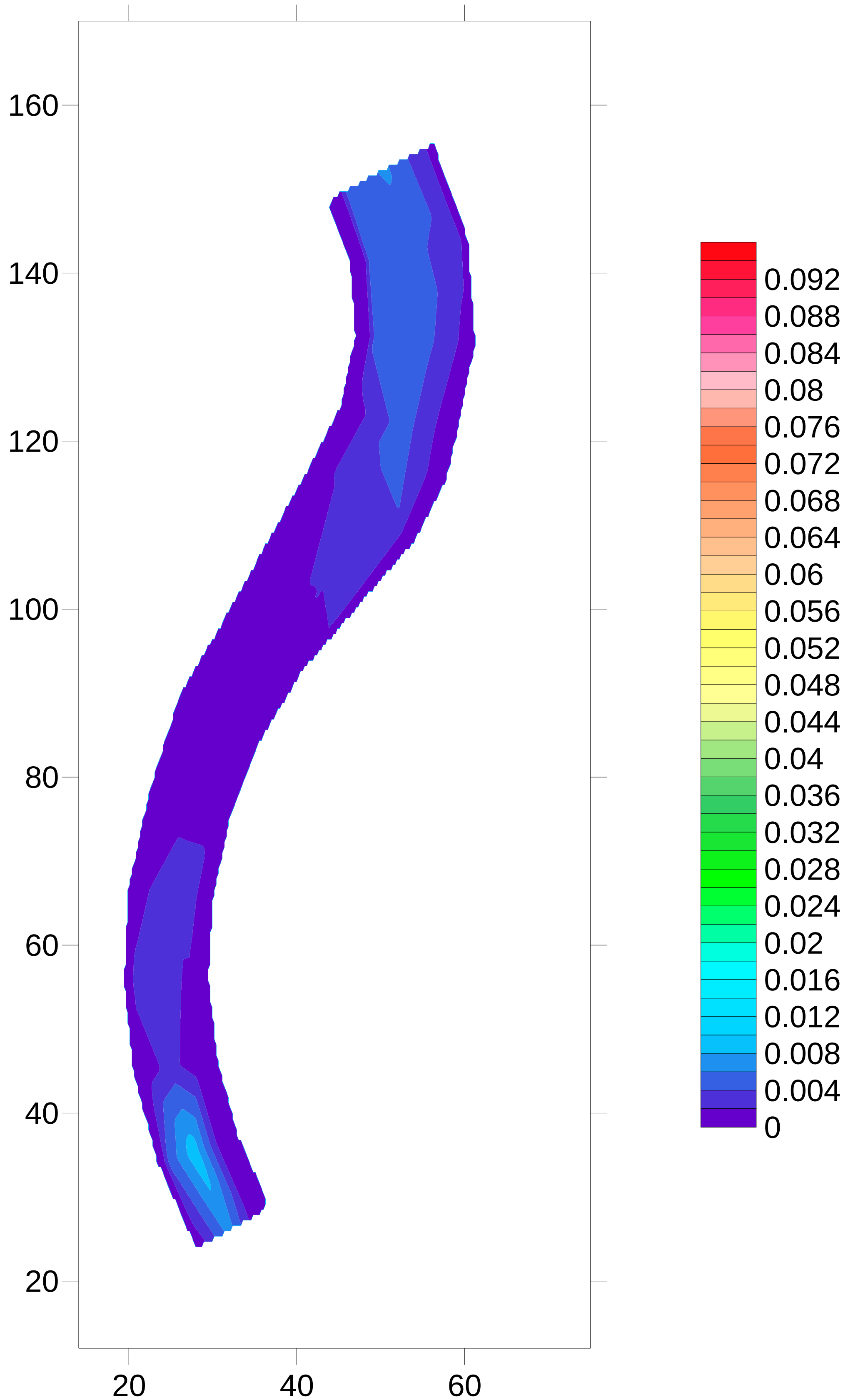

Figure C.6 Shear Stress Distribution, τ_y, by Linear Regression for 16 cfs (psf)

Appendix D. Shear Stress from Rozovskii (1961) Method

Table D.1 Shear stress (τ_y) from Rozovskii (1961) Method for 8 cfs

XSEC	Piezo	Shear Stress (psf)
4	c	0.0607
4	d	0.0683
4	e	0.0559
5	c	0.0090
5	d	0.0100
5	e	0.0104
6	c	0.0250
6	d	0.0247
6	e	0.0269
7	c	-0.0218
7	d	-0.0239
7	e	-0.0135
8	c	-0.0290
8	d	-0.0314
8	e	-0.0134
10	c	-0.0478
10	d	-0.0426
10	e	-0.0344
11	c	0.0140
11	d	0.0145
11	e	0.0284
12	c	0.0347
12	d	0.0288
12	e	0.0367
13	c	0.0246
13	d	0.0200
13	e	0.0175
14	c	0.0054
14	d	-0.0145
14	e	-0.0093
15	c	0.0649
15	d	0.0547
15	e	0.0501
16	c	0.0383
16	d	0.0228
16	e	0.0188
17	c	0.0463
17	d	0.0280
17	e	0.0202

Table D.2 Shear stress (τ_y) from Rozovskii (1961) Method for 12 cfs

XSEC	Piezo	Shear Stress (psf)	XSEC	Piezo	Shear Stress (psf)
4	b	0.0518	14	b	0.0223
4	c	0.0765	14	c	0.0047
4	d	0.0803	14	d	-0.0240
4	e	0.0589	14	e	-0.0133
4	f	0.0564	14	f	0.0045
5	b	-0.0096	15	b	0.0379
5	c	-0.0222	15	c	0.0335
5	d	-0.0256	15	d	0.0006
5	e	-0.0339	15	e	0.0022
5	f	-0.0049	15	f	0.0166
6	b	0.0264	16	b	0.0684
6	c	0.0337	16	c	0.0815
6	d	0.0363	16	d	0.0497
6	e	0.0307	16	e	0.0443
6	f	0.0307	16	f	0.0391
7	b	-0.0021	17	b	0.1012
7	c	-0.0112	17	c	0.1328
7	d	-0.0153	17	d	0.1157
7	e	-0.0027	17	e	0.0941
7	f	0.0089	17	f	0.0727
8	b	0.0346			
8	c	0.0397			
8	d	0.0438			
8	e	0.0639			
8	f	0.0505			
10	b	-0.0074			
10	c	-0.0266			
10	d	-0.0068			
10	e	-0.0038			
10	f	0.0043			
11	b	0.0264			
11	c	0.0176			
11	d	0.0323			
11	e	0.0460			
11	f	0.0443			
12	b	0.0240			
12	c	0.0100			
12	d	0.0050			
12	e	0.0173			
12	f	0.0239			
13	b	0.0641			
13	c	0.0659			
13	d	0.0664			
13	e	0.0694			
13	f	0.0561			

Table D.3 Shear stress (τ_y) from Rozovskii (1961) Method for 16 cfs

XSEC	Piezo	Shear Stress (psf)	XSEC	Piezo	Shear Stress (psf)
4	a	0.0273	11	d	0.0004
4	b	0.0324	11	e	0.0199
4	c	0.0453	11	f	0.0269
4	d	0.0504	11	g	0.0238
4	e	0.0163	12	a	0.0106
4	f	0.0372	12	b	0.0162
4	g	0.0368	12	c	0.0231
5	a	0.0181	12	d	0.0247
5	b	0.0186	12	e	0.0234
5	c	0.0266	12	f	0.0167
5	d	0.0289	12	g	0.0112
5	e	0.0085	13	a	0.0526
5	f	0.0239	13	b	0.0626
5	g	0.0261	13	c	0.0384
6	a	0.0386	13	d	0.0417
6	b	0.0478	13	e	0.0516
6	c	0.0651	13	f	0.0495
6	d	0.0598	13	g	0.0409
6	e	0.0546	14	a	0.0316
6	f	0.0535	14	b	0.0316
6	g	0.0438	14	c	0.0070
7	a	-0.0084	14	d	-0.0208
7	b	-0.0203	14	e	0.0265
7	c	-0.0317	14	f	0.0070
7	d	-0.0396	14	g	0.0154
7	e	-0.0310	15	a	0.0261
7	f	-0.0049	15	b	0.0206
7	g	0.0061	15	c	0.0000
8	a	0.0208	15	d	-0.0425
8	b	0.0208	15	e	-0.0368
8	c	0.0229	15	f	-0.0144
8	d	0.0203	15	g	0.0039
8	e	0.0518	16	a	0.0709
8	f	0.0467	16	b	0.0972
8	g	0.0380	16	c	0.1124
10	a	-0.0258	16	d	0.0768
10	b	-0.0639	16	e	0.0652
10	c	-0.0958	16	f	0.0575
10	d	-0.0722	16	g	0.0485
10	e	-0.0590	17	a	0.0259
10	f	-0.0234	17	b	0.0246
10	g	-0.0067	17	c	0.0101
11	a	0.0587	17	d	-0.0374
11	b	-0.0001	17	e	-0.0476
11	c	-0.0197	17	f	-0.0152
			17	g	-0.0060

Table D.4 Shear stress (τ_y) from Rozovskii (1961) Method for 20 cfs

XSEC	Piezo	Shear Stress (psf)	XSEC	Piezo	Shear Stress (psf)
4	a	0.0305	11	d	-0.0551
4	b	0.0386	11	e	-0.0259
4	c	0.0578	11	f	-0.0070
4	d	0.0668	11	g	0.0050
4	e	0.0262	12	a	-0.0012
4	f	0.0434	12	b	-0.0406
4	g	0.0431	12	c	-0.1019
5	a	0.0326	12	d	-0.0745
5	b	0.0431	12	e	-0.0432
5	c	0.0956	12	f	-0.0247
5	d	0.0560	12	g	-0.0036
5	e	0.0344	13	a	0.0439
5	f	0.0373	13	b	0.0308
5	g	0.0450	13	c	-0.0192
6	a	0.0474	13	d	-0.0096
6	b	0.0383	13	e	0.0128
6	c	0.0522	13	f	0.0188
6	d	0.0302	13	g	0.0251
6	e	0.0369	14	a	0.0264
6	f	0.0420	14	b	0.0140
6	g	0.0435	14	c	-0.0321
7	a	0.0182	14	d	-0.0576
7	b	0.0193	14	e	-0.0334
7	c	0.0256	14	f	-0.0128
7	d	0.0094	14	g	-0.0019
7	e	0.0618	15	a	0.0464
7	f	0.0332	15	b	0.0470
7	g	0.0392	15	c	0.0271
8	a	-0.0388	15	d	-0.0134
8	b	-0.0593	15	e	-0.0051
8	c	-0.0866	15	f	0.0053
8	d	-0.0996	15	g	0.0156
8	e	-0.0622	16	a	0.0487
8	f	-0.0327	16	b	0.0466
8	g	-0.0119	16	c	0.0364
10	a	-0.0100	16	d	-0.0190
10	b	-0.0271	16	e	-0.0147
10	c	-0.0378	16	f	0.0034
10	d	-0.0127	16	g	0.0160
10	e	0.0049	17	a	0.0185
10	f	0.0082	17	b	0.0118
10	g	0.0157	17	c	-0.0177
11	a	-0.0169	17	d	-0.0774
11	b	-0.0096	17	e	-0.0859
11	c	-0.0736	17	f	-0.0522
			17	g	-0.0231

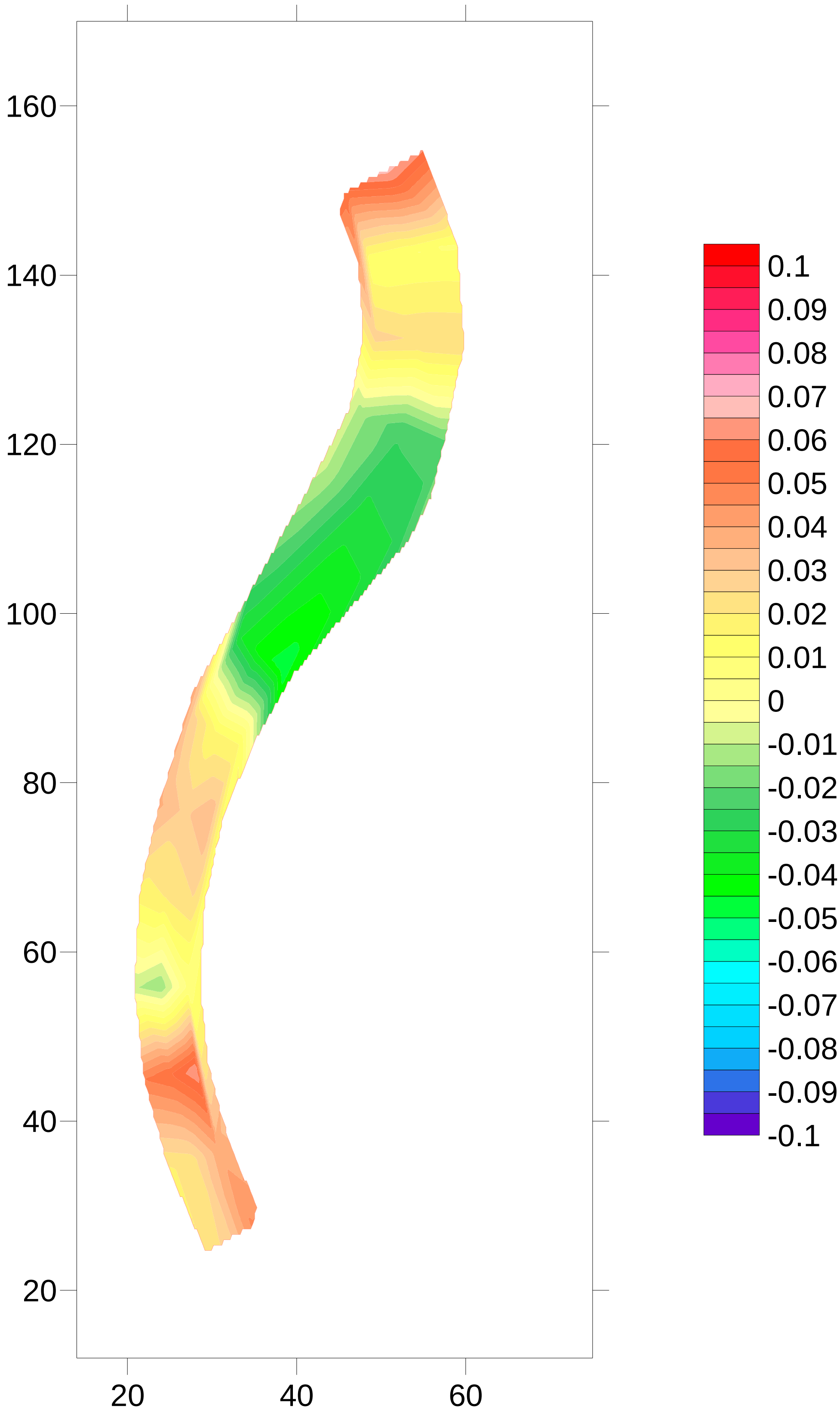

Figure D.1 Radial Shear Stress Distribution, τ_r, from Rozovskii (1961) for 8 cfs (psf)

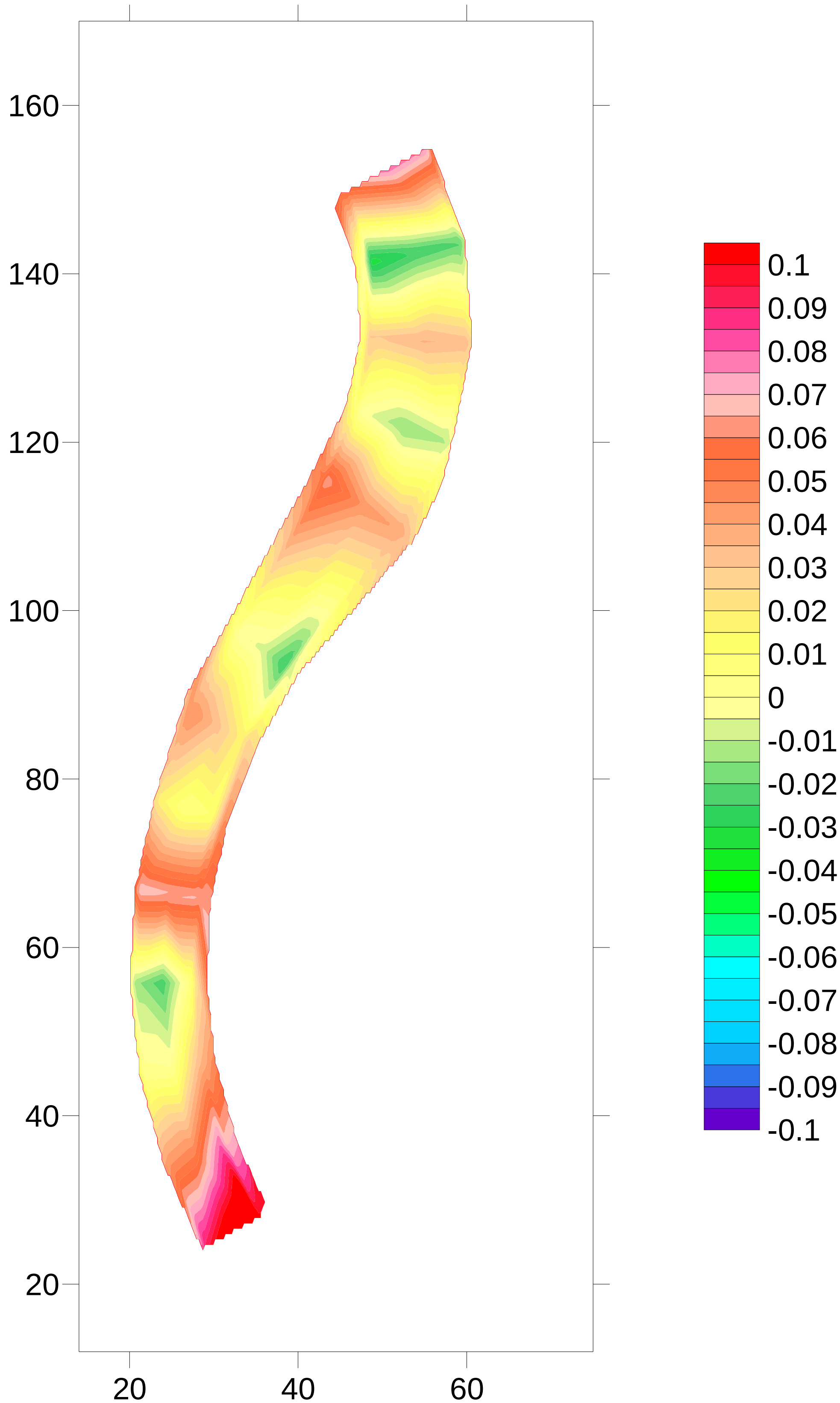

Figure D.2 Radial Shear Stress Distribution, τ_r, from Rozovskii (1961) for 12 cfs (psf)

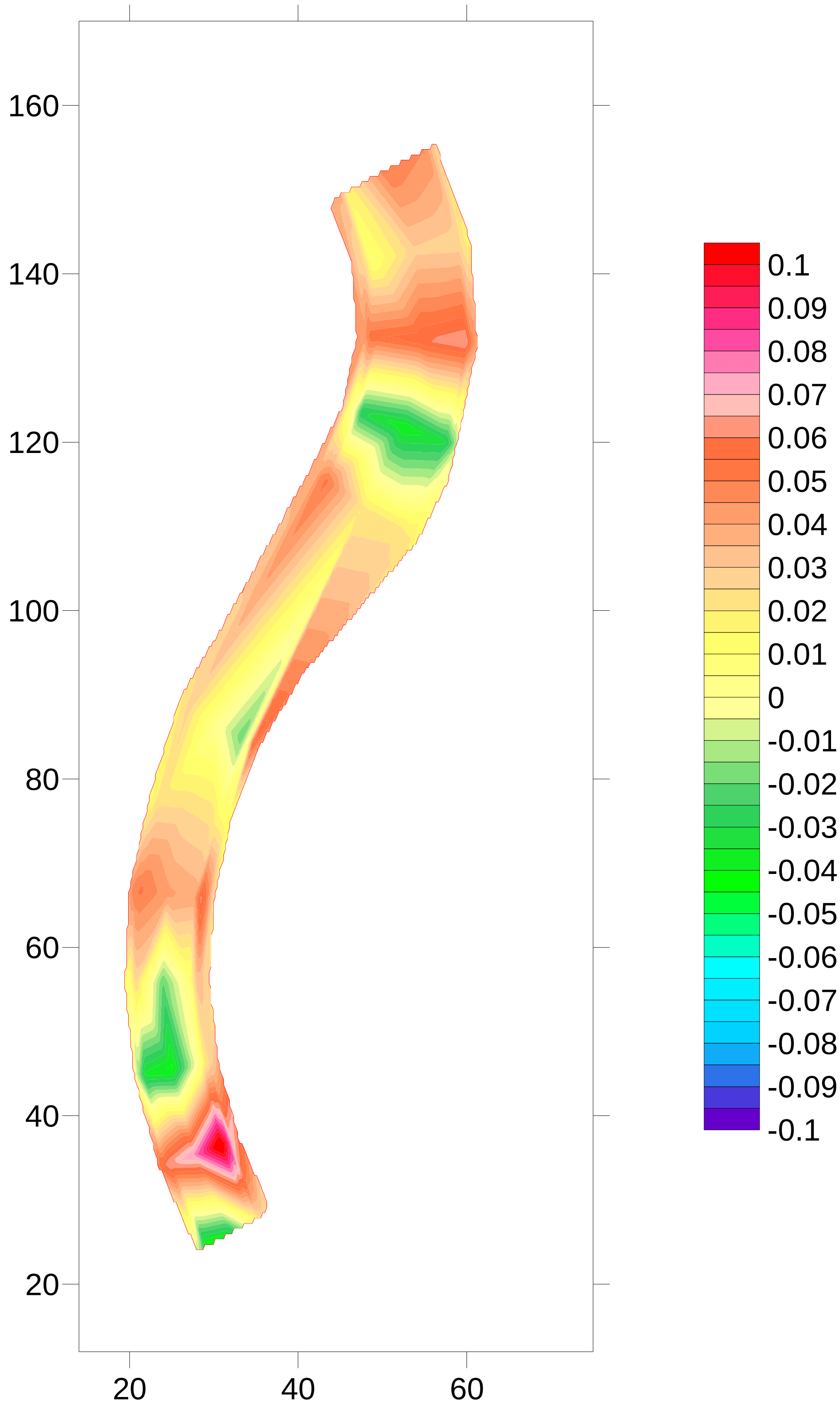

Figure D.3 Radial Shear Stress Distribution, τ_r, from Rozovskii (1961) for 16 cfs (psf)

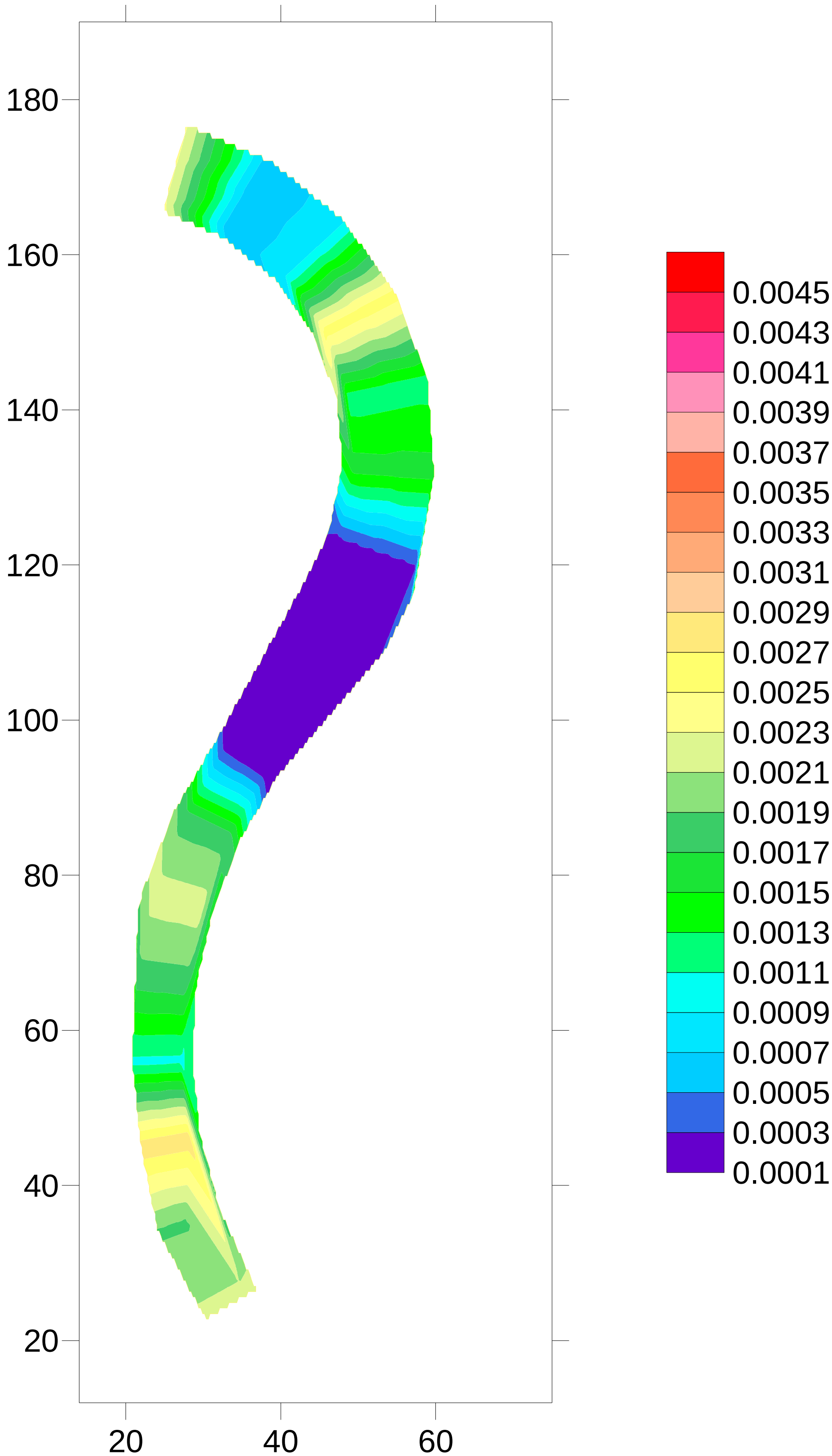

Figure D.4 Water Surface Slope Distribution for 8 cfs

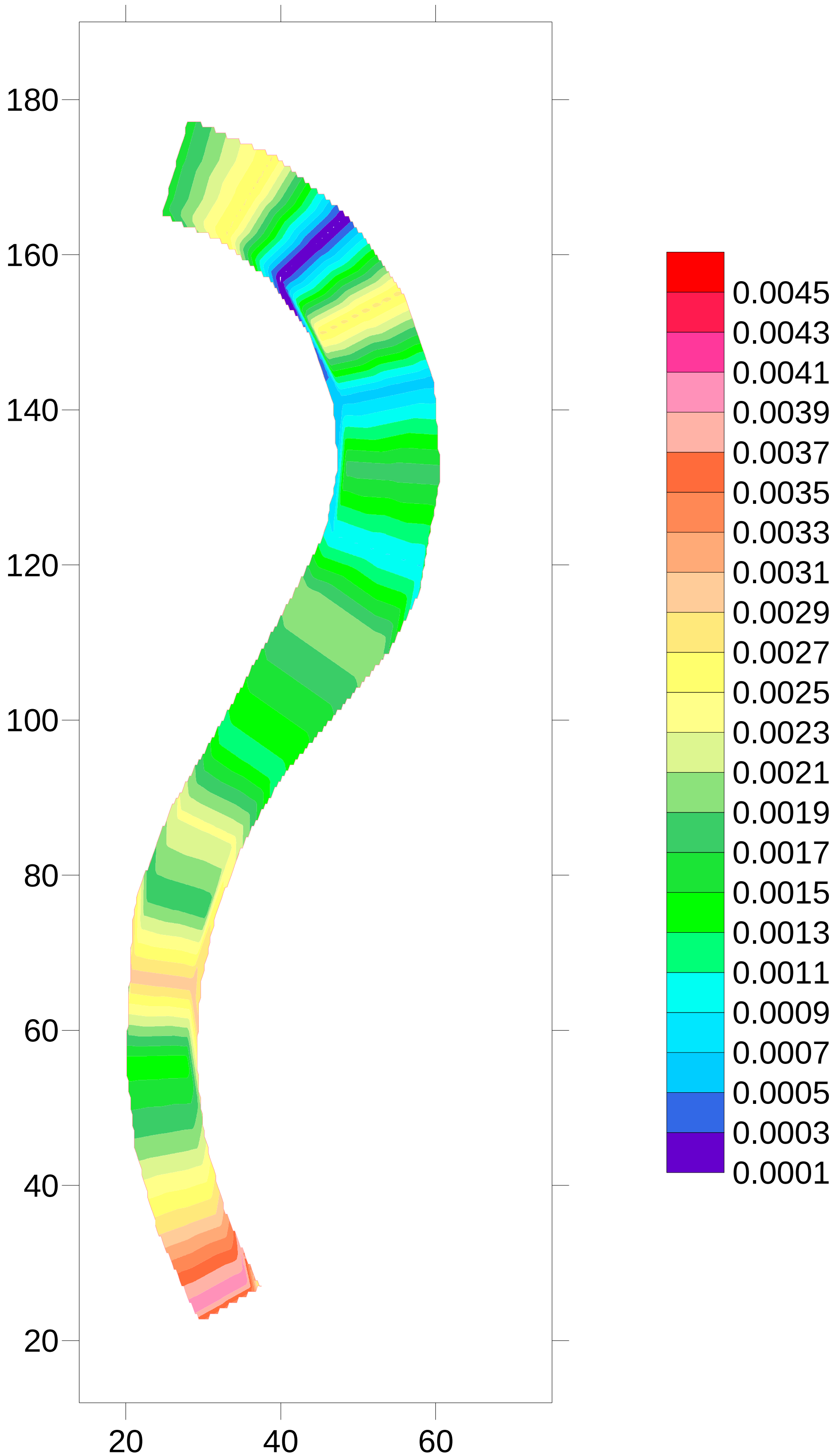

Figure D.5 Water Surface Slope Distribution for 12 cfs

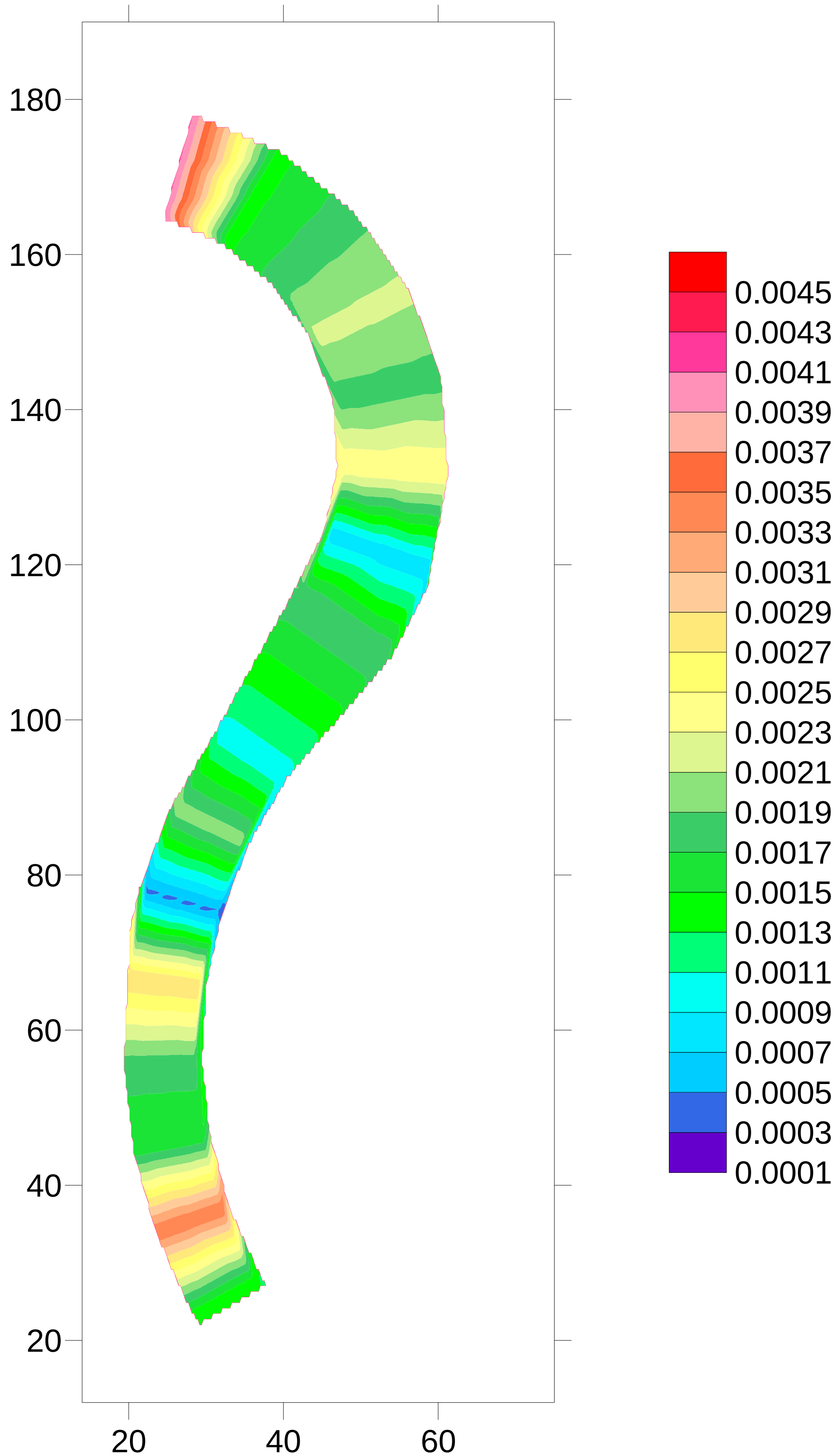

Figure D.6 Water Surface Slope Distribution for 16 cfs

Appendix E. Reynolds Shear Stress Extrapolation

E.1 Reynolds Shear Extrapolation

Appendix D shows the summary of the calculation result from Reynolds shear stress extrapolation. There are seven different columns in Table D.1 through Table D.9; Column 1 is the slope of linear regression equation of Reynolds shear stress profile, τxz; Column 2 is the intercept with y axis of the linear regression equation; Column 3 is the Reynolds shear stress, obtained from linear regression; and Column 4 through 6 is the same parameter of Reynolds shear stress; and Column 7 is bed shear stress computed from Equation 4.4. If Reynolds shear stress profile of τ_{xz} or τ_{zy} does not show similar trend with Figure 2.28, that data was presented as 'out' in Table E.1 through Table E.9.

Table E.1 Reynolds Shear Stress Calculation Summary for 8 cfs (psf)

	Column	1	2	3	4	5	6	7
XSEC	**Piezo**	Slope	b	τ_{xz}	Slope	b	τ_{yz}	τ_{bed}
4	c	-85.499	0.630	0.007	198.740	0.184	-0.001	0.007
4	d	out						
4	e	-74.965	0.508	0.007	-210.300	0.679	0.003	0.008
5	c	-159.730	0.668	0.004	980.910	0.295	0.000	0.004
5	d	out						
5	e	out						
6	c	-159.730	0.668	0.004	980.910	0.295	0.000	0.004
6	d	out						
6	e	out						
7	c	out						
7	d	out						
7	e	out						
8	c	out						
8	d	out						
8	e	-137.020	0.466	0.003	-1720.500	0.595	0.000	0.003
10	c	out						
10	d	-76.433	0.644	0.008	1017.000	-0.052	0.000	0.008
10	e	out						
11	c	-34.966	0.675	0.019	121.510	0.544	-0.004	0.020
11	d	out						
11	e	-56.983	0.607	0.011	-349.550	0.570	0.002	0.011
12	c	-62.656	0.723	0.012	835.890	2.459	-0.003	0.012
12	d	-60.051	0.756	0.013	-225.230	0.168	0.001	0.013
12	e	-59.604	0.717	0.012	-73.600	0.317	0.004	0.013
13	c	-45.212	0.588	0.013	113.030	0.669	-0.006	0.014
13	d	-51.017	0.872	0.017	-57.130	0.126	0.002	0.017
13	e	-67.681	0.779	0.012	-174.290	0.532	0.003	0.012
14	c	-203.800	1.299	0.006	-98.199	0.076	0.001	0.006
14	d	out						
14	e	-54.947	0.727	0.013	31.162	0.125	-0.004	0.014
15	c	-102.610	0.557	0.005	257.730	0.615	-0.002	0.006
15	d	-137.450	1.853	0.013	-150.880	0.060	0.000	0.013
15	e	-39.600	0.701	0.018	-97.857	0.285	0.003	0.018
16	c	out						
16	d	-32.438	0.732	0.023	237.930	0.655	-0.003	0.023
16	e	out						
17	c	out						
17	d	-43.757	0.693	0.016	-107.350	0.134	0.001	0.016
17	e	-47.680	0.741	0.016	-86.199	0.325	0.004	0.016

Table E.2 Reynolds Shear Stress Calculation Summary of Upstream Bend for 12 cfs (psf)

	Column	1	2	3	4	5	6	7
XSEC	**Piezo**	Slope	b	τ_{xz}	Slope	b	τ_{yz}	τ_{bed}
4	b	-19.205	0.432	0.022	158.380	0.382	-0.002	0.023
4	c	-39.107	0.517	0.013	-478.450	0.633	0.001	0.013
4	d	out						
4	e	-50.955	0.516	0.010	-98.052	0.584	0.006	0.012
4	f	out						
5	b	out						
5	c	-85.313	0.586	0.007	146.660	0.324	-0.002	0.007
5	d	-120.490	0.684	0.006	128.660	-0.016	0.000	0.006
5	e	-34.916	0.477	0.014	-144.470	0.672	0.005	0.014
5	f	-129.830	0.501	0.004	-188.650	0.607	0.003	0.005
6	b	-79.636	0.786	0.010	90.680	0.234	-0.003	0.010
6	c	out						
6	d	-137.420	0.942	0.007	95.307	0.125	-0.001	0.007
6	e	-76.112	0.631	0.008	-143.370	0.707	0.005	0.010
6	f	-111.540	0.448	0.004	241.340	0.089	0.000	0.004
7	b	-102.310	0.677	0.007	96.070	0.284	-0.003	0.007
7	c	out						
7	d	-66.081	0.695	0.011	-62.375	0.747	0.012	0.016
7	e	-61.544	0.597	0.010	-145.940	0.575	0.004	0.010
7	f	out						
8	b	-65.609	0.501	0.008	73.638	0.306	-0.004	0.009
8	c	-118.150	0.598	0.005	318.300	0.370	-0.001	0.005
8	d	-127.520	0.785	0.006	173.020	-0.142	0.001	0.006
8	e	-122.680	0.550	0.004	-247.340	0.631	0.003	0.005
8	f	-180.860	0.420	0.002	337.130	0.045	0.000	0.002

Table E.3 Reynolds Shear Stress Calculation Summary of Downstream Bend for 12 cfs (psf)

	Column	1	2	3	4	5	6	7
XSEC	**Piezo**	Slope	b	τ_{xz}	Slope	b	τ_{yz}	τ_{bed}
10	b	-53.036	0.636	0.012	160.080	0.477	-0.003	0.012
10	c	-43.527	0.422	0.010	179.770	0.405	-0.002	0.010
10	d	-90.334	0.663	0.007	230.060	0.036	0.000	0.007
10	e	out						
10	f	-69.233	0.514	0.007	139.520	0.029	0.000	0.007
11	b	out						
11	c	-36.108	0.612	0.017	170.530	0.563	-0.003	0.017
11	d	-60.498	0.652	0.011	69.190	0.332	-0.005	0.012
11	e	-86.993	0.718	0.008	-621.370	0.867	0.001	0.008
11	f	out						
12	b	out						
12	c	out						
12	d	-46.024	0.760	0.017	396.510	0.309	-0.001	0.017
12	e	-52.546	0.696	0.013	-59.134	0.345	0.006	0.014
12	f	out						
13	b	-46.268	0.459	0.010	-90.676	0.120	0.001	0.010
13	c	-30.808	0.640	0.021	72.360	0.658	-0.009	0.023
13	d	-60.780	1.010	0.017	192.070	0.667	-0.003	0.017
13	e	-46.912	0.731	0.016	-114.080	0.461	0.004	0.016
13	f	-32.038	0.489	0.015	-57.870	0.429	0.007	0.017
14	b	out						
14	c	-35.097	0.556	0.016	86.888	0.707	-0.008	0.018
14	d	-48.936	1.025	0.021	230.900	1.032	-0.004	0.021
14	e	-65.275	0.891	0.014	-74.848	0.373	0.005	0.015
14	f	out						
15	b	out						
15	c	out						
15	d	out						
15	e	-63.118	0.719	0.011	-93.491	0.488	0.005	0.013
15	f	out						
16	b	-37.227	0.414	0.011	-179.480	0.009	0.000	0.011
16	c	-32.074	0.477	0.015	179.940	0.795	-0.004	0.016
16	d	-27.345	0.862	0.032	92.003	0.884	-0.010	0.033
16	e	-42.445	0.846	0.020	-68.900	0.533	0.008	0.021
16	f	out						
17	b	-59.835	0.456	0.008	355.190	0.734	-0.002	0.008
17	c	out						
17	d	out						
17	e	-33.915	0.605	0.018	-98.617	0.680	0.007	0.019
17	f	out						

Table E.4 Reynolds Shear Stress Calculation Summary of Upstream Bend for 16 cfs (psf)

	Column	1	2	3	4	5	6	7
XSEC	**Piezo**	Slope	b	τ_{xz}	Slope	b	τ_{yz}	τ_{bed}
4	a	-41.251	0.597	0.014	15.382	0.298	-0.019	0.024
4	b	-23.399	0.376	0.016	135.440	0.323	-0.002	0.016
4	c	-13.906	0.263	0.019	28.790	0.201	-0.007	0.020
4	d	-39.013	0.409	0.010	-201.050	0.865	0.004	0.011
4	e	-33.259	0.419	0.013	-74.613	0.452	0.006	0.014
4	f	out						
4	g	out						
5	a	-110.960	1.055	0.010	43.892	0.342	-0.008	0.012
5	b	-41.011	0.480	0.012	96.719	0.312	-0.003	0.012
5	c	out						
5	d	out						
5	e	-64.555	0.566	0.009	-86.411	0.509	0.006	0.011
5	f	out						
5	g	out						
6	a	out						
6	b	-80.810	0.628	0.008	180.710	0.577	-0.003	0.008
6	c	-74.016	0.485	0.007	125.430	0.272	-0.002	0.007
6	d	out						
6	e	-43.589	0.539	0.012	-71.690	0.491	0.007	0.014
6	f	-99.020	0.574	0.006	-113.330	0.611	0.005	0.008
6	g	-171.370	0.475	0.003	407.430	-0.153	0.000	0.003
7	a	out						
7	b	out						
7	c	-47.538	0.398	0.008	78.854	0.170	-0.002	0.009
7	d	out						
7	e	-67.955	0.522	0.008	-189.170	0.679	0.004	0.008
7	f	out						
7	g	out						
8	a	-27.059	0.440	0.016	227.180	0.603	-0.003	0.016
8	b	-89.206	0.679	0.008	172.470	0.312	-0.002	0.008
8	c	out						
8	d	-66.188	0.546	0.008	80.191	0.055	-0.001	0.008
8	e	-66.734	0.470	0.007	-198.710	0.585	0.003	0.008
8	f	out						
8	g	out						

Table E.5 Reynolds Shear Stress Calculation Summary of XS 10 ~ XS 15 for 16 cfs (psf)

	Column	1	2	3	4	5	6	7
XSEC	**Piezo**	Slope	b	τ_{xz}	Slope	b	τ_{yz}	τ_{bed}
10	a	-49.208	0.695	0.014	-145.130	0.058	0.000	0.014
10	b	-21.206	0.404	0.019	202.930	0.522	-0.003	0.019
10	c	-15.326	0.323	0.021	212.810	0.433	-0.002	0.021
10	d	-56.462	0.696	0.012	-207.880	0.890	0.004	0.013
10	e	-70.256	0.529	0.008	-298.600	0.701	0.002	0.008
10	f	-42.268	0.399	0.009	151.360	0.093	-0.001	0.009
10	g	out						
11	a	-27.333	0.462	0.017	-100.770	-0.034	0.000	0.017
11	b	-19.721	0.669	0.034	93.748	0.621	-0.007	0.035
11	c	-19.130	0.468	0.024	87.194	0.414	-0.005	0.025
11	d	-53.413	0.694	0.013	175.230	0.350	-0.002	0.013
11	e	out						
11	f	-41.670	0.681	0.016	-155.000	0.514	0.003	0.017
11	g	out						
12	a	-347.220	2.035	0.006	-110.420	0.078	0.001	0.006
12	b	-25.429	0.542	0.021	-56.215	-0.068	-0.001	0.021
12	c	-31.288	0.658	0.021	98.299	0.610	-0.006	0.022
12	d	out						
12	e	-44.729	0.626	0.014	-60.891	0.271	0.004	0.015
12	f	-20.463	0.458	0.022	-78.113	0.378	0.005	0.023
12	g	out						
13	a	-94.605	0.631	0.007	260.210	0.570	-0.002	0.007
13	b	out						
13	c	-17.961	0.611	0.034	78.781	0.799	-0.010	0.035
13	d	-21.909	0.745	0.034	133.100	0.640	-0.005	0.034
13	e	-30.917	0.700	0.023	-103.550	0.350	0.003	0.023
13	f	out						
13	g	out						
14	a	-61.407	0.601	0.010	216.920	0.581	-0.003	0.010
14	b	-49.525	0.582	0.012	-98.922	-0.051	-0.001	0.012
14	c	-19.658	0.549	0.028	146.640	0.817	-0.006	0.028
14	d	-24.346	0.824	0.034	-65.408	0.159	0.002	0.034
14	e	-31.980	0.788	0.025	-86.134	0.370	0.004	0.025
14	f	out						
14	g	out						
15	a	out						
15	b	-47.069	0.432	0.009	60.839	0.368	-0.006	0.011
15	c	-39.447	0.548	0.014	145.200	0.712	-0.005	0.015
15	d	-27.061	0.833	0.031	-67.040	0.211	0.003	0.031
15	e	-26.746	0.666	0.025	-76.329	0.436	0.006	0.026
15	f	out						
15	g	out						

Table E.6 Reynolds Shear Stress Calculation Summary of XS 16 ~ XS 17 for 16 cfs (psf)

	Column	1	2	3	4	5	6	7
XSEC	**Piezo**	Slope	b	τ_{xz}	Slope	b	τ_{yz}	τ_{bed}
16	a	-47.288	0.458	0.010	-199.770	0.175	0.001	0.010
16	b	-46.247	0.504	0.011	179.810	0.834	-0.005	0.012
16	c	-29.265	0.577	0.020	176.080	0.710	-0.004	0.020
16	d	-35.927	1.099	0.031	48.576	0.864	-0.018	0.035
16	e	-36.451	0.896	0.025	-30.185	0.325	0.011	0.027
16	f	out						
16	g	out						
17	a	out						
17	b	-53.205	0.434	0.008	128.620	0.600	-0.005	0.009
17	c	-24.473	0.407	0.017	113.890	0.580	-0.005	0.017
17	d	-28.354	0.889	0.031	57.236	0.981	-0.017	0.036
17	e	out						
17	f	out						
17	g	out						

Table E.7 Reynolds Shear Stress Calculation Summary of Upstream Bend for 20 cfs (psf)

	Column	1	2	3	4	5	6	7
XSEC	**Piezo**	Slope	b	τ_{xz}	Slope	b	τ_{yz}	τ_{bed}
4	a	-37.102	0.449	0.012	15.536	0.253	-0.016	0.020
4	b	-85.760	0.415	0.005	-32.778	0.297	0.009	0.010
4	c	-61.512	0.478	0.008	118.180	0.217	-0.002	0.008
4	d	-68.330	0.666	0.010	-105.620	0.648	0.006	0.012
4	e	-29.445	0.534	0.018	-57.002	0.702	0.012	0.022
4	f	out						
4	g	out						
5	a	-72.948	0.603	0.008	7.410	0.306	-0.041	0.042
5	b	out						
5	c	-64.419	0.483	0.008	-193.940	0.401	0.002	0.008
5	d	-95.145	0.838	0.009	-103.370	1.020	0.010	0.013
5	e	-27.537	0.394	0.014	-59.209	0.578	0.010	0.017
5	f	out						
5	g	out						
6	a	-71.402	0.747	0.010	20.729	0.252	-0.012	0.016
6	b	-6.582	0.317	0.048	-60.666	0.314	0.005	0.048
6	c	-48.443	0.410	0.008	-395.840	0.541	0.001	0.009
6	d	out						
6	e	-49.203	0.551	0.011	-78.175	0.668	0.009	0.014
6	f	-60.304	0.536	0.009	-103.610	0.698	0.007	0.011
6	g	-95.615	0.404	0.004	107.930	0.018	0.000	0.004
7	a	-28.184	0.502	0.018	182.830	0.487	-0.003	0.018
7	b	-14.635	0.351	0.024	-268.680	0.398	0.001	0.024
7	c	-37.299	0.415	0.011	-696.570	0.714	0.001	0.011
7	d	-64.736	0.654	0.010	-54.499	0.918	0.017	0.020
7	e	-63.306	0.528	0.008	-91.264	0.687	0.008	0.011
7	f	-76.751	0.589	0.008	-120.930	0.714	0.006	0.010
7	g	out						
8	a	out						
8	b	-63.233	0.583	0.009	77.498	0.215	-0.003	0.010
8	c	-53.066	0.387	0.007	-366.460	0.839	0.002	0.008
8	d	-80.959	0.686	0.008	-53.388	0.827	0.015	0.018
8	e	-58.357	0.443	0.008	-133.030	0.700	0.005	0.009
8	f	-121.830	0.526	0.004	-152.670	0.659	0.004	0.006
8	g	out						

Table E.8 Reynolds Shear Stress Calculation Summary of XS 10 ~ XS 15 for 20 cfs (psf)

	Column	1	2	3	4	5	6	7
XSEC	**Piezo**	Slope	b	τ_{xz}	Slope	b	τ_{yz}	τ_{bed}
10	a	-34.832	0.713	0.020	-269.780	-0.042	0.000	0.020
10	b	-45.341	0.636	0.014	924.420	0.720	-0.001	0.014
10	c	-8.296	0.338	0.041	198.940	0.386	-0.002	0.041
10	d	-23.410	0.555	0.024	-264.620	1.107	0.004	0.024
10	e	-73.351	0.596	0.008	-181.650	0.681	0.004	0.009
10	f	-84.321	0.531	0.006	-316.250	0.904	0.003	0.007
10	g	-73.644	0.576	0.008	-388.540	1.040	0.003	0.008
11	a	out						
11	b	out						
11	c	-21.767	0.505	0.023	139.750	0.379	-0.003	0.023
11	d	out						
11	e	-49.223	0.692	0.014	-92.230	0.514	0.006	0.015
11	f	out						
11	g	out						
12	a	-15.267	0.522	0.034	-64.990	0.120	0.002	0.034
12	b	out						
12	c	-22.967	0.661	0.029	127.750	0.627	-0.005	0.029
12	d	-33.407	0.757	0.023	230.370	0.414	-0.002	0.023
12	e	out						
12	f	out						
12	g	-46.766	0.729	0.016	-41.799	0.353	0.008	0.018
13	a	-58.472	0.526	0.009	-90.486	0.049	0.001	0.009
13	b	out						
13	c	-15.042	0.671	0.045	70.757	0.694	-0.010	0.046
13	d	-22.680	0.684	0.030	99.242	0.598	-0.006	0.031
13	e	-47.751	0.780	0.016	289.290	0.465	-0.002	0.016
13	f	-37.787	0.769	0.020	-349.480	0.734	0.002	0.020
13	g	out						
14	a	-59.165	0.562	0.010	-105.600	0.014	0.000	0.010
14	b	-35.737	0.576	0.016	76.763	0.694	-0.009	0.018
14	c	-17.143	0.610	0.036	67.368	0.684	-0.010	0.037
14	d	-23.166	0.768	0.033	91.865	0.719	-0.008	0.034
14	e	-36.839	0.813	0.022	209.000	0.615	-0.003	0.022
14	f	out						
14	g	out						
15	a	-90.056	0.619	0.007	194.090	0.704	-0.004	0.008
15	b	-46.539	0.653	0.014	107.430	0.858	-0.008	0.016
15	c	-23.598	0.572	0.024	102.620	0.745	-0.007	0.025
15	d	-13.616	0.767	0.056	48.387	0.722	-0.015	0.058
15	e	-37.585	0.828	0.022	223.340	0.841	-0.004	0.022
15	f	-24.744	0.765	0.031	-104.440	0.505	0.005	0.031
15	g	out						

Table E.9 Reynolds Shear Stress Calculation Summary of XS 16 ~ XS 17 for 20 cfs (psf)

	Column	1	2	3	4	5	6	7
XSEC	**Piezo**	Slope	b	τ_{xz}	Slope	b	τ_{yz}	τ_{bed}
16	a	-76.102	0.555	0.007	336.330	1.135	-0.003	0.008
16	b	-48.828	0.522	0.011	223.790	0.893	-0.004	0.011
16	c	-25.677	0.594	0.023	78.620	0.760	-0.010	0.025
16	d	out						
16	e	out						
16	f	-35.273	0.840	0.024	-34.175	0.443	0.013	0.027
16	g	out						
17	a	out						
17	b	-53.979	0.571	0.011	60.137	0.612	-0.010	0.015
17	c	-45.774	0.534	0.012	128.750	0.709	-0.006	0.013
17	d	out						
17	e	-23.885	0.678	0.028	-34.993	0.272	0.008	0.029
17	f	out						
17	g	out						

Appendix F. Comparison of Shear Stress from Linear Regression of Velocity Profile for Lateral Direction (τ_y) and Rozovskii Method

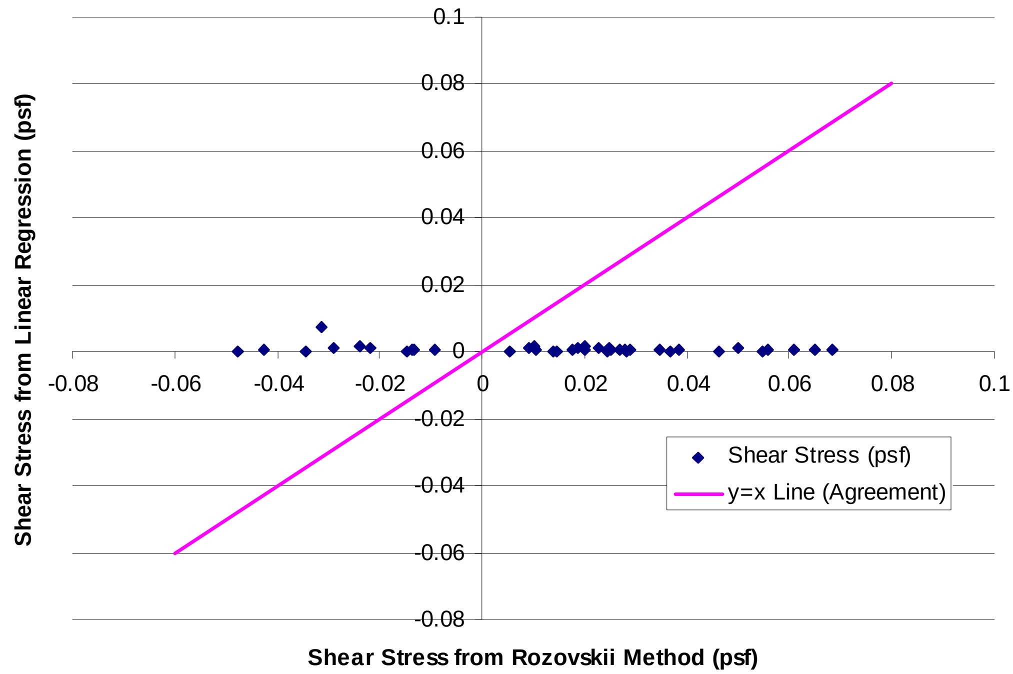

Figure F.1 Comparison of Shear Stress from Preston Tube and Rozovskii Method for 8 cfs

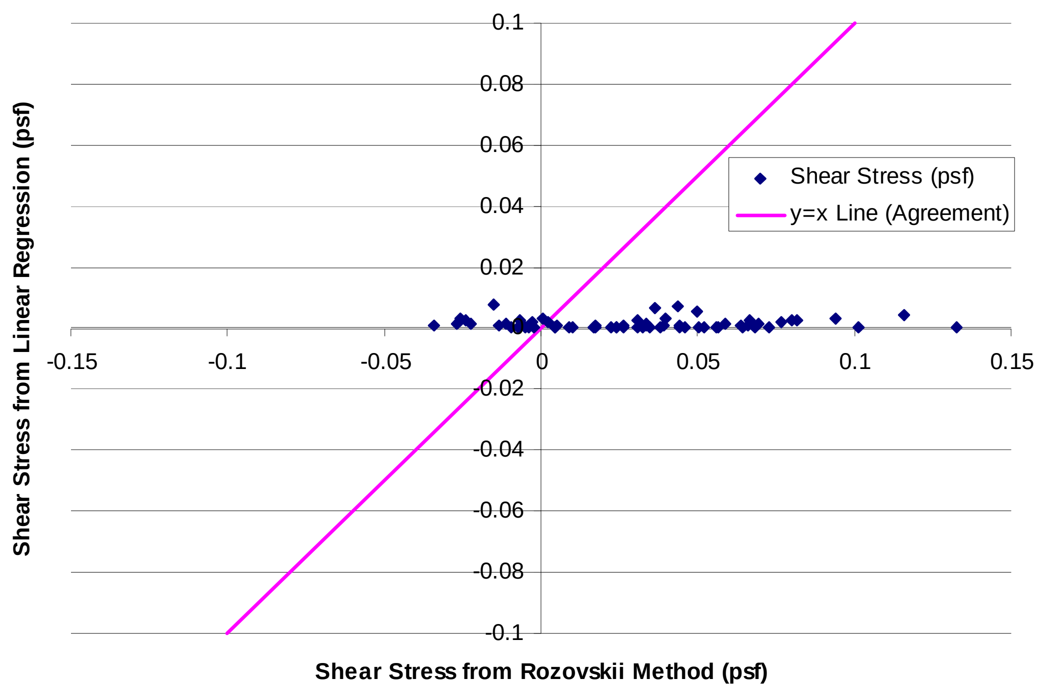

Figure F.2 Comparison of Shear Stress from Preston Tube and Rozovskii Method for 12 cfs

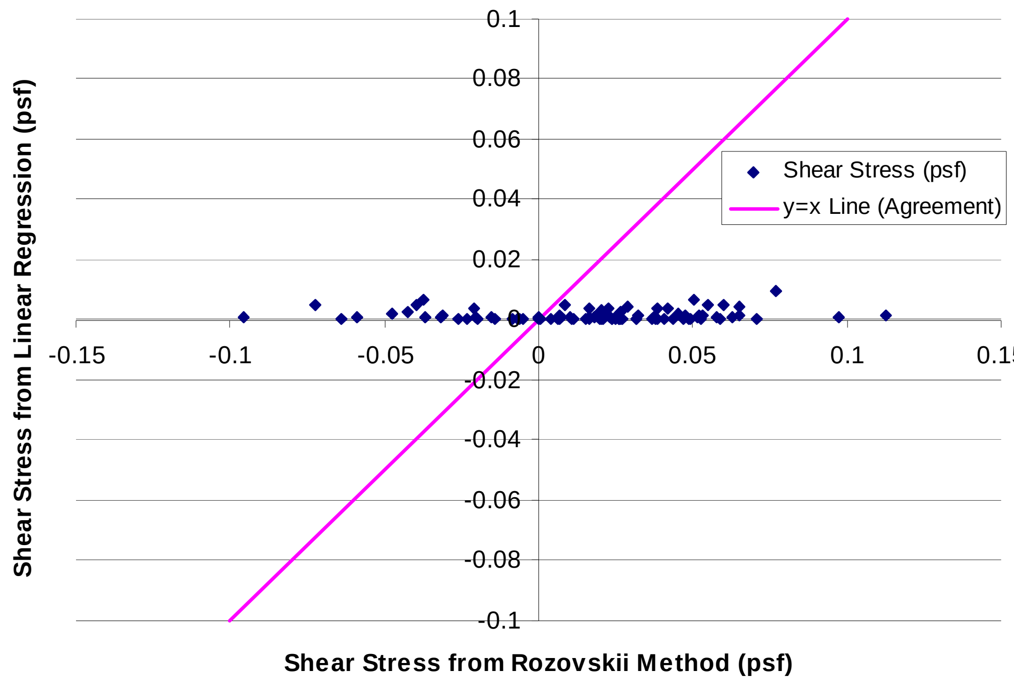

Figure F.3 Comparison of Shear Stress from Preston Tube and Rozovskii Method for 16 cfs

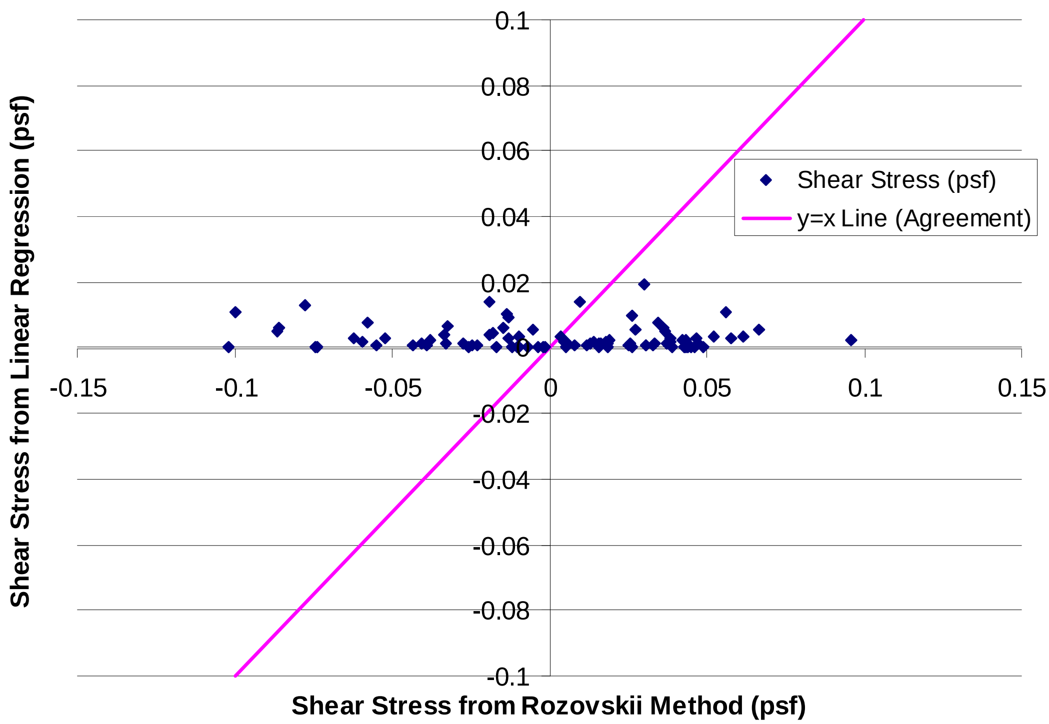

Figure F.4 Comparison of Shear Stress from Preston Tube and Rozovskii Method for 20 cfs

Appendix G. Comparison of Shear Stress Maximum Values

G.1 Comparison of Shear Stress Maximum Values

To compare shear stress calculation methods for different angles, maximum shear stress values from different methods are plotted in Appendix G. The blue lines in the plots show the averaged shear stress value from HEC-RAS. In upstream bend, shear stress from HEC-RAS in cross section 1 and 2 are averaged. For downstream bend, shear stresses from HEC-RAS in cross section 10 and 11 are averaged. Theoretically, the order of maximum value of shear stress should be; Shear stress from Preston tube > Shear stress from Reynolds shear extrapolation > Shear stress from linear regression because of the measurement method. The plots and prediction of the order of maximum shear stress was agreed well except for the case of 20 cfs in the upstream bend.

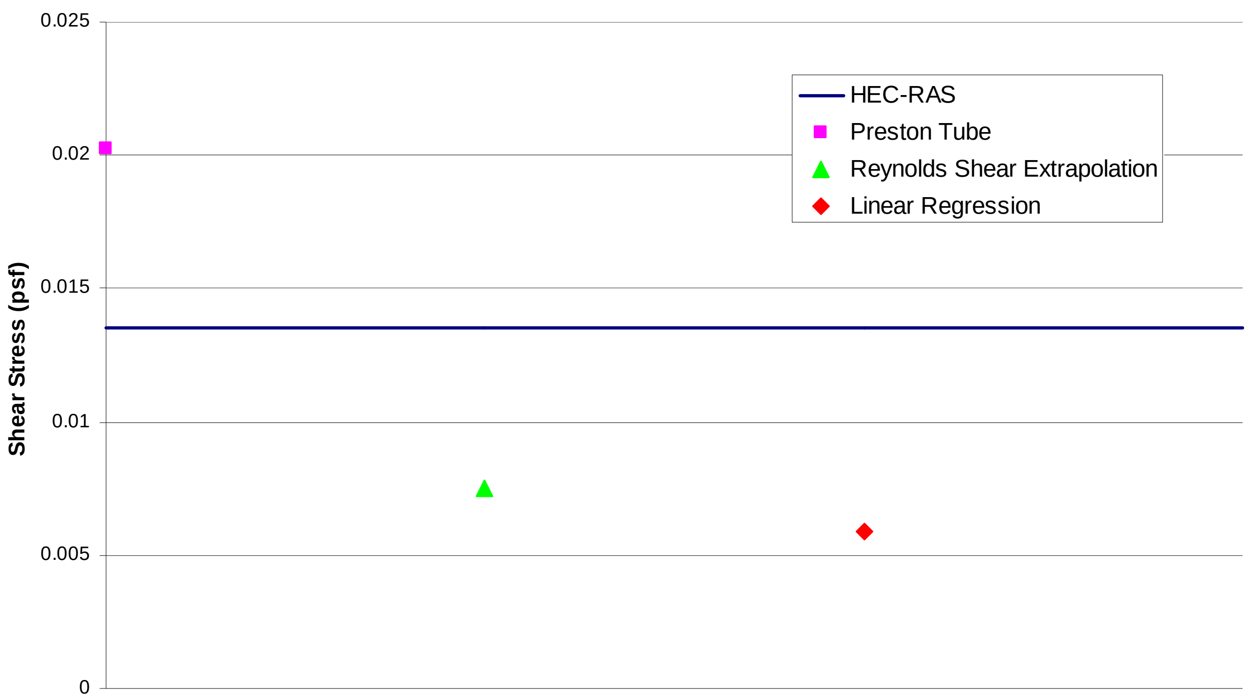

Figure G.1 Comparison of Shear Stress Maximum Values (8 cfs Upstream)

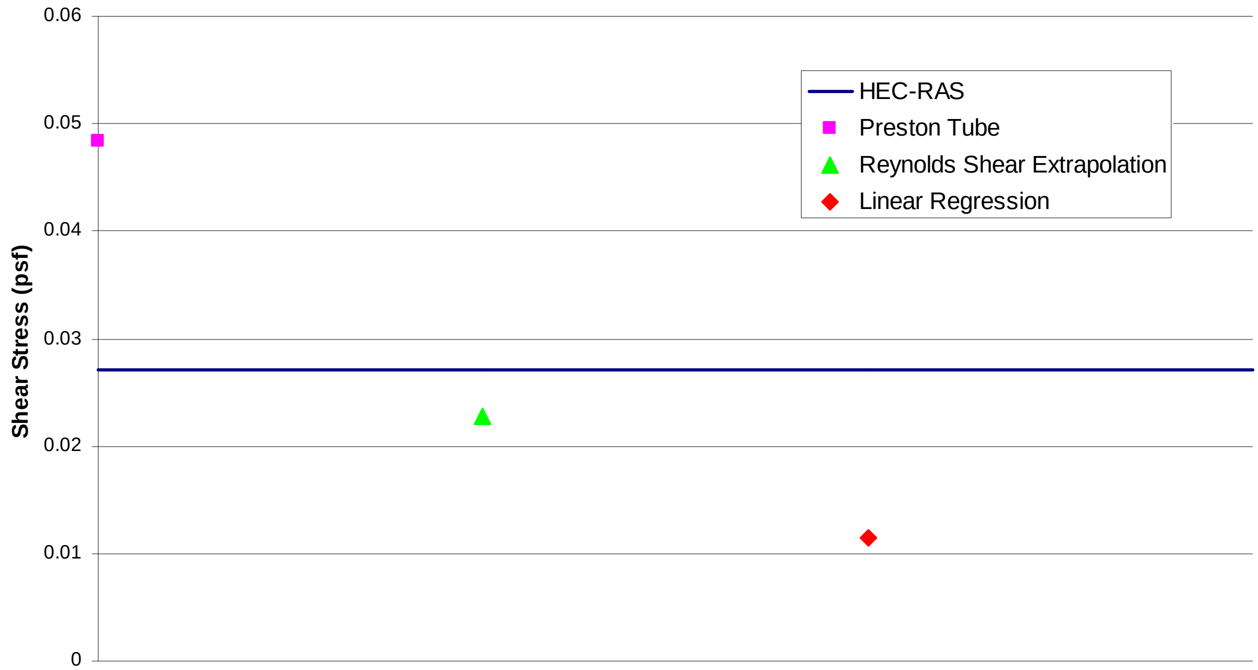

Figure G.2 Comparison of Shear Stress Maximum Values (8 cfs Downstream)

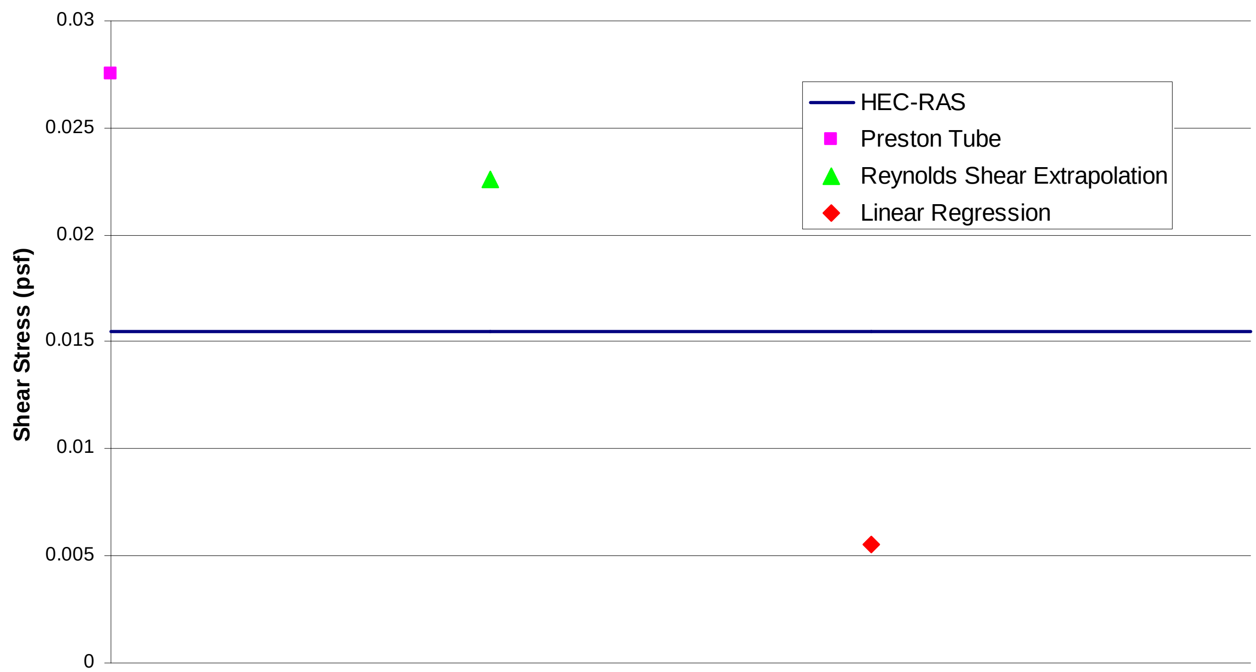

Figure G.3 Comparison of Shear Stress Maximum Values (12 cfs Upstream)

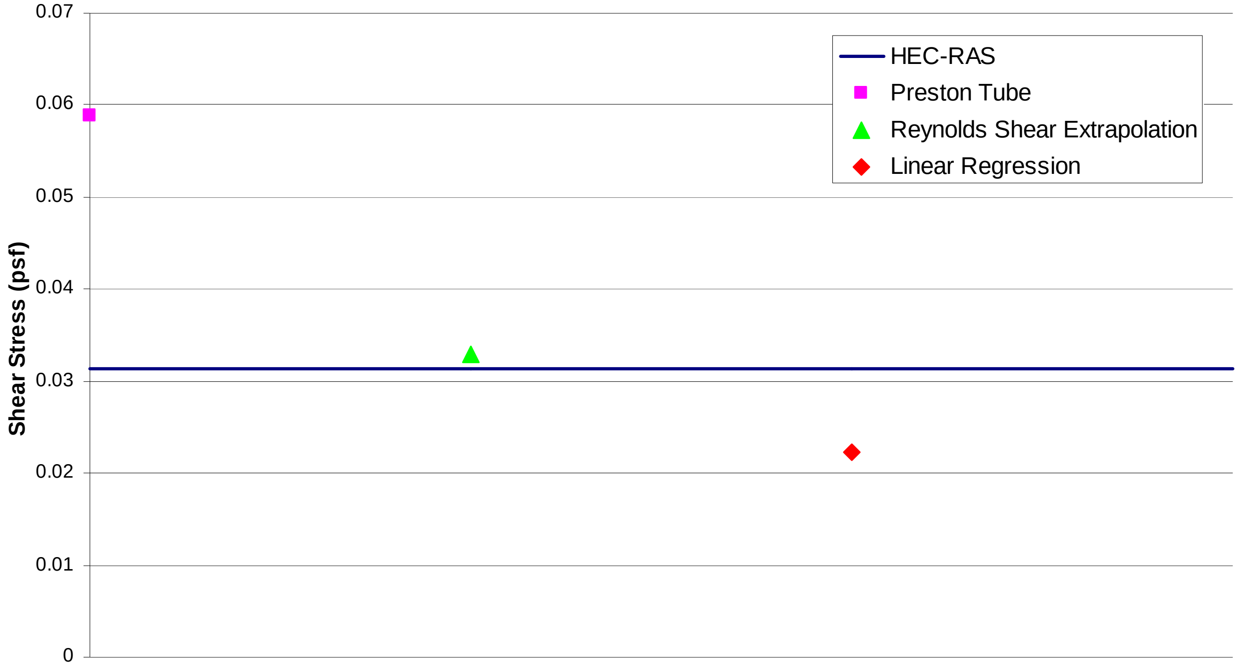

Figure G.4 Comparison of Shear Stress Maximum Values (12 cfs Downstream)

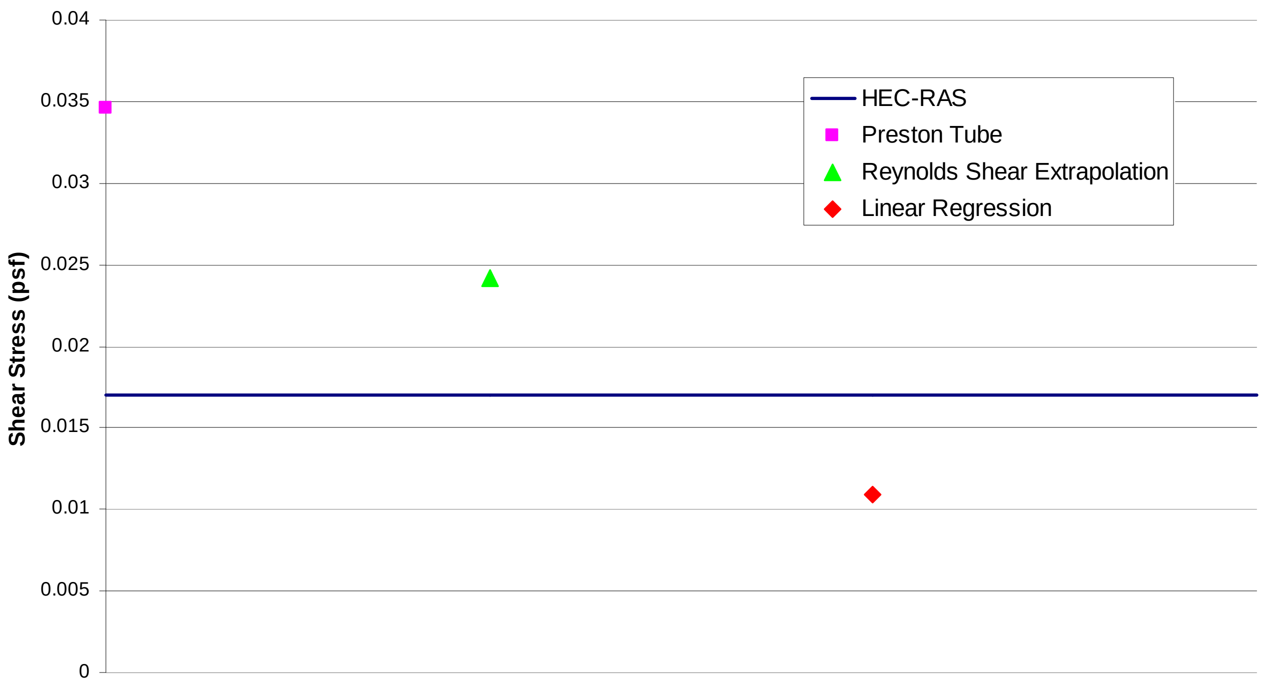

Figure G.5 Comparison of Shear Stress Maximum Values (16 cfs Upstream)

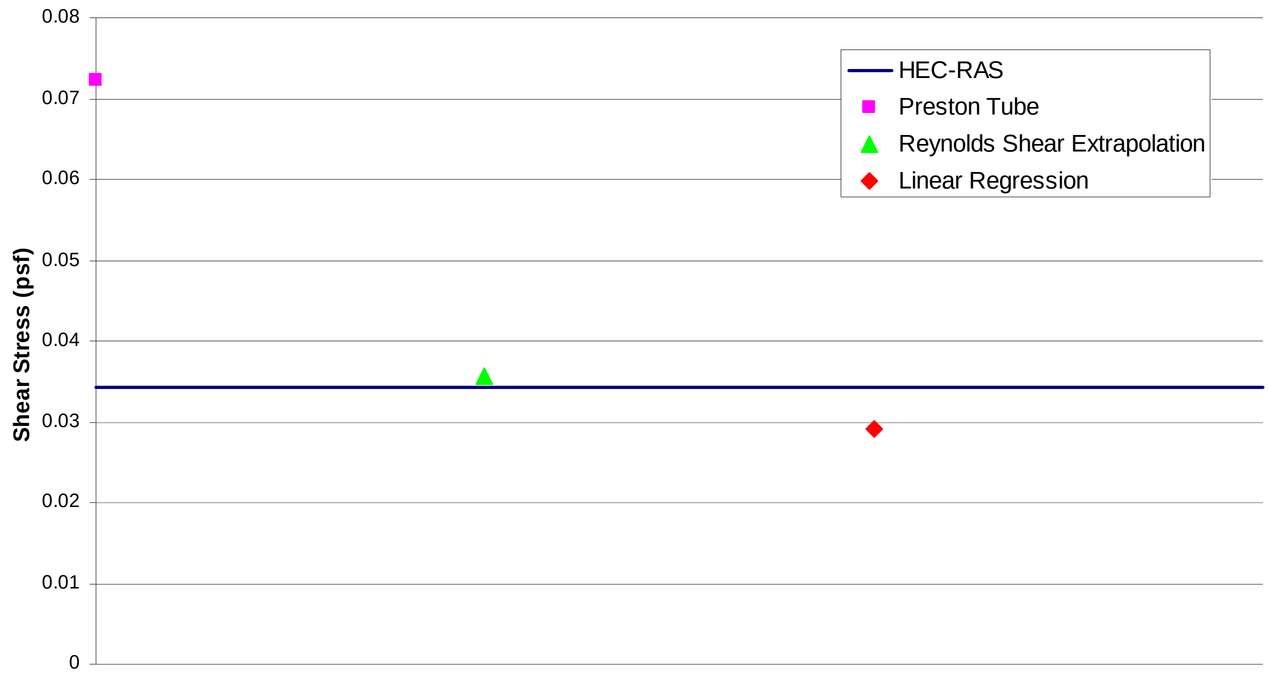

Figure G.6 Comparison of Shear Stress Maximum Values (16 cfs Downstream)

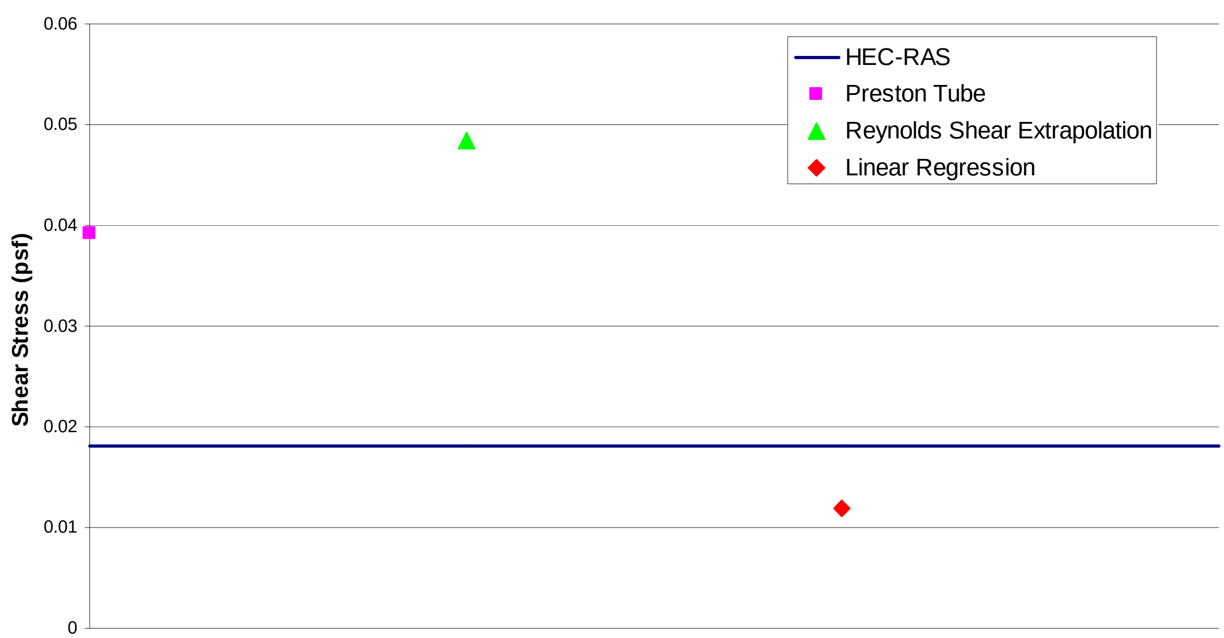

Figure G.7 Comparison of Shear Stress Maximum Values (20 cfs Upstream)

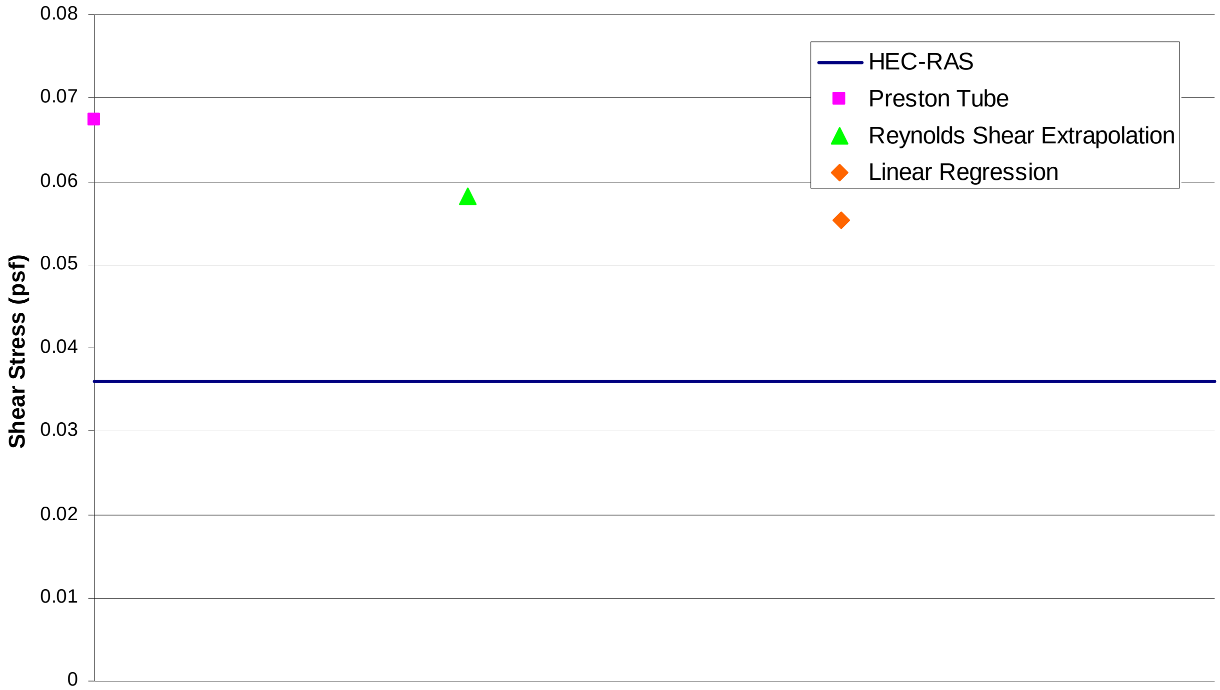

Figure G.8 Comparison of Shear Stress Maximum Values (20 cfs Downstream)